MICROWAVE REMOTE SENSING OF THE GREENLAND

ICE SHEET: MODELS AND APPLICATIONS

by

Ivan S. Ashcraft

A dissertation submitted to the faculty of

Brigham Young University

in partial fulfillment of the requirements for the degree of

Doctor of Philosophy

Department of Electrical and Computer Engineering

Brigham Young University

December 2004

BRIGHAM YOUNG UNIVERSITY

GRADUATE COMMITTEE APPROVAL

of a dissertation submitted by

Ivan S. Ashcraft

This dissertation has been read by each member of the following graduate committee and by majority vote has been found to be satisfactory.

_____   _____
Date   David G. Long, Chair

_____   _____
Date   Michael A. Jensen

_____   _____
Date   Brian D. Jeffs

_____   _____
Date   Perry J. Hardin

_____   _____
Date   Richard H. Selfridge

BRIGHAM YOUNG UNIVERSITY

As chair of the candidate's graduate committee, I have read the dissertation of Ivan S. Ashcraft in its final form and have found that (1) its format, citations, and bibliographical style are consistent and acceptable and fulfill university and department style requirements; (2) its illustrative materials including figures, tables, and charts are in place; and (3) the final manuscript is satisfactory to the graduate committee and is ready for submission to the university library.

_____   _____
Date   David G. Long
                                 Chair, Graduate Committee

Accepted for the Department

                                 _____
                                 Michael A. Jensen
                                 Graduate Coordinator

Accepted for the College

                                 _____
                                 Douglas M. Chabries
                                 Dean, College of Engineering and Technology

ABSTRACT

MICROWAVE REMOTE SENSING OF THE GREENLAND

ICE SHEET: MODELS AND APPLICATIONS

Ivan S. Ashcraft

Electrical and Computer Engineering

Doctor of Philosophy

Spaceborne microwave sensors are powerful tools for monitoring the impacts of global climate change on the Greenland ice sheet. This dissertation focuses on refining methods for applying microwave data in Greenland studies by using new simple theoretical and empirical models to investigate (1) azimuth anisotropies in the data, (2) the microwave signature of the snow surface, (3) detection of snow melt, and (4) classification of snow melt. The results are applicable for identifying geophysical properties of the snow surface and monitoring changes on the ice sheet in relation to melt duration/extent, accumulation, and wind patterns.

Azimuth dependence of the normalized radar cross-section ($\sigma°$) over the Greenland ice sheet is modeled with a simple surface scattering model. The model assumes that azimuth anisotropy in 1-100 meter scale surface roughness is the primary mechanism driving the azimuth modulation. This model is inverted to estimate snow surface properties using $\sigma°$ measurements from the C-band European Remote Sensing Advanced Microwave Instrument (ERS) in scatterometer mode. The largest roughness estimates occur in the lower portions of the dry snow zone. Estimates of

the preferential direction in surface roughness are highly correlated with katabatic wind fields over Greenland.

A new observation model is introduced that uses a limited number of parameters to characterize the snow surface based on the dependence of radar backscatter on incidence angle, azimuth angle, spatial gradient, and temporal rate of change. The individual model parameters are discussed in depth with examples using data from the NASA Scatterometer (NSCAT) and from the ERS. The model may be applied for increased accuracy in scatterometer, SAR, and wide-angle SAR studies. Examples illustrating the use of the model are included with one application focusing on analysis of inter-annual change and another focusing on increased sensitivity in studies of intra-annual change.

Six different melt detection method/sensor combinations are compared using data for the summer of 2000. The sensors include the Special Spectral Microwave Imager (SSM/I), SeaWinds on QuikSCAT (QSCAT), and ERS. A new method of melt detection is introduced that is based on a simple physical model relating the moisture content and depth of a layer of wet surface snow to a single channel melt detection threshold. The model can be applied to both active and passive sensors. Model-based melt estimates from different sensors are highly correlated and do not exhibit the unnatural phenomenon observed with previous methods.

Trends in SSM/I channel ratios are used to differentiate subsurface and surface melt. For ablation estimation, this separation is important due to expected differences in the ablation rate for the two melt types. Evidences of the daily melt refreeze cycle are observed in the diurnal variation of the different T_b channel ratios. The polarization ratio increases during periods of surface melt while the frequency ratio remains relatively constant. The frequency ratio increases during periods of expected subsurface melt. Similar trends are observed in T_b measurements from *in situ* data collected by other investigators.

ACKNOWLEDGMENTS

Thank you to my advisor, Dr. David Long, for his faith in me, his advice, and his support. He gave me enough room to wander in the dark and yet enough guidance to find the paths, steps, and bridges leading to the destination. Thank you to my wife, Stephanie, for her patience, faith, and support and to my children, Devan, Elizabeth, and Spencer for their smiles and their prayers. Thank you to my parents, Grant and Dorothy Ashcraft, for teaching me to, "Stick to a task 'til it sticks to you[1]."

---

[1]From the poem *Stick to your task*, Author Unknown

Contents

List of Tables

List of Figures

Chapter 1

Introduction

In recent years, spaceborne microwave instruments have been used in an increasing number of environmental studies including measuring near-surface ocean winds, observing tropical forest deforestation, tracking icebergs, mapping sea-ice extent, sea-ice classification, and more. These studies are based on theoretical and empirical methods relating the microwave measurements to the geophysical properties of the surface.

Spaceborne microwave sensors, including scatterometers and radiometers, are nearly optimal for large-scale studies requiring consistent relatively frequent observations. Current sensors observe over 90% of the Earth's surface each day. Microwaves penetrate cloud cover and are independent of solar illumination, reducing the need for optimal conditions to obtain quality measurements. Thus, accurate all-weather measurements are obtained night and day, resulting in consistent temporal and spatial coverage.

1.1 Scientific Interest in Greenland

The Greenland ice-sheet is an area where the use of spaceborne microwave instruments is particularly beneficial. Current scientific interest in Greenland stems from its position as a powerful measuring stick for monitoring global climate change. Greenland is the largest island on Earth and is almost completely covered by a large ice-sheet. Because of its size, this ice-sheet plays an important role in sea-level changes

and the Earth's radiation budget[1]. Large-scale changes on the ice sheet are important indicators of global climate change.

The mass-balance of the ice-sheet is a major contributor to changes in the global sea level. Paterson and Reeh [1] state, "The greatest uncertainty in predicting future sea level changes lies with our estimates of the mass balance of the ice sheets in Greenland and Antarctica." Greenland contains eight percent of the Earth's ice, enough water to raise sea-level by 7 meters [2]. It is estimated that 7% of the current rise in sea-level originates from the Greenland ice-sheet [3].

Changes in the duration and extent of Greenland melt is important to the earth's radiation budget. With a surface area of $\sim 1.75 \text{x} 10^6$ km^2, the Greenland ice-sheet constitutes 11% of the global glacier surface area [2]. Dry snow has a high albedo, reflecting most of the incoming solar radiation; however, liquid moisture present in the snow reduces the albedo increasing the solar radiation absorption three fold [4]. Because the interior of the ice sheet has a small slope (typically less than 1°), small changes in air temperature result in large changes in the areal extent of the melt [5]. This increase in absorption of solar radiation with increasing melt represents an unstable positive feedback mechanism in our climate system. Increased temperatures are also expected to contribute to an increase in accumulation. This adds another complexity to predicting the effects of climate change on the mass-balance of the ice-sheet.

The dynamics of the ice-sheet are also important indicators of global climate change. Variations in yearly melt extent and duration over the ice-sheet are related to variations in global temperature. Tracking and understanding changes on Greenland requires consistent large-scale observations of the complete ice-sheet.

Multiple reasons motivate the use of microwave measurements in studying Greenland. Because of the size and harsh environment of the ice-sheet *in situ* observations are difficult to obtain. Microwave measurements are available for the complete ice-sheet dating back to 1978, and current spaceborne microwave instruments observe

---

[1]The balance between the radiation absorbed and emitted by the earth's surface.

the complete ice-sheet multiple times per day. Microwave measurements are also valuable for Greenland studies due to their sensitivity to snow grain size, snow wetness, and subsurface features. This sensitivity makes possible the delineation of Greenland ice facies, the tracking of accumulation, and the measurement of melt extent and duration. One limiting factor in the application of scatterometer and radiometer measurements is the relatively low resolution of the data. However, the uniform nature of the ice-sheet reduces the need for finer resolution. Additionally, current resources limit the practicality of large-scale long-term analysis at high resolution.

1.2   Previous Work

A significant amount of work has already been performed in using microwave measurements to study Greenland. Long and Drinkwater [6] used $\sigma°$ measurements from NASA's Seasat-A Scatterometer (SASS) to map the Greenland snow zones based on a physical scattering model. Several other investigators have used synthetic aperture radar (SAR) measurements in relating $\sigma°$ to the different snow zones [7, 8, 9]. Long term changes in the ice sheet were observed by Drinkwater and Long [10] using SASS, the NASA Scatterometer (NSCAT), and the European Remote Sensing satellite (ERS). Localized long term changes have also been observed using SAR [9].

Multiple studies have focused on measuring Greenland melt duration and extent. Special Sensor Microwave Imager (SSM/I) brightness temperature (T_b) measurements were used by Mote et al. [11], Mote and Anderson [12] and Abdalati and Steffen [2, 4, 5, 13] for measuring melt. Melt detection using the normalized radar cross-section ($\sigma°$) was performed by Wismann [14] using ERS measurements and by Nghiem et al. [15] using measurements from NASA's SeaWinds on QuikSCAT (QS-CAT). Pack and Jensen [16] used a data fusion with SSM/I and ERS measurements for melt detection.

Previous studies have also used microwave measurements to estimate accumulation. Studies focusing on long-term accumulation include Bolzan and Jezek [17] using SSM/I, Drinkwater et al. [18] using ERS and NSCAT, and Forster et al. [19]

using the ERS SAR. Annual accumulation studies have been performed by Wismann et al. [20] using ERS and Pack and Jensen [21] using SSM/I.

1.3   Current Focus

Although much work has been performed and significant progress has been made, microwave remote sensing of Greenland is still in its infancy. In this dissertation, I focus on improving four key areas: (1) understanding and accounting for azimuth dependencies in the measurements, (2) developing an improved observation model for monitoring change, (3) refining melt detection for improved correlation in melt detected by different sensors, and (4) classification of melt as either surface or subsurface. These studies primarily use scatterometer and radiometer data.

In previous studies over Greenland, the azimuth dependency of microwave measurements has been ignored. In Antarctica, an environment similar to Greenland, significant azimuth modulation has been observed [22, 23, 24]. When ignored, the azimuth dependency of the data appears as noise possibly corrupting the study results. Although azimuth modulation is documented over Antarctica, the physical mechanism driving the azimuth anisotropy is not well understood. I focus on the development of a simple scattering model to reproduce the observed azimuth modulation over Greenland.

The results from this model are consistent with azimuth dependence being caused by wind-formed surface features on the snow. The model is inverted using ERS measurements to estimate the relative variation in the slopes of these surface features and the direction of average wind flow. The estimates of the meso-scale surface slopes are largest in the lower portions of the dry snow zone. Wind flow estimates are consistent with automatic weather station measurements and atmospheric model estimates of Greenland katabatic wind flow. The mean RMS error of the inverted model estimates is 0.46 dB compared to 0.56 dB when the meso-scale surface slopes are assumed to be azimuthally isotropic. The improvement in the model estimation occurs primarily in the lower dry snow zone where the azimuth modulation is largest.

Parameterization of the azimuth modulation provides additional information about the microwave signature of the surface. Changes in these parameters indicate specific changes occurring on the surface. One of the difficulties in remote sensing is many-to-one mapping where different surface profiles result in similar microwave measurements. A knowledge of the azimuth and incidence angle dependence, along with other attributes of the microwave signature, enables improved characterization of the surface profile. A classic example is measuring σ° over the ocean. Some knowledge of the near-surface ocean wind speed can be obtained from a single σ° measurement; however, by combining multiple measurements, not only can the the wind speed be estimated much more accurately, but the wind direction can also be inferred.

I develop a descriptive model for characterizing multiple σ° measurements using a limited number of parameters. This model provides additional parameters which help identify the long-term changes occurring on the ice-sheet. Using this model, the microwave signature is characterized using 7 to 10 parameters depending on the instrument design and the desired model accuracy. Next to incidence angle dependence, model terms involving the spatial gradient provide the greatest reduction in RMS error. This is followed by model terms for azimuth modulation and temporal variation. The average RMS error using the full model is approximately 0.375 dB for ERS and 0.458 dB for NSCAT. Inter-annual changes in the ERS model parameter estimates are related to annual changes in melt extent, the formation of iced-firn on the snow surface, the formation of subsurface ice-structures, and annual changes in accumulation rate.

Because the model parameters are relatively constant between summer melt events, this model is also used to observe intra-annual changes in the average σ°. This method enables higher temporal resolution than traditional methods. Estimates of the change in the average σ° with time also have smaller variance than traditional methods. This aids in the observation of small magnitude annual trends such as those observed in the dry snow zone, and in the detection of short melt events.

Although various methods exist for melt detection over Greenland, these methods have not been compared on a large scale. In comparing these methods, I find significant discrepancies in the detection by each method as well as unnatural phenomenon in the temporal and spatial progression of the estimated melt. To develop melt detection methods for each sensor which give consistent results, I present a simple physical model of a melt event and its effect on σ° and T_b. This model is applicable for melt detection using σ° or T_b.

Melt detection based on this simple physical model yields results consistent between sensors with some variation due to frequency and temporal sampling differences. The correlation coefficient between model-based melt detection with the different sensors ranges from 0.87 to 0.73. The correlation coefficient for other existing methods is lower with the smallest correlation coefficient being 0.19. The unnatural phenomenon observed in results of previous methods are eliminated in the physical model-based methods. QSCAT and SSM/I melt detection estimate that approximately 60% of the ice-sheet experiences melt, which is consistent with estimates from *in situ* studies.

The next step in melt analysis over Greenland is classifying different types of melt. I focus on classification of melt as either surface of sub-surface. Because a single σ° or T_b value could correspond to either type of melt, multiple channels are required for this classification. Because SSM/I measures T_b at multiple frequency/polarization combinations simultaneously, this data set is used primarily for melt classification. Data from multiple sensors are employed to enable estimation of the diurnal variation in T_b and relate it to the stages of the daily melt cycle. This relationship is validated using *in situ* temperature measurements. Diurnal trends in the polarization ratios and frequency ratios are then used to associate the sensitivity of these ratios to the stages of the daily melt process. I find the horizontal to vertical polarization ratio to be a sensitive indicator of surface melt and the frequency ratio of 19 GHz to 37 GHz to be a sensitive indicator of subsurface melt.

1.4 Organization

This dissertation is organized in the following manner. Chapter 2 contains the general background fundamental to all of the following chapters. This includes a discussion on Greenland and its properties, a general background on $\sigma°$ and T_b, an overview of the various sensors, and a brief discussion on data processing. Chapter 3 develops a model for azimuth modulation of $\sigma°$ over Greenland including results from the model inversion. Chapter 4 develops a descriptive model for $\sigma°$ with applications and results. Chapter 5 introduces a simple physical model for melt detection and compares results from methods based on this model to previous methods of melt detection. Chapter 6 focuses on using frequency and polarization differences in T_b to classify different types of melt. Chapter 7 provides a summary and conclusions.

Chapter 2

Background

This chapter contains background universal to all of the research areas in this dissertation. First, is a brief introduction to $\sigma°$ and T_b, followed by a presentation of the sensors employed in my studies. Methods used for data processing and imaging are also discussed. This chapter concludes with background on Greenland.

2.1 The Normalized Radar Cross-Section

The normalized radar cross-section ($\sigma°$) is measure of the reflectivity of the surface relative to the direction of the transmit and receive antennas. It is defined as the ratio of the target radar cross-section (σ) to the actual target area (A_t), i.e.

$$\sigma° = \frac{\sigma}{A_t}.$$

The radar cross-section is defined using the *radar equation* [25]

$$P_r = \underbrace{P_t G_t (4\pi R_t^2)^{-1}}_{\text{incident power density}} \sigma \underbrace{(4\pi R_r^2)^{-1}}_{\text{spreading loss}} A_r \tag{2.1}$$

where P_r is the receive power, P_t is the transmit power, G_t is the normalized transmit gain in the direction of the target, R_t is the range from the transmit antenna to the target, R_r is the range from the target to the receive antenna, and A_r is the effective area of the receive antenna. The radar cross-section has an intuitive physical definition. The receive antenna effectively measures the scattered power density at the receive location. If it is assumed that the target scatters the power isotropically, the radar cross-section is the area required to capture the right amount of transmitted power to generate the received signal (see Fig. 2.1).
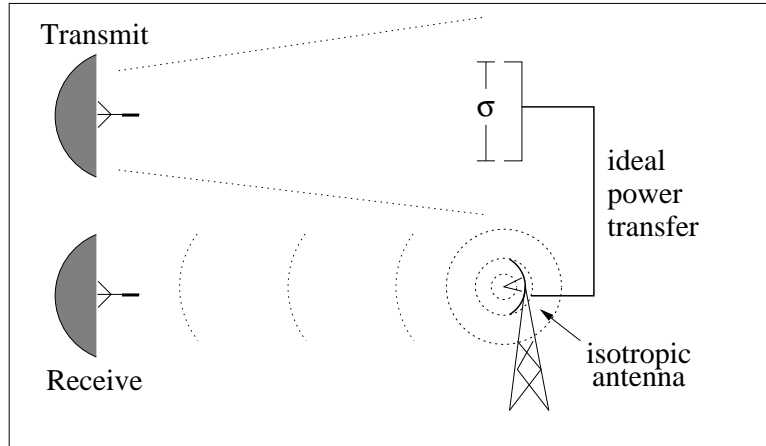
Figure 2.1: Illustration of the radar cross-section (σ) and the radar equation. Based on the radar equation, σ represents the area required to capture the transmitted power and re-radiate it isotropically to produce the power density measured by the receive antenna.

The radar equation can be rewritten in terms of the gain of the receive antenna (G_r) using the relationship

$$G_r = \frac{4\pi A_r}{\lambda^2}$$

where λ is the wavelength of the signal. The new form of Eq. (2.1) is

$$P_r = P_t \lambda^2 \frac{G_t G_r}{(4\pi)^3 R_t^2 R_r^2} \sigma. \qquad (2.2)$$

For the mono-static case where the same antenna is used for transmit and receive, $G_t = G_r = G$, $R_t = R_r = R$, and Eq. (2.2) becomes

$$P_r = P_t \lambda^2 \frac{G^2}{(4\pi)^3 R^4} \sigma. \qquad (2.3)$$

If the target is large, G, R, and σ° vary across the illuminated area for which case the integral form of the radar equation,

$$P_r = \frac{P_t \lambda^2}{(4\pi)^3} \int_{A_t} \frac{G^2}{R^4} \sigma^\circ \, \mathrm{d}a,$$

is used where A_t is the illuminated area on the target. The illuminated area is typically termed the antenna footprint.
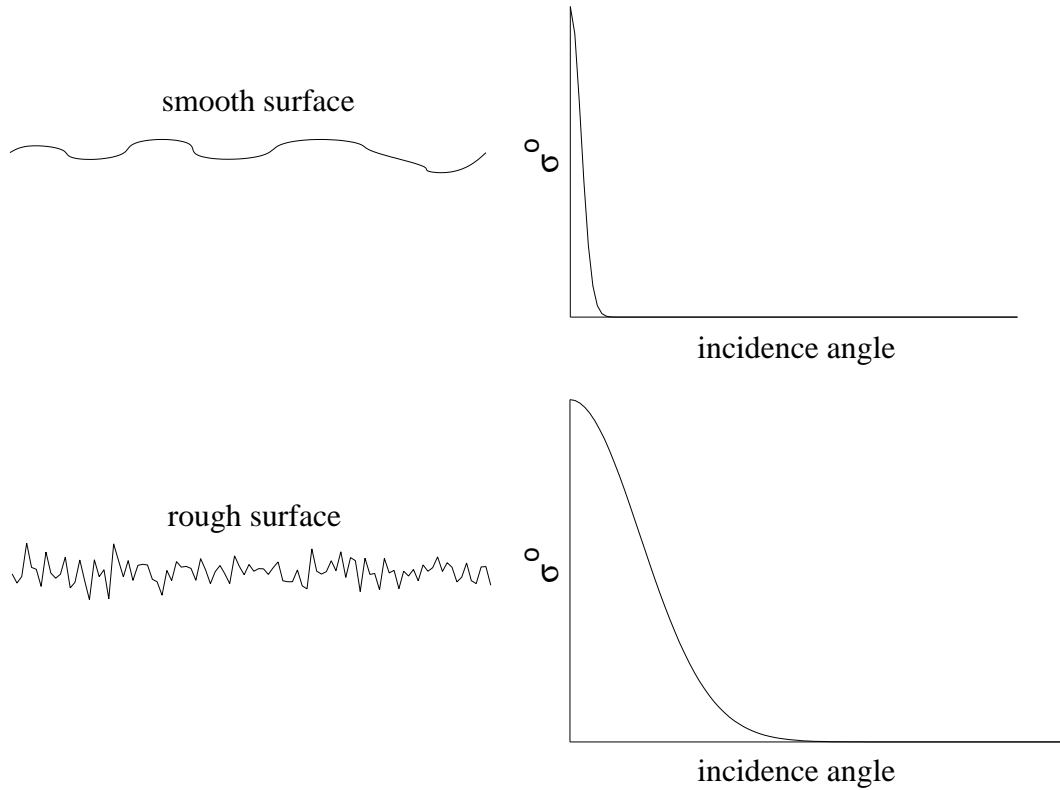
Figure 2.2: Surface scattering from a smooth surface is drops rapidly with increasing incidence angle while the fall-off for a rough surface is less steep.

In general, σ° is a composite of both surface and volume scattering, i.e.

$$\sigma^\circ = \sigma^\circ_{\text{vol}} + \sigma^\circ_{\text{surf}}.$$

Surface scattering originates from the boundary between two distinct mediums. Volume scattering is due to variations in the electro-magnetic properties within a medium. The largest $\sigma^\circ_{\text{surf}}$ is at nadir where specular scattering dominates. At off-nadir angles, the drop in $\sigma^\circ_{\text{surf}}$ is dependent on the roughness of the surface. Backscatter decreases more rapidly with increasing incidence angle for smoother surfaces (see Fig. 2.2). Further discussion on volume and surface scattering along with physical models are provided in Chapters 3 and 5.

2.2 Brightness Temperature

Brightness temperature is a measure of the microwave emission naturally radiating from a surface. Because a microwave radiometer only receives and does not transmit a signal, this is termed a passive measurement and the radiometer which measures T_b is termed a passive instrument.

The brightness temperature is related to the surface temperature (T) in Kelvin through the Rayleigh-Jeans approximation [26]

$$T_b = eT$$

where e is the emissivity of the surface. Because T_b is coupled to the dielectric properties as well as the temperature of the surface, it is in some respects more difficult to relate to the geophysical properties of the surface than is σ°.

A useful tool in modeling the T_b radiating from a surface is the *equation of transfer*. Given $T_b(0)$, the brightness temperature at r is [26, pg. 216]

$$T_b(r) = T_b(0)e^{-\tau(0,r)} + \int_0^r \kappa_e(r')\left[(1-a)T(r') + aT_{sc}(r')\right]e^{-\tau(r',r)}\,\mathrm{d}r' \qquad (2.4)$$

where the variables are

$T_b(0)$ - brightness temperature entering the layer,

κ_e - extinction coefficient $(\kappa_a + \kappa_s)$,

κ_a - absorption loss coefficient,

κ_s - scattering loss coefficient,

a - albedo (κ_s/κ_e),

$T(r)$ - physical temperature in Kelvin,

$T_{sc}(r)$ - scattered radiometric temperature, and

$\tau(r',r)$ - optical length $(\int_{r'}^r \kappa_e\,\mathrm{d}r)$.

Although not explicitly stated, the radiation is assumed to be in the direction of $\hat{r}$. The term inside the integral including $T(r')$ represents self-emission and the term involving $T_{sc}(r')$ represents scattering of radiation from other directions into the direction of $\hat{r}$.
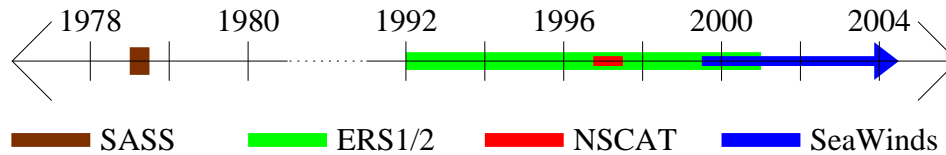
Figure 2.3: Time-line of the operation intervals for various scatterometers.

2.3 Sensors

Multiple microwave scatterometers have been used to measure the σ° of the Earth's surface within the last 25 years (see Fig. 2.3). NASA has collected σ° measurements from three Ku-band (~ 14 GHz) scatterometers. The Seasat-A scatterometer collected data for 3 months in 1978. For 9 months during 1996 and 1997 the NSCAT scatterometer collected data aboard the Japanese ADEOS-I platform. SeaWinds on QuikSCAT has continually collected σ° measurements from mid 1999 to the present. The European Space agency has flown a C-band (5.3 GHz) microwave scatterometer aboard the ERS-1 and ERS-2 satellites giving continuous data from 1992 though the beginning of 2001. A summary of the statistics for these instruments is provided in Table 2.1.

There is also a continuous set of T_b measurements from 1979 to the present. These measurements were obtained using the Nimbus-7 Scanning Multichannel Microwave Radiometer (SMMR) and the Defense Meteorological Satellite Program (DMSP) Special Sensor Microwave Imager (SSM/I) series. SSM/I measures T_b at 53° incidence angle using 7 different channels. The polarization and frequency of these channels are listed in Table 2.2.

2.4 Data Processing

The measurements from each of these sensors are in raw form with pseudo-random sampling in location and time. For analysis it is convenient to process the data, resampling at regular intervals in space and time. Various methods such as the

Table 2.1: Information on the various scatterometers used in this work.

	SASS	ERS-1/2	NSCAT	SeaWinds
FREQUENCY	14.6 GHz	5.3 GHz	13.995 GHz	13.6 GHz
AZIMUTHS				
POLAR.	V-H, V-H	V ONLY	V, V-H, V	V-OUTER/H-INNER
BEAM RESOLUTION	FIXED DOPPLER	RANGE GATE	VARIABLE DOPPLER	PENCIL-BEAM
SCI. MODES	MANY	SAR, WIND	WIND ONLY	WIND/HI-RES
RESOLUTION	50/100 km	25/50 km	25/50 km	25 km/6x25km
SWATH		500	600 600	1100,1600
INCIDENCE ANGS	0° –70°	20° –70°	17° –62°	42° & 54°
DAILY COVERAGE	VARIABLE	< 41 %	78 %	92 %
DATES	6/78 – 10/78	92–96 & 96–01	8/96 – 6/97	7/99 –
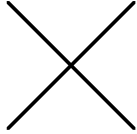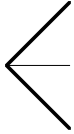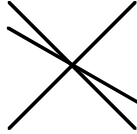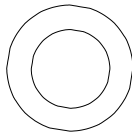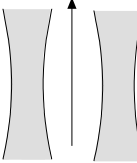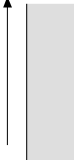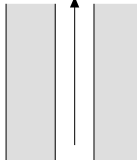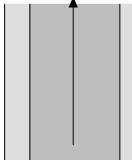
Table 2.2: Frequency and polarization of the 7 channels of the SSM/I radiometer [27].

Channel	Frequency (GHz)	Polarization
1	19.35	vertical
2	19.35	horizontal
3	22.235	vertical
4	37.0	vertical
5	37.0	horizontal
6	85.5	vertical
7	85.5	horizontal

Scatterometer Image Reconstruction (SIR) algorithm [28] have been developed for this purpose.

I adopt a simple algorithm similar to the averaging method used in the first iteration of SIR processing. This method is fast and simple, requiring only one iteration, although it results in lower resolution than SIR. Because the Greenland ice-sheet is relatively uniform, high resolution is not critical. For an imaging grid I consistently use 8.9 km x 8.9 km spacing based on a Lambertian projection. For parameter estimation at a given pixel all measurements with centroids within a 25 km radius of the pixel center are included. The measurement estimate for a given pixel at time τ is obtained using the non-parametric fit

$$x(\tau) = \frac{\sum_{i=1}^{N} x_i w(\tau, t_i)}{\sum_{i=1}^{N} w(\tau, t_i)} \tag{2.5}$$

where N is the number of measurements (x) within the specified radius. The weighting function varies with the applications. Typical weighting functions include a rectangular window function

$$w(\tau, t_i) = \begin{cases} 1 & \text{if } |t_i - \tau| \leq \Delta t_{\max}, \\ 0 & \text{if } |t_i - \tau| > \Delta t_{\max}. \end{cases}$$

and a truncated Gaussian

$$w(\tau, t_i) = \begin{cases} e^{-\frac{1}{2}(t_i - \tau)^2/\sigma_t^2} & \text{if } |t_i - \tau| \leq \Delta t_{\max}, \\ 0 & \text{if } |t_i - \tau| > \Delta t_{\max}. \end{cases}$$

Much of my work employs linear models where σ° is modeled in terms of incidence angle, azimuth angle, and possibly other terms. The model parameters are obtained using least-squares estimation. The general form of this model is

$$\sigma_i^\circ = c_0 + c_1 b_{i1} + c_2 b_{i2} + \cdots + c_N b_{iN}$$

The model parameters (c_n) are estimated using the weighted least-squared error solution to

$$\begin{bmatrix} 1 & b_{11} & b_{12} & \cdots & b_{1N} \\ 1 & b_{21} & b_{22} & \cdots & b_{2N} \\ \vdots & \vdots & \vdots & \ddots & \vdots \\ 1 & b_{M1} & b_{M2} & \cdots & b_{MN} \end{bmatrix} \begin{bmatrix} c_0 \\ c_1 \\ \vdots \\ c_N \end{bmatrix} = \begin{bmatrix} \sigma_1^\circ \\ \sigma_2^\circ \\ \vdots \\ \sigma_N^\circ \end{bmatrix}$$

where the weighting is that of the non-parametric fit described above. For an example, let us assume a model of the form

$$\sigma^\circ = c_0 + c_1(\theta - 40) + c_2(\theta - 40)^2$$

where θ is the incidence angle dependence. For this case, $b_{i1} = \theta_i - 40$ and $b_{i2} = (\theta_i - 40)^2$ are the definitions of the two bases in the model.

2.5 Greenland

Greenland has a unique environment. It is the largest island in the world. The distance from the most northern point to the most southern point is over 1500 miles, about the distance from the Canadian border to the southern tip of Texas. The distance from east to west is about 700 miles, further than the distance from Salt Lake City to the Pacific Ocean. The majority of Greenland is covered by a large ice sheet. About 8 percent of the total volume of ice on earth is located there [2].

Greenland is almost completely covered by a thick layer of snow and ice. Near the summit, this snow layer is over 3 km deep [29]. Because the snow is so deep, ground features are almost entirely masked out, leaving a surface with mountains present only on the periphery of the ice sheet (see Fig. 3.1 (c)).

The topography of Greenland makes it unique. Sixty-five percent of Greenland is over 2000 m in elevation, a relative distribution found on no other significant land mass except for Antarctica. A histogram of the elevation distribution is shown in Fig. 2.5. Although high in elevation, the ice sheet itself is relatively flat. The 3-dimensional image of Greenland in Fig. 2.4(a) illustrates how smooth and high in elevation the interior of the ice sheet is. Figure 2.4(b) shows more topography data including elevation, slope, and slope orientation. The Greenland summit (3278 m) is indicated in the slope orientation image. A second summit (2850 m) is also indicated on the southern portion of the ice-sheet.

Because of the associated cost and other difficulties, *in situ* data from Greenland is scarce relative to the size of the ice sheet. Greenland is one of the final frontiers with human exploration of the ice-sheet relatively recent. The first

16

elevation   gradient   upslope direction

1500   m   3278   0   m/km   25   0   deg rel. to north   360

(a)   (b)
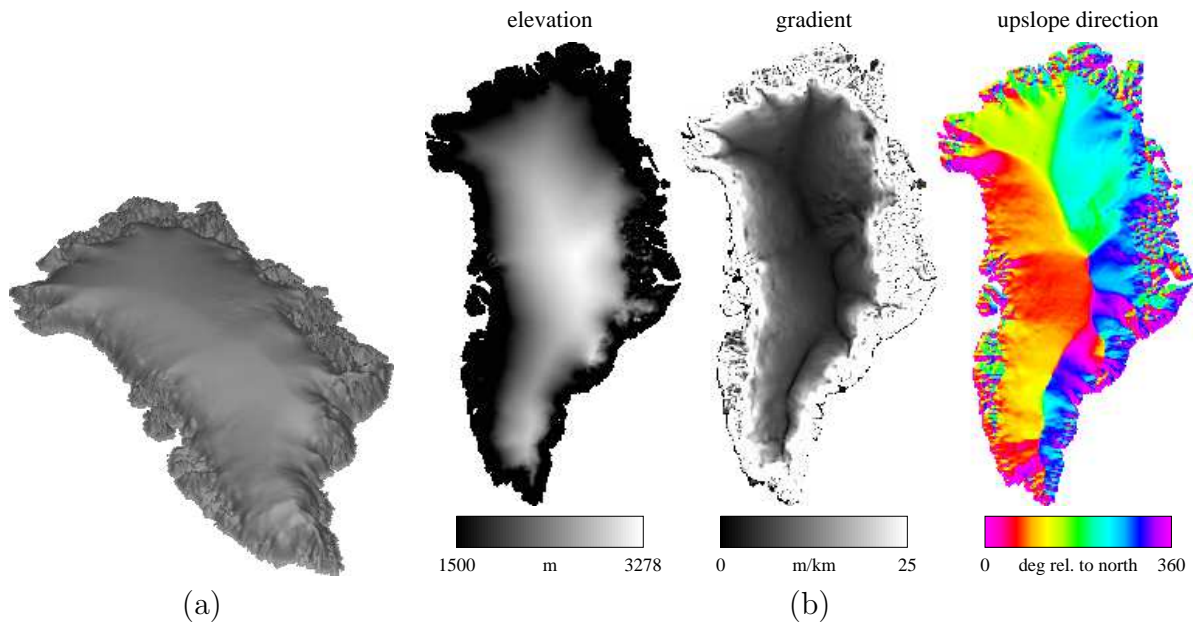
Figure 2.4:   (a) 3-dimensional image of Greenland. The vertical scale is exaggerated.
(b) Topography characteristics of Greenland.
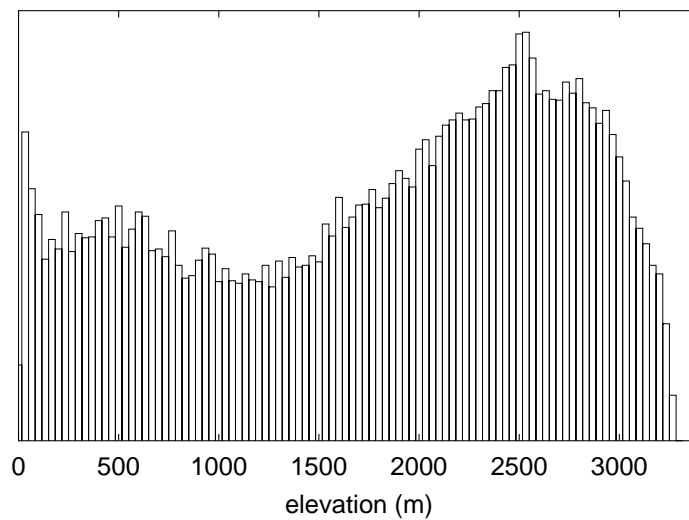
elevation (m)

Figure 2.5:   Histogram showing the elevation distribution over Greenland.

record of human crossing of the ice sheet is in 1888 when Fridtjof Nansen and his team successfully traversed the southern portion of the ice-sheet traveling by skis from the east to the west coast [29]. Throughout the twentieth century exploration of Greenland has constantly been increasing. Even with modern technology many obstacles still prevent thorough investigation. Most travel to the interior of the ice sheet is done by air due in part to obstacles in the marginal zone near the edge of the ice sheet.

One of the most extensive studies of the Greenland ice sheet was performed by the United States SIPRE project [30]. The field work for the project was performed from 1952 to 1955. This study includes extensive snow pit data which give insights into accumulation and melt processes over Greenland. Data from this study is still used today to further understand the properties of the ice sheet.

In his report for the SIPRE project, Benson [30] defines four basic ice facies. As an understanding of the ice facies types is critical to Greenland studies, a brief description of each is given here.

Ablation facies - The area around the periphery of Greenland where the yearly snow accumulation completely melts during the summer leaving a surface of glacial ice and rock.

Soaked or wet snow facies - During the summer melt, the accumulated snow for the previous year becomes completely saturated with snow. The boundary between the ablation and wet snow facies is termed the firn line.

Percolation facies - Some melting occurs, but the snow does not become saturated with water. The liquid water that forms percolates down through a network of channels which later freeze forming ice pipes and ice lenses. The boundary between the wet snow facies and the percolation facies is termed the saturation line,

Dry snow facies - The area at the interior of the ice sheet that is at a high enough elevation that summer melt is negligible. The boundary between the percolation and dry snow facies is termed the dry snow line.

The locations of these facies as given by Benson are illustrated in Fig. 2.6. An updated facies map derived from SASS meaurements [6] is shown in Fig. 2.7 along with an ERS $\sigma°$ image. A discussion of the scattering properties of the different snow zones is contained in Chapter 4.
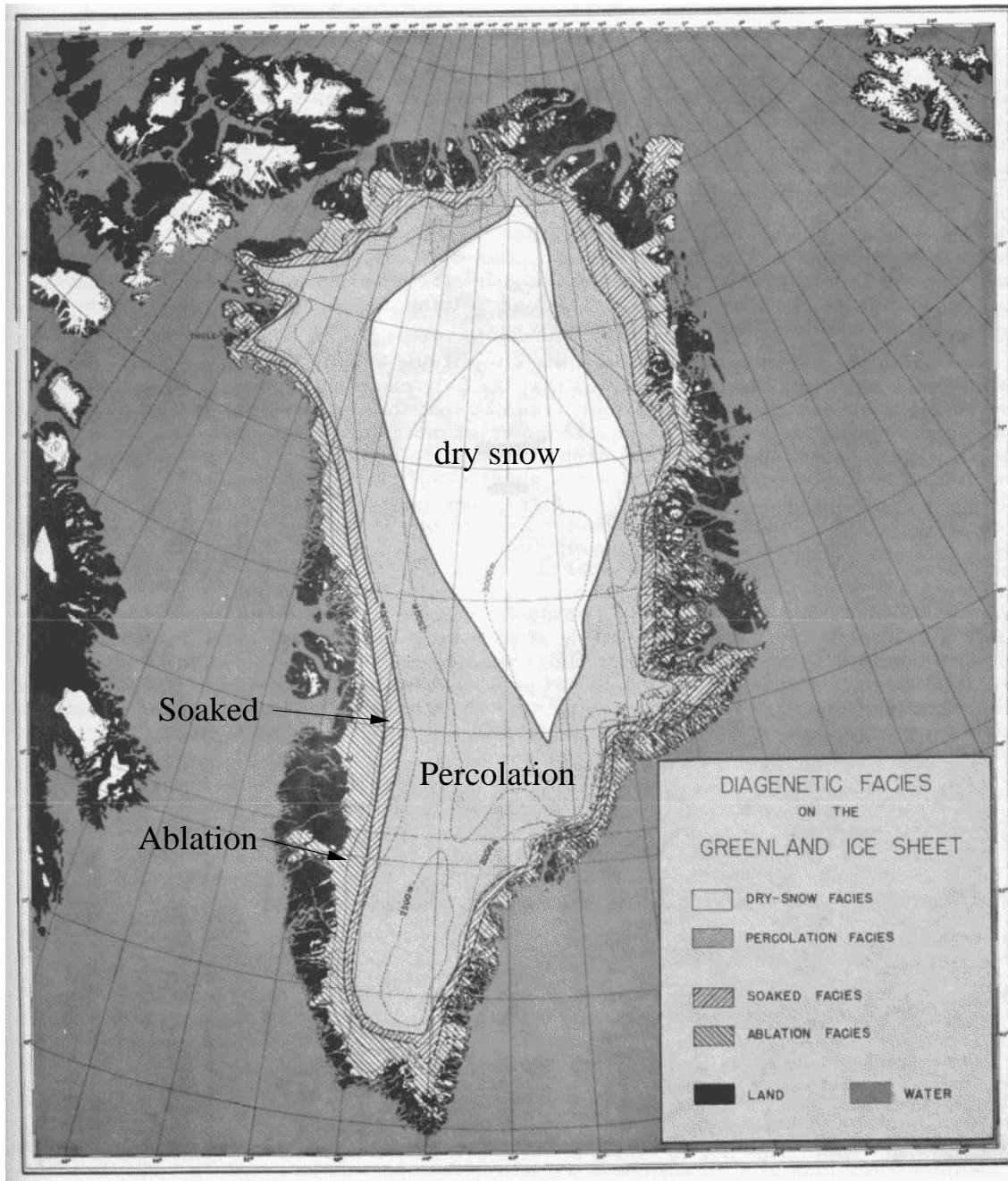
Figure 2.6: Greenland ice facies regimes as defined by Benson [30].
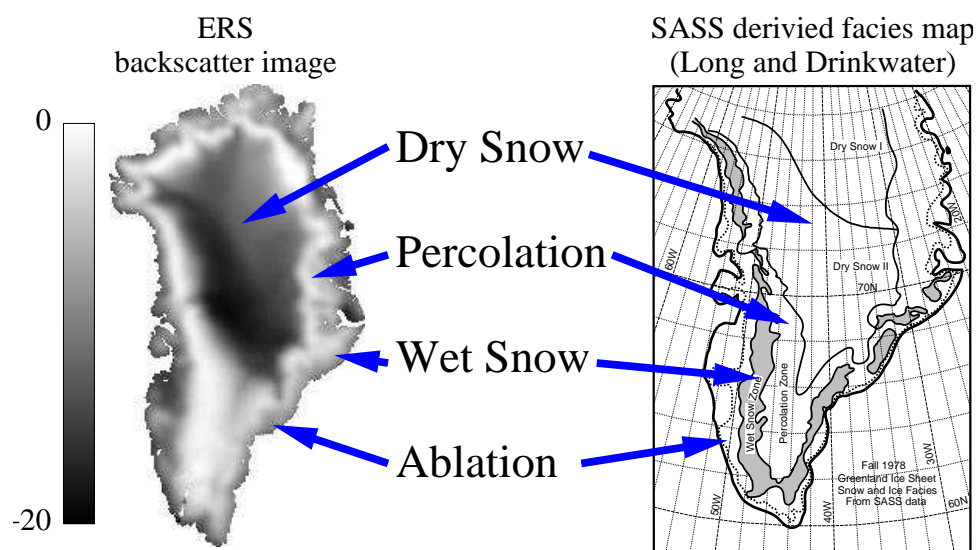
Figure 2.7: (left) ERS $\sigma°$ image normalized to 40° incidence angle. (right) Greenland ice facies map derived from SASS $\sigma°$ measurements from Long and Drinkwater [6].

Chapter 3

Azimuth Modulation Physical Model

An understanding of the relationship between $\sigma°$ azimuth dependence and physical properties of the surface is valuable for enhancing our understanding of the dynamics of the ice sheet. Past studies employing $\sigma°$ measurements over Greenland have assumed azimuth modulation to be negligible. However, as remote sensing studies become more refined, extracting the relationship between the azimuth variation and surface features is necessary for characterizing processes related to long term change. My investigations have found azimuth modulation to be relatively stable over time making it a potential indicator for long term change. The key to this application is relating this change to surface properties.

This chapter presents a simple surface scattering model relating physical properties of the surface to observed azimuth modulation of $\sigma°$. The chapter is organized as follows: First is a background discussion of the data and previous research on azimuth modulation over snow. Next, a simple surface scattering model is presented which includes azimuth modulation. This model is inverted using data from two study locations and the results are discussed. Finally, the model is inverted for the entire ice sheet and the resulting estimates of geophysical surface properties are discussed.

3.1 Background

This study employs data from ERS which has a fan-beam design with three fixed antennas, each measuring $\sigma°$ at a different azimuth angle. Combining ascending and descending passes, ERS provides azimuth sampling at approximately

6 distinct azimuth angles at any given location. Azimuth sampling is fundamental to the primary purpose of ERS which is to measure vector winds over the ocean. Wind retrieval is achieved by inverting an empirical model of the azimuth dependence of σ° as a function of wind speed and direction. I use the azimuth sampling of ERS to estimate parameters of a physical model of the azimuth dependence of σ° over Greenland. The data used in this study spans a 30 day interval beginning Julian Day (JD) 330 and ending JD 360, 1996 which is during the winter when the backscatter of the Greenland surface is relatively constant.

Much of the analysis focuses on data from the Tunu-N (78.0 N, 34.0 W) and NASA-U (73.83 N, 49.5 W) sites (see Fig. 3.1). The raw data at each location comprises all ERS σ° measurements which lie within a 30 km radius of the location center. Figure 3.2 shows azimuth modulation observed in the raw data. The azimuth modulation at the Tunu-N site is over 3 dB peak-to-peak and the modulation at the NASA-U site is about half this magnitude.

Azimuth modulation of σ° has been observed over both Antarctica and Greenland. Over Antarctica, the orientation of the modulation is highly correlated with the wind direction [22, 23, 24]. Over Greenland, azimuth modulation of σ° over was first observed by Swift et al. [31] at a location in the southern percolation zone. The modulation was observed in an aircraft banking maneuver during which the scatterometer remained focused on a specific location. The observed modulation is approximately 1 dB for σ° at Ku-band and is primarily first order (a single cycle for 360°).

My analysis indicates that the largest azimuth modulation at both C-band and Ku-band occurs in the dry snow of central and northern Greenland where it is primarily second order [32]. The orientation of the azimuth modulation matches the general flow of the winter-time katabatic[1] wind field as modeled by Bromwich et al. [33].

---

[1]Katibatic winds are formed by cooling of the near-surface air which increases the air density causing it to be accelerated down-slope by gravity.
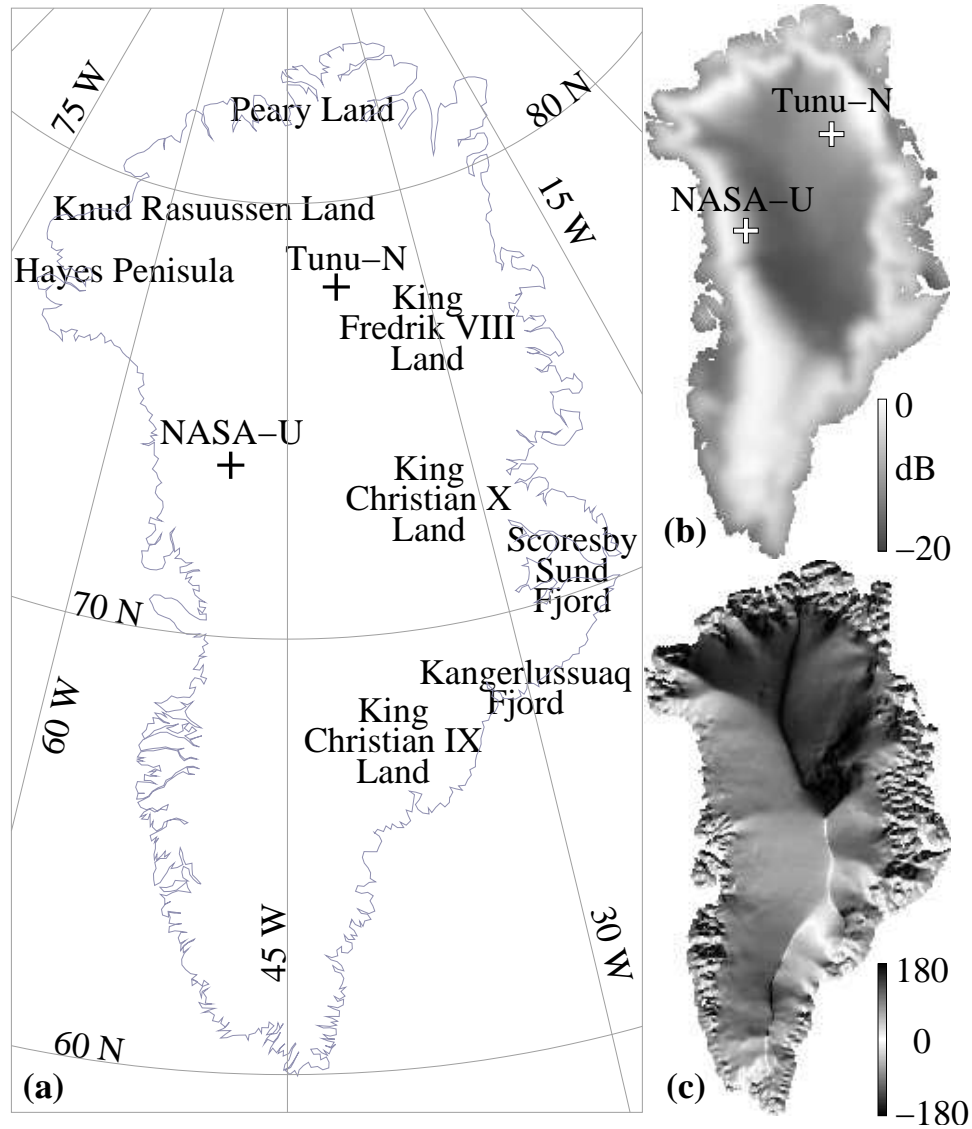
Figure 3.1: (a) Map of Greenland. (b) ERS backscatter image showing $\sigma°$ at 40° incidence angle with the two study sites indicated. (c) Image of the direction of the gradient of the Greenland surface topography.
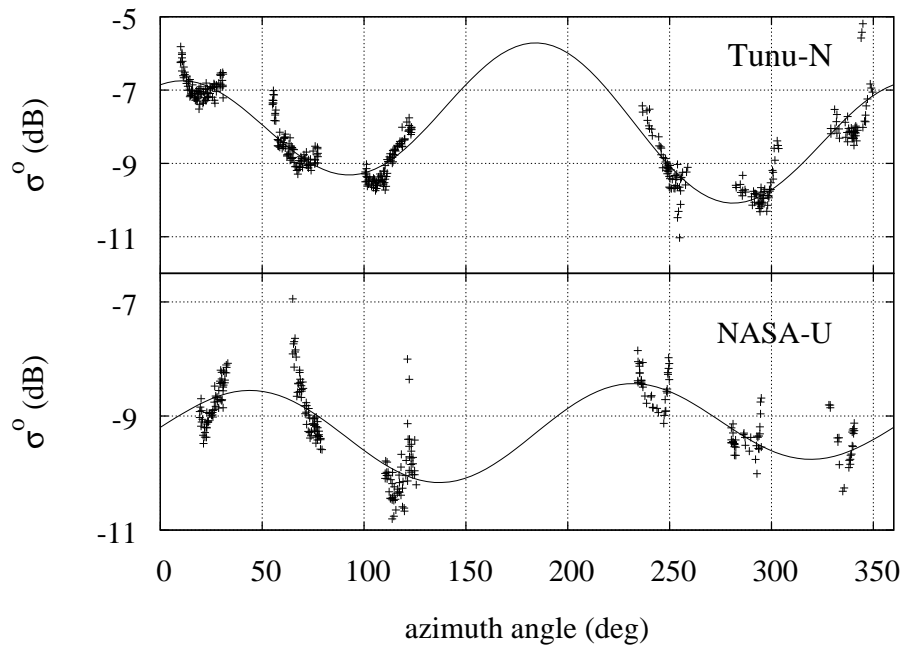
Figure 3.2: Azimuth modulation observed in the ERS backscatter at the two study location indicated in Fig. 3.1. The circles represent the raw ERS measurements normalized to 40° incidence based on a linear dependence on incidence angle. The line is a second order sinusoid fit to the data.

Over Antarctica, azimuth modulation of $\sigma°$ is attributed to wind-formed surface features termed sastrugi [22, 23, 24]. Sastrugi are erosional or depositional surface features which are aligned such that the crest is parallel to the wind direction. They range in scale from 10 to over a hundred meters [34]. Over Antarctica, azimuth modulation is primarily second order with the orientation highly correlated with the katabatic wind flow [24].

Although azimuth modulation is attributed to sastrugi on the surface, there is a lack of physical models directly relating snow surface properties to azimuth modulation of $\sigma°$. I propose a simple surface scattering model which relates azimuth modulation to physical surface properties. My model assumes that sastrugi and other features of the same scale are the primary mechanism driving the modulation, which is consistent with second order azimuth modulation such as that observed over much of the Greenland ice sheet and Antarctica.

3.2   Surface Scattering Model

The proposed model for the simulation of the effects of sastrugi on $\sigma°$ over Greenland is composed of two scales. In my model, roughness of the order of a radar wavelength (5.7 cm) or smaller is termed *small-scale* roughness. Roughness at scales from a few meters to a few kilometers is termed *meso-scale* roughness. Features at this scale are larger than a wavelength and smaller than the dimensions of the measurement footprint. Features at scales larger than the size of the satellite footprint (50 km) are termed *large-scale*. Roughness at scales in between these levels is assumed to be negligible. The surface is modeled as a composite of small-scale roughness and meso-scale roughness as illustrated in Fig. 3.3 (a).

While formulated as a surface scattering model, the scattering model represents an effective bulk equivalent to the actual multi-layer surface including multilayer interaction and volume scattering, since the Greenland snow-pack consists of multiple layers with each layer roughly equivalent to a years' accumulation (see Fig. 3.3 (b). Backscatter from internal layer boundaries may affect the model estimates of

(a)   Composite surface

small–scale roughness

meso–scale roughness

(b)   Air

Snow Layers
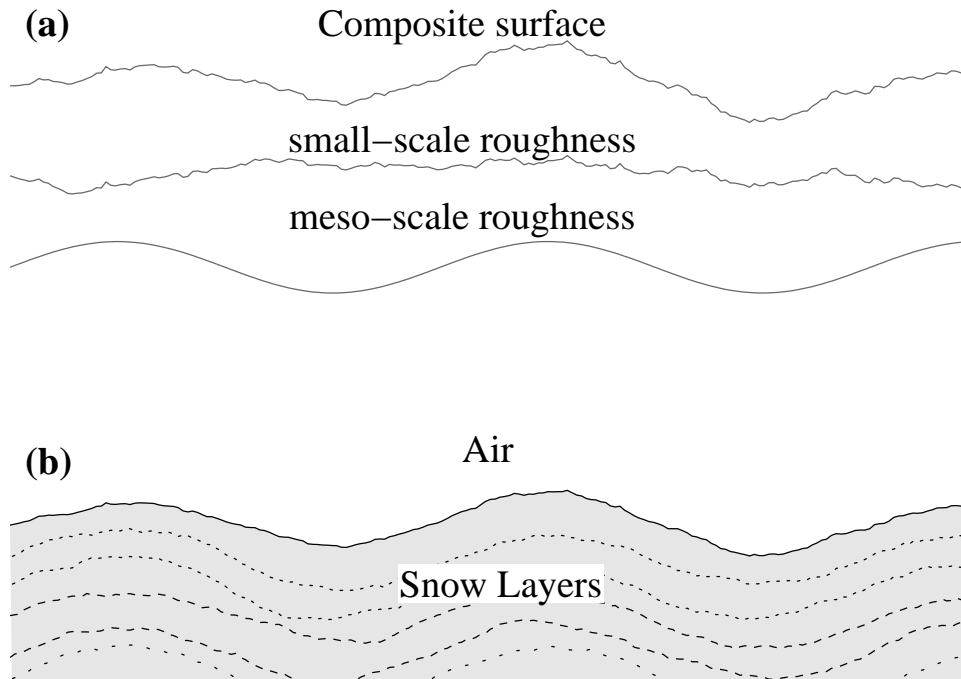
Figure 3.3: (a) The snow surface is modeled as the composite of roughness at two-scales: a meso-scale variation which is much larger than the electro-magnetic wavelength and a small-scale perturbation with variations of the order of a wavelength and smaller. (b) The actual surface includes multiple layers. The model represents the net effective response for both the surface and the interaction between multiple layers (see text).

surface roughness. This effect is expected to be small for an individual layer because the dielectric difference between layers is small compared to at the air/snow boundary. However, the combined contribution from multiple layers may be significant, especially for ERS which has a much larger penetration depth than Ku-band scatterometers.

The model assumes the small-scale roughness is isotropic and is the primary factor in local incidence angle dependence of σ°. The meso-scale roughness is assumed, in general, to be anisotropic, resulting in azimuth modulation of σ°. To model the meso-scale roughness, the snow surface is viewed as a mesh of individual flat surfaces. The dimensions of each mesh element are assumed to be large compared with the incident wavelength. The satellite observed large-scale backscatter (σ_{ls}°) is the ensemble average of the small-scale backscatter (σ_{ss}°) from the meso-scale mesh elements, i.e.

$$\sigma_{ls}^\circ(\theta, \phi) = \int_0^{\pi/2} \sigma_{ss}^\circ(\theta') P(\theta'|\theta, \phi) \, \mathrm{d}\theta' \tag{3.1}$$

where $P(\theta'|\theta, \phi)$ is the probability distribution of the local incidence angle. The local incidence angle distribution can be obtained from the surface slope distribution given the observation geometry. Because our model assumes that each mesh element is azimuthally isotropic, σ_{ss}° is only a function of the local incidence angle (θ').

For evaluating the contribution of the azimuth anisotropy in the meso-scale roughness to the model accuracy, results from this general model are compared with the results from a form of the model constrained to be azimuthally isotropic in surface roughness. The general model for which the meso-scale surface roughness is anisotropic is termed the *A-model*. The form of the model constrained to isotropic surface roughness is termed the *I-model*. Additionally, these two models are compared with a form of the model where the meso-scale surface is constrained to be flat, which I term the *F-model*. In the F-model $P(\theta'|\theta, \phi) = \delta(\theta' - \theta)$ and Eq. (3.1) becomes $\sigma_{ls}^\circ(\theta, \phi) = \sigma_{ss}^\circ(\theta)$ where $\delta(\cdot)$ is the Dirac delta function.

3.2.1 Meso-scale model

The probability distribution of the local incidence angle, $P(\theta'|\theta, \phi)$, is directly related to the meso-scale slope distribution $P(\vec{s})$ where $\vec{s} = [\, s_x \; s_y \,]^T$ are the slopes in the x and y direction. Assuming that $\vec{s}$ is zero-mean and Gaussian distributed,

$$P(\vec{s}) = \frac{1}{2\pi |R|^{1/2}} e^{-(1/2)\vec{s}^T R^{-1} \vec{s}} \tag{3.2}$$

where R is the covariance matrix. The surface slope covariance R has a physical interpretation in terms of a RMS slope as a function of azimuth. The singular value decomposition

$$R = U\Sigma U^T \tag{3.3}$$

provides estimates of the minimum and maximum one-dimensional RMS slope and the associated azimuth angles. Let

$$\Sigma = \begin{bmatrix} \xi_1^2 & 0 \\ 0 & \xi_2^2 \end{bmatrix} \tag{3.4}$$

and

$$U = [\vec{u}_1 | \vec{u}_2] \,. \tag{3.5}$$

Formulas for obtaining the SVD are given in Appendix B. ξ_1 is the maximum one-dimensional RMS surface slope which is in the direction of $\vec{u}_1$ and ξ_2 is the minimum one-dimensional RMS surface slope which is in the $\vec{u}_2$ direction. For the case of the I-model, R is constrained to the form $R = \xi I$ where I is the identity matrix.

The simplified slope probability distribution in Eq. (3.2) is related to the size and orientation of sastrugi over a snow field. The distribution defines how the RMS slope of a cross-section of the surface varies with direction. Over sastrugi, the RMS slope is expected to be a maximum when the cross-section is orthogonal to the crests of the sastrugi and minimum when the cross-section is parallel to the sastrugi crests. Because the crests of the sastrugi are aligned with the wind direction [34] $\vec{u}_1$ coincides with the cross-wind direction and $\vec{u}_2$ coincides with the up/down wind direction. ξ_1 is an estimate of the RMS slope of the sastrugi.

3.2.2 Small-scale model

The other surface property required to evaluate Eq. (3.1) is the small-scale dependence of σ° on incidence angle ($\sigma_{ss}^\circ(\theta')$). Backscatter over snow is a combination of both volume and surface scattering. Near nadir, surface scattering dominates, while at larger incidence angles volume scattering has a more significant contribution. The total backscatter at any incidence angle is the sum of these two components, i.e.

$$\sigma_{ss}^\circ(\theta') = \sigma_{surf}^\circ(\theta') + \sigma_{vol}^\circ(\theta'). \tag{3.6}$$

The Small Perturbation Method (SPM) is used to model surface scatter, which is appropriate for roughness scales of the order of the incident wavelength or smaller. SPM is also used by Ledroit et al. [22] in modeling backscatter over the Antarctic ice sheet. There are two key differences between my implementation of SPM and that of Ledroit et al. First, Ledroit et al. assume an azimuth dependent form of SPM to account for azimuth modulation. However, SPM is only valid for roughness smaller than the incidence wavelength (5.7 cm for ERS). I assume the surface is isotropic at the SPM scale and that azimuth dependency is caused by surface tilt due to meso-scale features which is consistent with the theory that sastrugi are the primary mechanism for azimuth modulation. Second, I assume a Gaussian surface correlation function as opposed to the exponential correlation function used by Ledroit et al. This is done because the Gaussian correlation function results in model estimates more consistent with the σ° measurements.

For SPM [25],

$$\sigma_{surf}^\circ(\theta') = 8k^4\sigma^2\cos^4\theta'|\alpha_{pp}(\theta')|^2 W(2k\sin\theta') \tag{3.7}$$

where k is the wave number in free space, σ is the surface RMS height, and l is the surface correlation length. The α_{pp} term is dependent upon polarization (p). For the vertical-vertical ERS polarization [25]

$$\alpha_{vv}(\theta') = (\epsilon_r - 1)\frac{\sin^2\theta' - \epsilon_r(1+\sin^2\theta')}{\left[\epsilon_r\cos\theta' + (\epsilon_r - \sin^2\theta')^{1/2}\right]^2}$$

where ϵ_r is the relative dielectric constant of the surface. $W(\cdot)$ is the power spectrum of the surface. Assuming a Gaussian correlation function, the roughness spectrum is [25]

$$W(2k\sin\theta') = \frac{1}{2}l^2 e^{-(kl\sin\theta')^2}. \tag{3.8}$$

For volume scattering I use the same model as Swift [35],

$$\sigma_{vol}^\circ(\theta') = T^2(\theta')\frac{n\sigma_b}{2\alpha}\cos\theta' \tag{3.9}$$

where $T(\theta')$ is the plane wave power transmission coefficient, n is the number density of scatters per unit volume, σ_b is the radar cross-section of a single scatter, and α is the bulk volume attenuation coefficient. Combining Eqs. (3.6)-(3.9) results in

$$\sigma_{ss}^\circ(\theta') = 4k^4\sigma^2l^2\cos^4\theta'|\alpha_{pp}(\theta')|^2 e^{-(kl\sin\theta')^2} + T^2(\theta')\frac{n\sigma_b}{2\alpha}\cos\theta'. \tag{3.10}$$

The performance of Eq. (3.10) in matching the ERS measurements is evaluated by fitting the model to the ERS data at a location where the surface is relatively flat and minimal azimuth modulation is observed. Figure 3.4 shows a least-squares fit of Eq. (3.10) to ERS data from 73.25 N, 37.28 W, which is near the summit where the azimuth variation in σ° is negligible. The method used to obtain the least-squared error model estimates is described in the next section. Model roughness estimates for this location are $kl = 3.22$ and $k\sigma = 0.498$. The upper limit for the valid region of SPM is $k\sigma < 0.3$ [25]. Because the estimate obtained for $k\sigma$ is somewhat larger than this limit, care must be used when interpreting these parameters in terms of actual surface roughness values. However, as observed in Fig. 3.4, the model provides a good fit to the data and thus is useful as an empirical model describing the local incidence angle dependence of σ°. Also, as discussed in Section 3.2, Eq. (3.10) is a bulk equivalent model representing the snow-pack, which consists of many layers, as one single layer. Therefore, the surface roughness parameters represent an equivalent single layer roughness estimate for a multi-layered surface. The Small Slope Approximation (SSA) is a possible alternative to SPM for future studies as SSA is valid for larger roughness scales [36]. SSA is not used here because it adds significant complexity to the model and the model inversion process. The quality of the fit and the simplicity provided by the SPM model is deemed appropriate for this initial study.
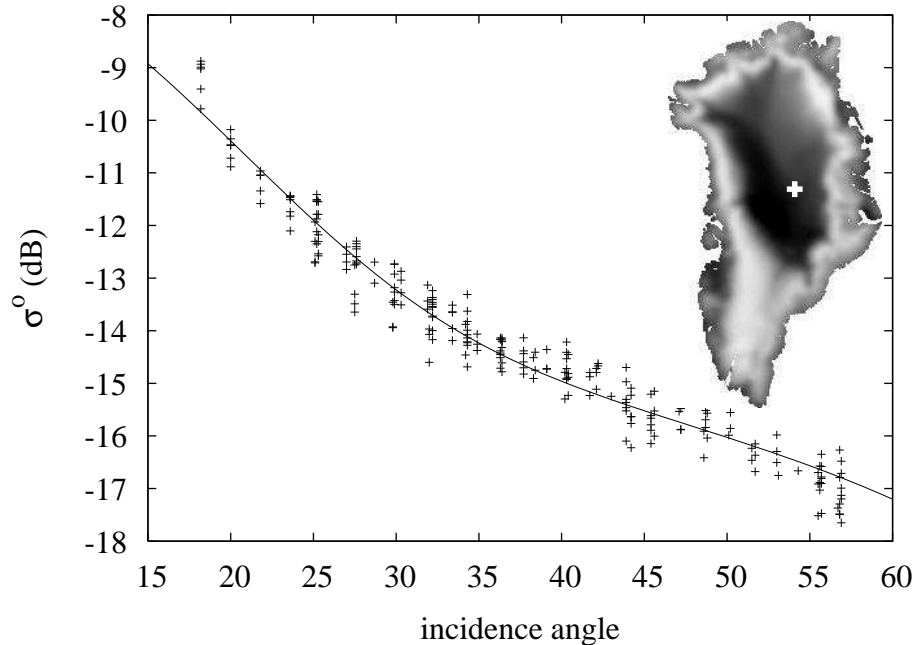
Figure 3.4: A least-squares fit of the small-scale model to ERS data at 73.25 N, 37.28 W, which is near the summit where azimuth modulation in the ERS data is negligible.

3.2.3 Model inversion

Estimation of surface parameters from σ° measurements requires inversion of the surface model. The model inversion is obtained by minimizing the RMS error

$$\chi = \left[(\vec{\sigma}^\circ - \vec{\sigma}^\circ_{ls})^T (\vec{\sigma}^\circ - \vec{\sigma}^\circ_{ls}) \right]^{1/2} \tag{3.11}$$

where $\vec{\sigma}^\circ$ is a vector of the measurement values and $\vec{\sigma}^\circ_{ls}$ is a vector of the model estimates. The minimization of Eq. (3.11) with respect to the model parameters is a second order non-linear regression problem. We solve it using the iterative Levenberg-Marquardt technique [37]. On the base level, the small-scale model parameters which minimize Eq. (3.11) are estimated for a given probability density $P(\theta'|\theta, \phi)$ which is obtained from a specified meso-scale slope covariance R. This process is iterated for different R values until the minimum of Eq. (3.11) is obtained.

The distribution $P(\theta'|\theta, \phi)$ is different for each measurement based on the measurement geometry. For each measurement the calculation of $P(\theta'|\theta, \phi)$ from the

surface slope covariance R is performed numerically. This is done by discretizing the range of surface slopes along with the associated probability for each slope combination. Each slope combination $\vec{s}$ is represented by a unit vector $\hat{\mathbf{z}}'$ orthogonal to the local surface. The corresponding local incidence angle is $\theta' = \cos^{-1}(\hat{\mathbf{z}}' \cdot \hat{\mathbf{r}})$ where $\hat{\mathbf{r}}$ is a unit vector in the θ, ϕ direction. Each surface slope combination is binned according to the local incidence angle θ' to obtain a discrete estimate of the local incidence angle distribution $P(\theta'|\theta, \phi)$.

Given $P(\theta'|\theta, \phi)$ the small-scale surface parameters which minimize Eq. (3.11) are obtained. To solve for the small-scale model parameters Eq. (3.10) is rewritten as

$$\sigma_{ss}^{\circ}(\theta') = P \cos^4 \theta' |\alpha_{pp}(\theta')|^2 e^{-Q \sin^2 \theta'} + T^2(\theta') V \cos(\theta') \qquad (3.12)$$

where $P = 4k^4 \sigma^2 l^2$, $Q = k^2 l^2$, and $V = \frac{n\sigma_b}{2\alpha}$ are used as the unknown parameters. To obtain α_{pp} and $T(\theta')$ we set $\epsilon_r = 1.7$, corresponding to a snow density of 0.38 g/cm [38, pg. 2061] which is typical of the densities observed by Benson [30, pg. 66] in the upper percolation facies. For each iteration of the non-linear least-squares regression, the two-scale model is evaluated using the discretized $P(\theta'|\theta_i, \phi_i)$ for each measurement, i.e.

$$
\begin{bmatrix}
\sigma_{ls}^{\circ}(\theta_1, \phi_1) \\
\sigma_{ls}^{\circ}(\theta_2, \phi_2) \\
\vdots \\
\sigma_{ls}^{\circ}(\theta_m, \phi_m)
\end{bmatrix}
=
\begin{bmatrix}
P(\theta_1'|\theta_1, \phi_1) & P(\theta_2'|\theta_1, \phi_1) & \cdots & P(\theta_n'|\theta_1, \phi_1) \\
P(\theta_1'|\theta_2, \phi_2) & P(\theta_2'|\theta_2, \phi_2) & \cdots & P(\theta_n'|\theta_2, \phi_2) \\
\vdots & \vdots & \ddots & \vdots \\
P(\theta_1'|\theta_m, \phi_m) & P(\theta_2'|\theta_m, \phi_m) & \cdots & P(\theta_n'|\theta_m, \phi_m)
\end{bmatrix}
\begin{bmatrix}
\sigma_{ss}^{\circ}(\theta_1') \\
\sigma_{ss}^{\circ}(\theta_2') \\
\vdots \\
\sigma_{ss}^{\circ}(\theta_n')
\end{bmatrix}
$$

$$(3.13)$$

or equivalently

$$\vec{\sigma}_{ls}^{\circ} = \mathbf{P} \vec{\sigma}_{ss}^{\circ}.$$

3.2.4 Results

The fit of the surface scattering model to the ERS σ° measurements is analyzed using two study areas. As mentioned in Section 3.1 the study areas are centered at the Tunu-N and NASA-U sites to enable comparison between Greenland Climate Network automatic weather station (AWS) *in situ* wind measurements and

model-produced preferential directions in the surface roughness. As discussed in Appendix A, the co-location bias in the data can be significant. This is especially true for locations in transition regions between facies such as the Tunu-N and NASA-U sites. Therefore, before inverting the model to fit the $\sigma°$ measurements, the co-location bias in the data is estimated and removed using the method outlined in Appendix A.

Estimates obtained through inverting the A-model provide a good fit to the data. Plots comparing A-model estimates to $\sigma°$ measurements are shown in Fig. 3.5 for Tunu-N and Fig. 3.6 for NASA-U. The model estimates show peak-to-peak azimuth modulation of over 3 dB at Tunu-N and up to 2 dB at NASA-U. At Tunu-N the variability of the data around the model estimates is generally smaller than 1 dB. The data is centered at the model estimate, indicating a good fit. At the NASA-U location the spread in the data at each azimuth is larger, in many cases over 2 dB, and not as consistently centered around the estimate. This apparent discrepancy is attributed in part to the incidence angle dependence of $\sigma°$. Over the 5° incidence angle range for each sub-plot, $\sigma°$ varies up to 1.5 dB depending on incidence angle.

A second plot for evaluating the fit of the model estimates to the data is provided in Fig. 3.5 (b) and Fig. 3.6 (d). These plots show the incidence angle dependence of the model at two azimuth angles along with $\sigma°$ measurements with azimuth angles within $\pm10°$. Here the incidence angle dependence of $\sigma°$ is distinctly different for the displayed azimuth ranges. At Tunu-N, the $\sigma°$ measurements around $\phi = 15°$ are consistently about 3 dB larger than the case where $\phi = 290°$. This behavior is matched by the model output. At NASA-U, the model estimates a 2 dB bias in the mean data with the larger backscatter at $\phi = 245°$ and the smaller at $\phi = 115°$. The model estimated bias is slightly larger than the spread observed in the $\sigma°$ measurements.

The performance of the A-model is evaluated by comparing the estimate errors with those of the I-model and the F-model. The RMS residual error as defined in Eq. (3.11) is used as the error metric. The A-model performs similarly at both
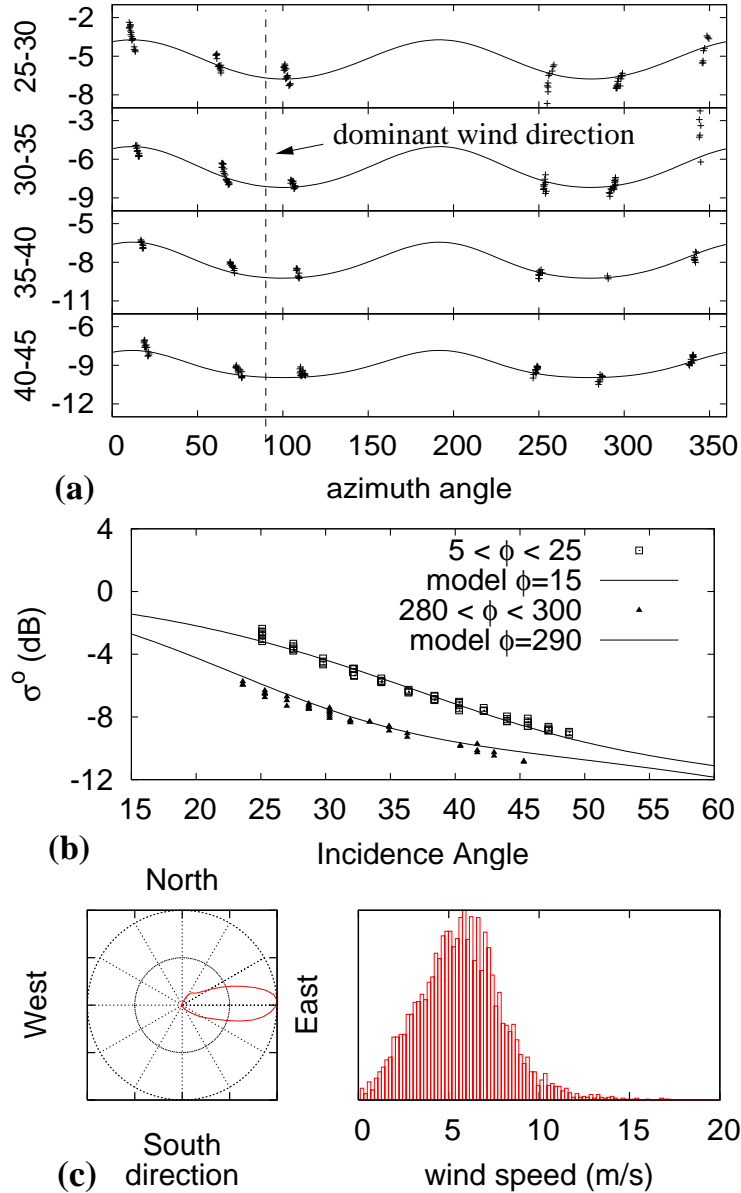
Figure 3.5: Illustration of the A-model fit to ERS σ° measurements at the Tunu-N (78.0 N, 34.0 W) site (see Fig. 3.1). (a) Plots of the azimth modulation observed in raw ERS measurments (indictated by "+" symbols). The data are divided into four incidence angle bins with the range of each bin indicated on the vertical axis. The lines represent the model fit to the raw data where θ is set to the center of the respective incidence angle range and ϕ varies along the horizontal axis. (b) Plots showing the incidence angle dependence of the raw data and the surface model fit. For each plot, raw ERS data from two ranges of ϕ are shown with the range indicated in the key. The line shows the A-model where ϕ is set to the center of each range indicated in the key and θ varies along the horizontal axis. (c) Wind statistics at each location during 1996 obtained from the Greenland Climate Network [39]. The left plot in (c) is a circular histogram of the wind direction while the right plot in (c) is a histogram of the wind speed.
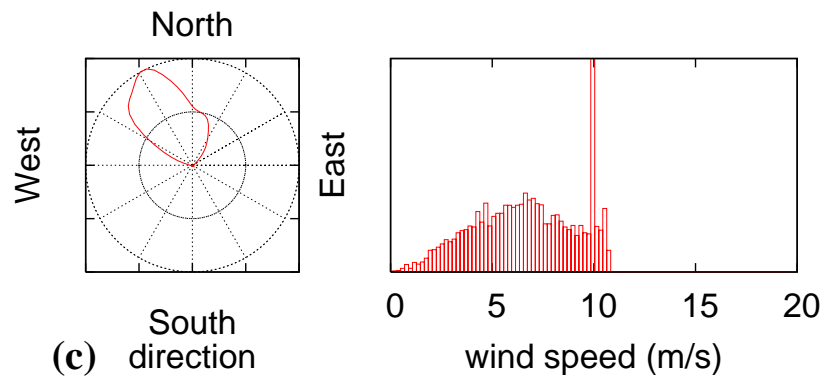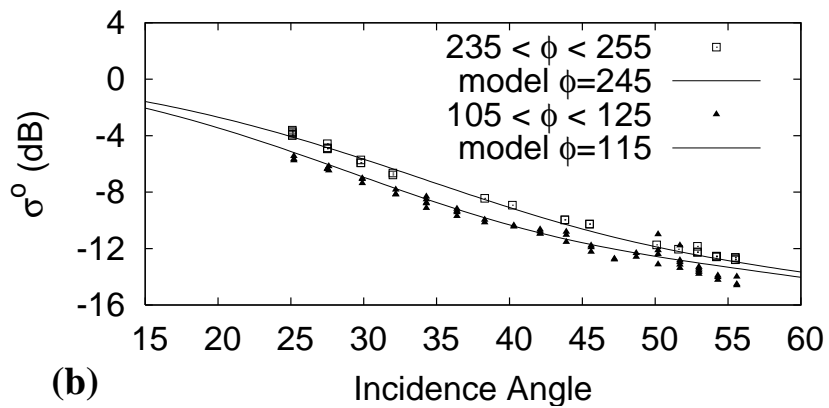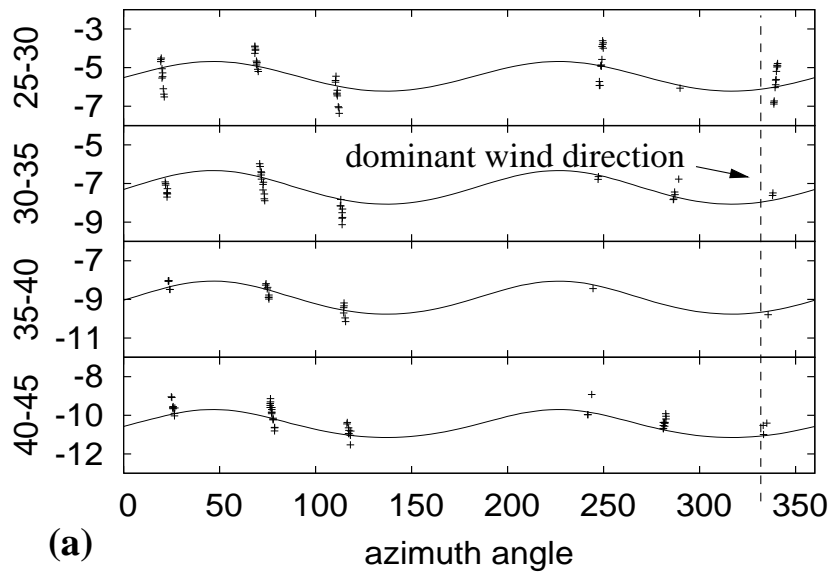
Figure 3.6: Same as Fig. 3.5 for the NASA-U site (73.83 N, 49.5 W).

Table 3.1: Maximum (ξ_1) and minimum (ξ_2) one-dimensional RMS meso-scale surface slopes in (m/m) and corresponding azimuth angles (in degrees relative to North) obtained from the A-model surface slope distribution estimates at the two study locations. Because the model makes no distinction between up and down wind, there is a 180° ambiguity in the direction of $\vec{u}_2$. The displayed value is the ambiguity closest to the measured wind flow direction. Also included in the table is an estimate of the meso-scale RMS surface slope for the I-model.

| | A-model | | | | I-model |
	ξ_1	ξ_2	$\angle\vec{u}_1$	$\angle\vec{u}_2$	ξ
Tunu-N	0.29	0.12	193°	103°	0.055
NASA-U	0.21	0.11	46°	316°	0.050

study locations with RMS residual errors of around 0.4 dB. The RMS errors are significantly larger for the other two models: 1.05 dB at Tunu-N and 0.65 dB at NASA-U. ERS measurement accuracy is approximately 0.2 dB [40].

The A-model enables estimation of the directional dependence of the meso-scale surface slopes. The correlation matrix of the meso-scale surface slope distribution indicates how the one-dimensional RMS surface slope varies with azimuth angle as discussed in Section 3.2.1. Recall that ξ_1 and ξ_2 are estimates of the maximum and minimum one-dimensional RMS surface slope, and the corresponding azimuth angles are given by the orientations of $\vec{u}_1$ and $\vec{u}_2$. Estimates of these values for the two study locations are listed in Table 3.1. The RMS surface slope in the dominant roughness direction (ξ_1) is largest at Tunu-N, indicating steeper meso-scale surface slopes at this location. This is attributed to the difference in accumulation rates rather than a difference in wind speed since the speeds shown in Figs. 3.5 and 3.6 exhibit no significant difference in magnitude at the two locations. At Tunu-N the accumulation rate is less than one half the accumulation rate at the NASA-U site [41, 42]. The accumulation rate contributes to the differences in the thickness of the annual layers, the snow density and other properties. Unfortunately, *in situ* data is not available to validate the observed RMS surface slopes.

Table 3.2: Small-scale parameters for the three surface scattering models at the two study locations where $V = n\sigma_b/2\alpha$. Each parameter is discussed in detail in Section 3.2.2.

	A-model			I-model			F-model		
	$k\sigma$	kl	V (dB)	$k\sigma$	kl	V (dB)	$k\sigma$	kl	V (dB)
Tunu-N	1.24	3.62	-8.8	1.17	2.87	-8.7	1.18	2.82	-8.7
NASA-U	1.35	3.15	-11.2	1.39	2.76	-11.2	1.40	2.72	-11.2

The plots at the bottom of Figs. 3.5 and 3.6 show the distribution of wind speed and direction during 1996 at the two locations. The model estimates show that the minimum of the azimuth modulation is in the $\vec{u}_2$ direction. As discussed in Section 3.2.1 the orientation of $\vec{u}_2$ corresponds with the up/down wind direction. This relationship between the dominant wind direction and the minimum of the azimuth modulation is consistent with the results of Long and Drinkwater [24] over Antarctica. At both locations the orientation of $\vec{u}_2$ is within 15° of the dominant wind direction as shown in Figs. 3.5 and 3.6.

The small-scale parameter estimates are listed for each of the three models in Table 3.2. Because the estimates of $k\sigma$ are outside of the valid range for SPM as discussed in Section 3.2.2 the parameters are representative of the relative rather than the actual surface roughness. The model estimates are still valuable in gaining insights into the scattering at these locations. Inspection of the two terms in Eq. (3.10) reveals important differences in the contribution of each small-scale parameter to the overall backscatter.

The combination of surface and volume scattering dictates the backscatter model dependence on incidence angle. In general, surface scattering generates a steeper incidence angle dependence at large incidence angles than does volume scattering. The large estimates of $k\sigma$ cause the surface scattering term to contribute more at large incidence angles resulting in a steeper incidence angle dependence than is provided by the volume scattering term only. Thus, to adequately model the surface in terms of snow properties either a more complex volume scattering term having

a steeper roll-off with incidence angle or a surface scattering term valid for larger estimates of the backscatter at high incidence angles is required. An alternate approach for future studies is a multi-layer model combining the surface and volume scattering from the individual layers. However, such a model will increase the number of unknown parameters, decreasing the probability for well-conditioned model inversion.

3.2.5   Ice-sheet wide surface parameter estimation

Meso-scale parameters

I have inverted the three variations of the surface scattering model to obtain parameter estimates across the ice sheet. Estimates of the meso-scale slope distribution parameters are shown in Fig. 3.7. Recall that ξ_1 and ξ_2 are the square-roots of the singular values of the correlation matrix R from the A-model and provide estimates of the maximum and minimum one-dimensional RMS surface slopes. Perhaps the most compelling indicator of the validity of the A-model and the assumption that wind-formed sastrugi are the dominant mechanism driving azimuth modulation over Greenland is found in the orientation of $\vec{u}_2$. As discussed previously, over a field of sastrugi $\vec{u}_2$ is oriented in the up/down wind direction. Figure 3.7 (c) shows streamlines of $\angle \vec{u}_2$ imposed over an image of ξ_1. The streamlines are very similar to the katabatic surface wind fields modeled by Bromwich et al. [33] over the Greenland ice sheet (see Fig. 3.8). One of the most identifiable features in both the $\angle \vec{u}_2$ streamlines and the Bromwich wind field is the wind divergence region running from the summit northwest to Hayes Peninsula (see Fig. 3.1). Over the southern portion of the ice sheet, the dominant wind direction also matches $\angle \vec{u}_2$.

Features of the wind pattern are evident throughout the dry snow zone in the ξ_1 image. Locations with divergent wind fields give small estimates of the sastrugi slopes, which is consistent with the low wind speeds and correspondingly small sastrugi found there. This is most apparent where the wind field diverges northwest of the summit. It is also observed on the east of Greenland between the Scoresby Sund and Kangerlussuaq Fjords (see Fig. 3.1 (a)) where Bromwich et al. [33] estimate corresponding low wind speeds. Along the ridge separating these two fjords,
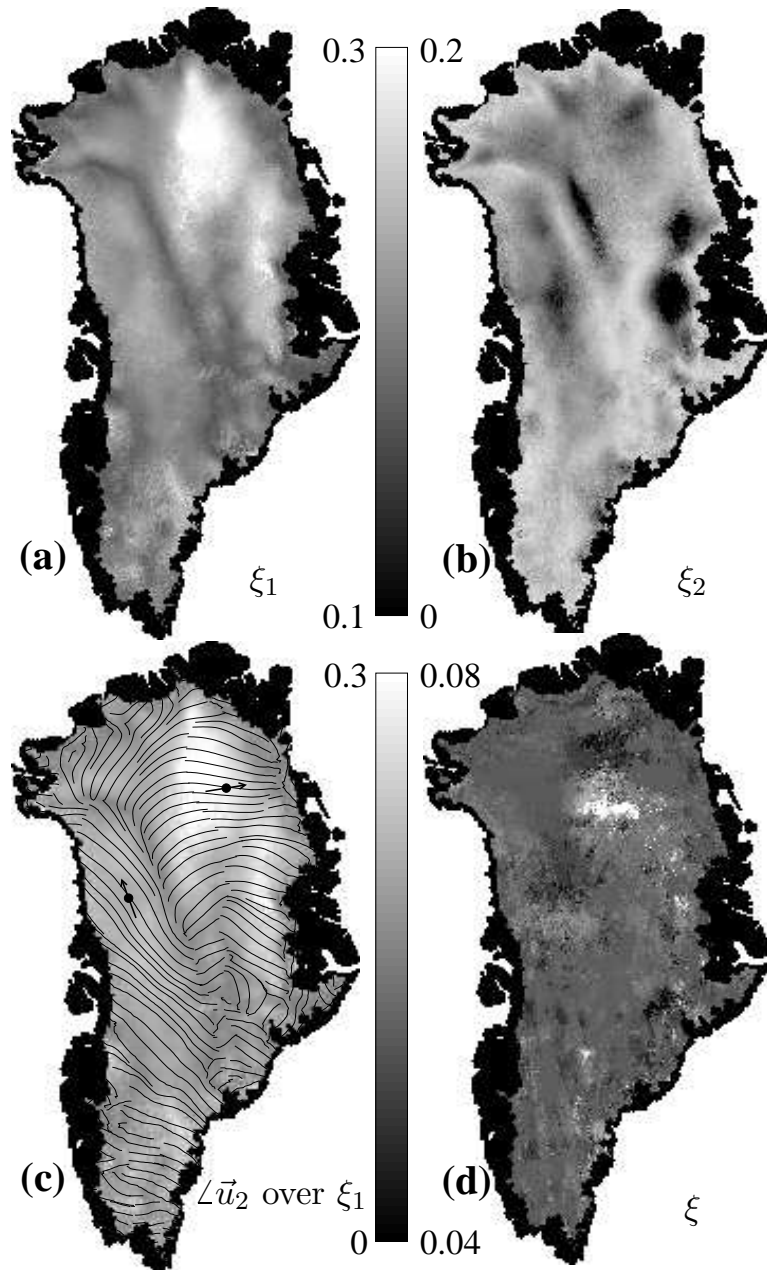
Figure 3.7: Images showing estimates of the meso-scale slope distribution correlation matrix singular values. (a) & (b) Maximum (ξ_1) and minimum (ξ_2) one-dimensional RMS surface slopes estimated using the A-model. (c) Stream-lines of the A-model estimate of the wind flow ($\vec{u}_2$ direction) imposed over a ξ_1 image. Direction is not indicated due to the 180° ambiguity in the model. Arrows indicate AWS measured average wind flow direction during 1996. (d) RMS surface slope obtained using the I-model.
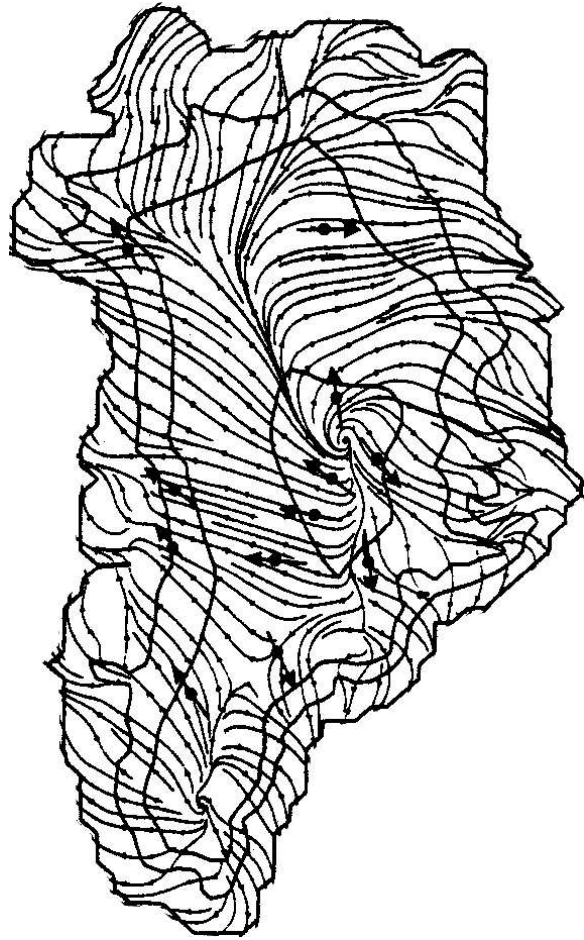
Figure 3.8: Estimate of the Greenland wintertime katabatic windfield estimate from Bromwich et al. [33].

the mean wind field diverges. Thus low winds are expected on the ridge and high winds on the slopes leading down to the fjords. This is observed in the ξ_1 image as a dark region (the ridge) between two brighter regions. Another pronounced feature in the ξ_1 image is an area of low estimates reaching almost directly north of the summit to the edge of the ice sheet between King Fredrik VIII Land and King Christian X Land. The location of these low estimates corresponds to the windward side of a ridge running northwest from the summit observed in Fig. 3.1 (b). For katabatic winds, such as those modeled by Bromwich et al. [33], the wind flow is driven by gravity and local topography. Katabatic cooling increases the air density so that it sinks downslope. In the region north of the summit with low RMS surface slope estimates, the wind and the topographical slope are nearly orthogonal. Because gravity is not accelerating the wind in the dominant flow direction, lower wind speeds are expected, which is consistent with the low ξ_1 estimates. One possible contributor to the differences in the ξ_1 estimates in the east and west dry snow zone is the difference in the accumulation rates. The northeast dry snow zone has about half the accumulation rate of the west dry snow zone [41, 42].

The low estimates of ξ_1 in the percolation zone are attributed to changes in the snow-pack associated with melt. Recall that the percolation zone is the region where melt occurs, but the snow pack does not become saturated with liquid water. Melt significantly changes the backscatter properties of the surface such that after refreeze the backscatter is dominated by scattering from subsurface ice structures [43] altering or masking the azimuth modulation signature. During the winter, scattering from the dry snow surface layer that has accumulated since the last melt is mitigated by its transparency and the strong backscatter from the sub-surface percolation facies.

Wind-field related features observed in the ξ_1 image are also apparent in the ξ_2 image. The estimates of ξ_2 at the divergent wind region between the summit and Hayes Peninsula are high while just outside the divergent region the estimates drop significantly. Low estimates are also found in other areas, mostly in the lower portions of the dry snow zone. These are areas where significant acceleration and narrow cross-wind variance is expected in the wind field as it nears the edge of the

ice sheet where the surface slope increases. The ice sheet slope is particularly large in King Christian X Land where the lowest estimates of ξ_2 are found.

Small-scale parameters

The images in Fig. 3.9 show the model parameters for the local incidence angle dependence. The small-scale parameters are estimated using a least-squares approximation for the three models. As discussed previously, the $k\sigma$ estimates are slightly outside the valid range for SPM. Thus $k\sigma$ and kl are indicative of relative rather than actual roughness. Nevertheless, as previously indicated, insights can be gained through viewing the small-scale model as an empirical model describing the local incidence angle dependence of σ°.

The $k\sigma$ and V terms primarily affect the magnitude of the σ° estimates, whereas the kl term is a major contributor to the incidence angle dependence of the σ° estimates. The $k\sigma$ estimates are nearly identical for all three models as are the V estimates. The $k\sigma$ and V images also exhibit very similar features. Three regions are observed in each image: a dark region at the interior surrounded by a bright region and then a reduced intensity region on the periphery. These regions roughly correspond to the dry snow, percolation, and wet snow facies. In general, the magnitudes of $k\sigma$ and V are correlated with the magnitude of the backscatter observed from the different facies. One feature observed only in the V image is the division of the dry snow zone into the two distinct regions first noted by Long and Drinkwater [6] in their investigations of the variance in σ° across the ice sheet.

Correlation length (kl) estimates are lowest in the percolation zone and highest in the dry snow zone. The I-model and F-model result in approximately the same kl estimates. The A-model is similar to the other two models in the percolation zone but produces significantly higher estimates of kl in the dry snow zone which has the largest azimuth modulation. Higher estimates of kl indicate an increased roll-off of σ° with incidence angle. In this region the A-model indicates an increased dependence of σ° on incidence angle.
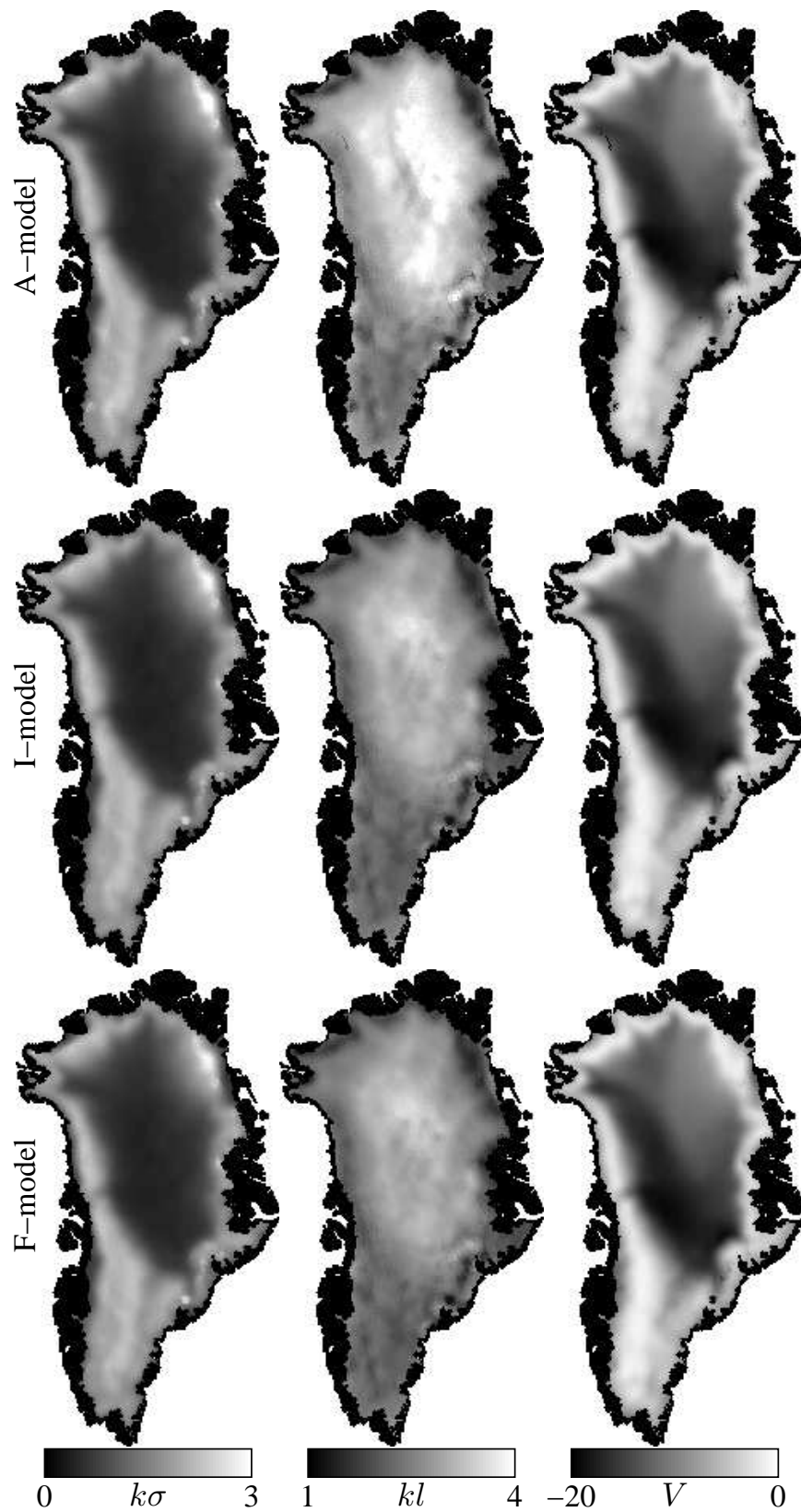
Figure 3.9:   Images of the estimated small-scale surface model parameters across the ice-sheet estimated for the three models from ERS σ° measurements.
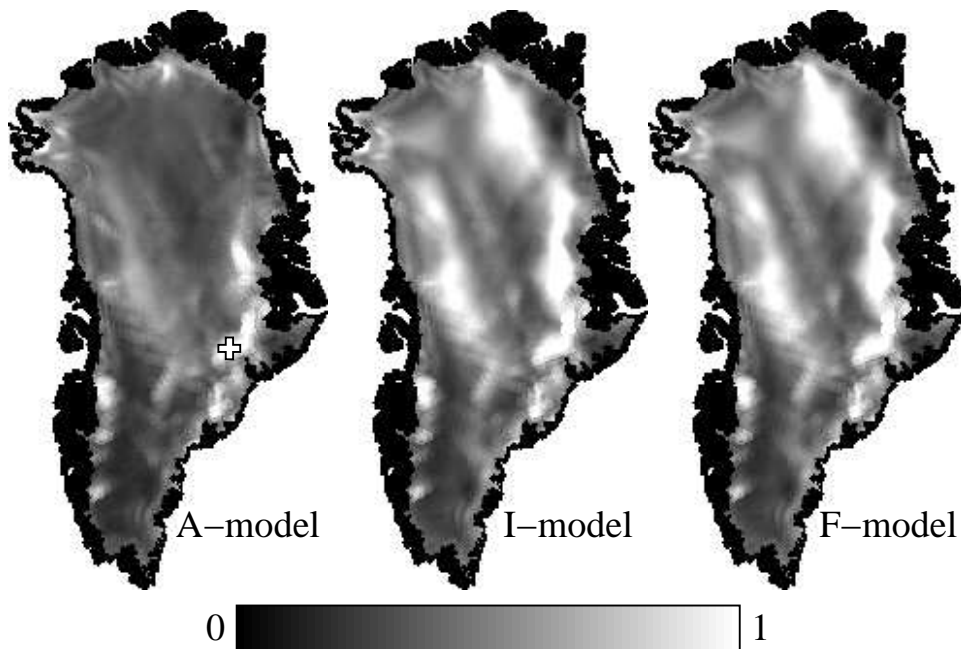
Figure 3.10: Images of the RMS error of the different models across the ice-sheet. The A-model image includes a "+" mark indicating the location (69.5 N, 34.3 W) which is used for further analysis of the RMS error.

Error analysis

Figure 3.10 shows the RMS error across the ice sheet for the three models as defined by Eq. (3.11). The A-model error is significantly smaller than that of the other two models throughout most of the dry snow zone, particularly in the northeast. The distribution of the RMS error for each model across the ice sheet is shown in Fig. 3.11. The A-model mean RMS error is 0.46, significantly less than the 0.56 dB mean RMS error of the I-model and F-model. Over a significant portion of the ice sheet the A-model RMS error approaches the ERS accuracy of 0.2 dB [40].

Areas with above average RMS errors are observed between King Christian IX Land and King Christian X Land along the east edge of the dry snow zone. A close inspection of the $\sigma°$ measurements in these large error regions reveals anomalies in the data at varying azimuth and incidence angles. Figure 3.12 shows data from 69.5 N, 34.3 W (see Fig. 3.10), a location within this high error region. From Fig. 3.12

46
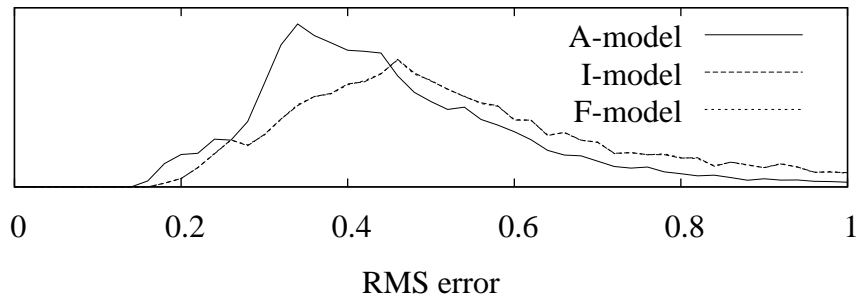
Figure 3.11: Normalized histogram of the RMS error across the ice sheet for the different models. The I-model and F-model overlap making them almost indistinguishable.

(a) we observe that the largest errors occur around $\phi = 75°$. In Fig. 3.12 (b) it appears that the incidence angle dependence around $\phi = 75°$ is reversed from the common incidence angle dependence observed over Greenland. At this location and azimuth angle, $\sigma°$ increases with incidence angle opposed to the decrease of $\sigma°$ with incidence angle commonly observed over Greenland. Similar anomalies in the ERS measurements are observed throughout the regions with high RMS errors. Between King Christian IX Land and King Christian X Land the anomalies are generally restricted to the range $-60 < \phi < 100$, though the anomalies are not always a reversal in the incidence angle dependence as observed in Fig. 3.12. In general the anomalies occur as abnormally high or low $\sigma°$ measurements within a small azimuth and incidence angle range. The source of these anomalies is not understood. A more complete azimuth and incidence angle sampling of $\sigma°$ combined with *in situ* data may be needed to understand the phenomena driving these anomalies. Because the specific azimuth and incidence angles where such anomalies are observed varies with location, it does not appear to be an instrument effect.

3.3   Summary

Significant azimuth modulation occurs in the ERS $\sigma°$ measurements of Greenland. This modulation is beneficial for further understanding the properties of
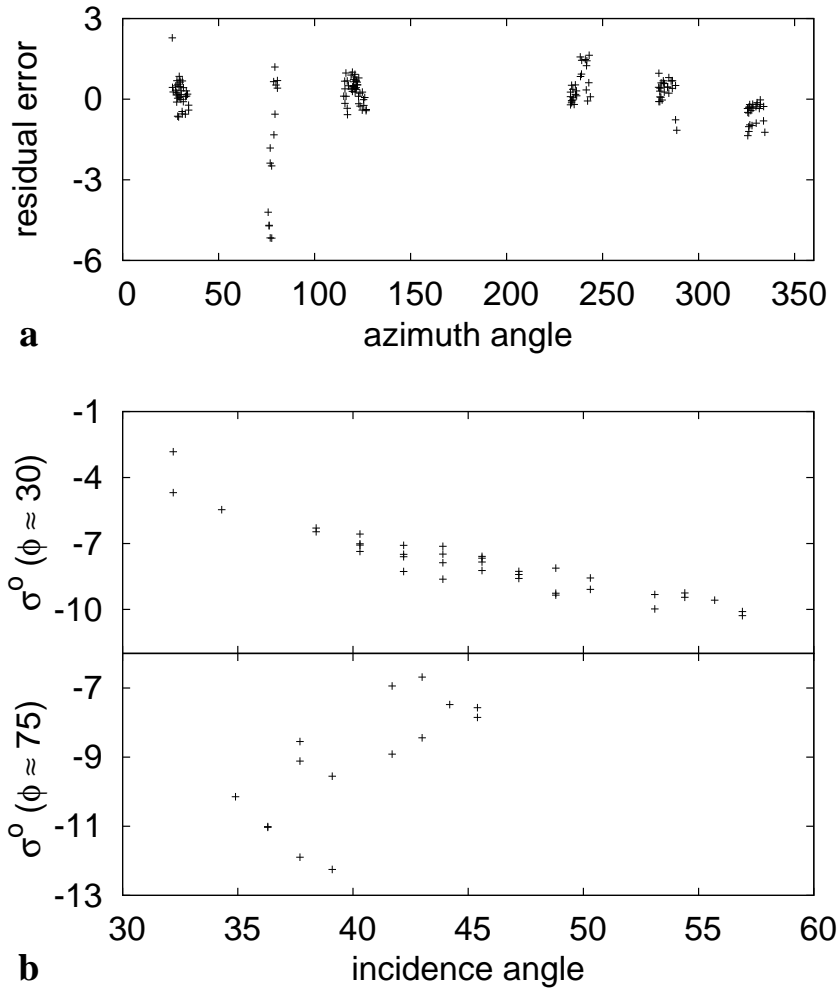
Figure 3.12: ERS data and A-model estimate errors at 69.5 N, 34.3 W (see Fig. 3.10). (a) A-model estimation error versus azimuth angle. At azimuth angles near 75° there is a high concentration of above average estimation errors. (b) Incidence angle dependence of raw σ° measurements at two azimuth angles. At $\phi \approx 30^\circ$ (top) the measurements exhibit the expected falloff with incidence angle. However, at $\phi \approx 75^\circ$ the measurements exhibit a counter-intuitive increase with incidence angle.

the ice sheet, with particular application to wind flow. A simple two-scale model can be used to model the combined incidence and azimuth angle dependence of the data. This model assumes that the primary mechanism driving the azimuth modulation are anisotropies in the meso-scale surface roughness, The small-scale incidence angle dependence is modeled using a combination of surface and volume scattering. Because the resulting surface roughness estimates are slightly outside the accepted range for the surface scattering model, the small-scale model must be viewed as an empirical model. Future studies may implement the model using SSA which has a larger region of validity than SPM. However, SSA adds significantly to the complexity of the model.

Model estimates are consistent with the idea of wind-formed sastrugi playing a dominant roll in the azimuth modulation. Estimates of the direction with the minimum one-dimensional RMS slope are highly correlated with katabatic wind flow patterns and AWS measurements. Many features related to the wind flow are observed in the model estimates of the surface slope characteristics. The largest meso-scale slope estimates occur in the lower portions of the dry snow zone. Even in the percolation zone where azimuth modulation is small and scattering from subsurface ice structures is significant, model estimates of the surface roughness directionality are strongly correlated with katabatic wind patterns.

The A-model, which assumes anisotropic meso-scale surface roughness, results in significantly smaller modeling errors than the I-model (isotropic meso-scale roughness) or the F-model (flat meso-scale surface). The mean RMS error is 0.46 dB for the A-model compared to 0.56 dB for the isotropic roughness models. Over much of the dry snow zone where significant azimuth modulation is observed, the improvement given by the A-model is much larger.

The A-model is a promising tool for characterization of the Greenland surface. Using σ° azimuth modulation, the dynamics of the Greenland ice sheet may be better tracked, including long term wind patterns. A better understanding of the azimuth modulation over Greenland in connection with geophysical surface properties may be obtained through *in situ* studies which combine measurements of σ° azimuth modulation with measurements of the geophysical properties of the surface.

Chapter 4

Microwave Signature Descriptive Model

Each scatterometer $\sigma°$ measurement has a given set of observation parameters including location (typically the measurement centroid) and look geometry (incidence and azimuth angle). Combined, these parameters are termed the observation geometry. A perturbation of any of the observation geometry parameters results in a corresponding change in the observed $\sigma°$. How $\sigma°$ changes with the observation geometry is termed the microwave signature of the snow. Temporal trends in the variation of $\sigma°$ are also part of the microwave signature. The regular and complete coverage of the ice sheet by scatterometers with measurements of $\sigma°$ at multiple incidence and azimuth angles enables the estimation of the $\sigma°$ signature of the surface. Our objective is to use scatterometer measurements of $\sigma°$ to estimate this signature using a small number of model parameters. This simplified model aids in the observation of $\sigma°$ and the study of its relationship to the large-scale geophysical properties of the snow.

The $\sigma°$ signature of the surface is important in at least three ways. First, the parameters characterizing the signature provide a reference frame for monitoring and understanding changes occurring on the surface relating to global climate change and other phenomenon. Changes in the snow surface are observed by a scatterometer as changes in the microwave signature. By closely monitoring the microwave signature and how it varies over time, the temporal variability of the physical properties of the ice sheet can be estimated. Second, an accurate descriptive model of the microwave signature enables the inference of variations from the average microwave signature on relatively short time scales. Using the model, individual measurements can be

normalized to a given geometry and then compared, making it possible to observe changes at the temporal sampling rate of the sensor while mitigating the $\sigma°$ changes due to variations in the observation geometry. Third, the $\sigma°$ signature is valuable for accurate studies of data sets with limited sampling over the observation geometry. A primary example is the azimuth sampling for SAR, which is effectively a single azimuth instrument. High resolution maps of temporal change may be obtained by inter-comparing swaths from different time periods. If these passes occur at different azimuth angles, the unaccounted for differences in $\sigma°$ due to azimuth modulation may be misinterpreted as being caused by temporal change of the surface. Additionally, processing of wide-angle SAR may be refined by including prior estimates of the azimuth dependence of $\sigma°$ along the swath.

In this chapter, a new model for parameterization of the $\sigma°$ signature over ice sheets is presented. The model is discussed in detail, outlining the theory as well as the relative importance of each individual element. I show the variation of each model parameter across the ice sheet and discuss the physical interpretation. Two applications of the model are considered: monitoring inter-annual changes across the Greenland ice sheet by observing the changes in the model parameters over time, and monitoring intra-annual change by observing the variation in $\sigma°$ measurements when normalized to a specific observation geometry using the long term average $\sigma°$ signature. Finally, a brief summary of the model and its applications is provided.

4.1   Background

This study employs data from ERS (C-band) and NSCAT (Ku-band). Both instruments have a fan beam design with ERS being a single swath instrument and NSCAT having a dual swath. The fan-beam design provides measurements at a range of incidence angles spanning 20 to 60 degrees from nadir. ERS has three fixed antennas, each measuring vertical polarization $\sigma°$ at a different azimuth angle. Combining ascending and descending passes provides azimuth sampling at approximately 6 distinct azimuth angles. NSCAT measures vertical polarization $\sigma°$ using 6 antennas providing azimuth sampling at more angles. Plots of the incidence/azimuth
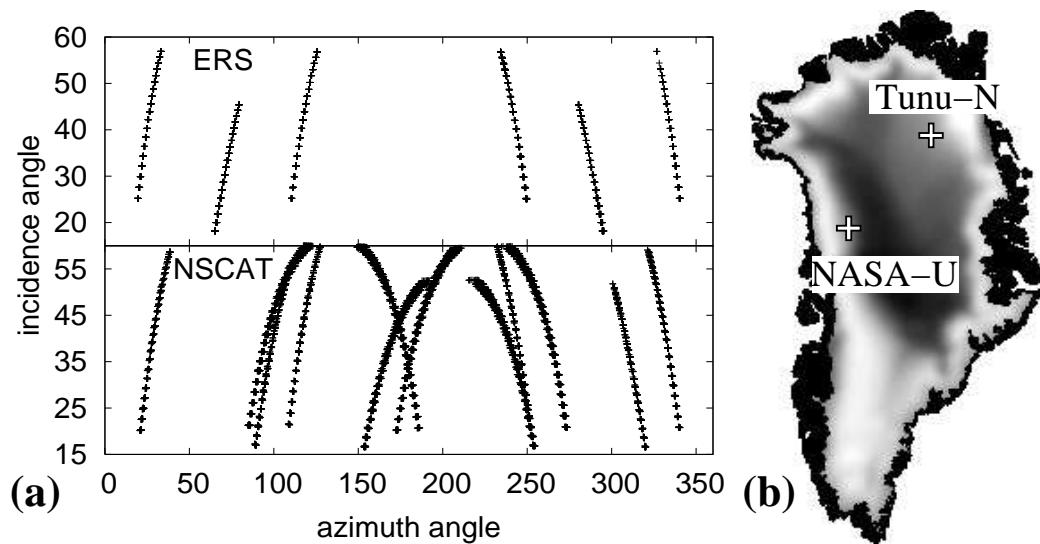
Figure 4.1: (a) Scatter-plot of azimuth angle versus incidence angle for ERS and NSCAT at NASA-U during the 6 months centered around January 1, 1997. (b) The locations of the Tunu-N and NASA-U stations indicated on an ERS image of A (σ° normalized to 40° incidence angle).

angle sampling for ERS and NSCAT are shown in Fig. 4.1 (a). ERS measurements at all six azimuth angles only occur within the incidence angle range of 25 to 45 degrees. Because of this, only data within the 25-45 degree incidence angle range is included in this study. The same incidence angle range is used for NSCAT to make the study self consistent. This study primarily uses data from the 6 month interval from Julian Day (JD) 275, 1996 to JD 90, 1997 which is during the winter months when backscatter from the Greenland surface is relatively constant.

Two locations are used for in-depth analysis throughout this study. These are the Tunu-N (78.0 N, 34.0 W) and NASA-U (73.83 N, 49.5 W) sites. The locations are shown in Fig. 4.1 (b). For each site Automatic Weather Station (AWS) data is available through the Greenland Climate Network [39]. The raw data analyzed at each location comprises all σ° measurements with centroids which lie within a 25 km radius of the location center.

In addition to focusing on the microwave signature at these two locations, I also present images of the model parameters across the ice sheet. The $\sigma°$ model parameter values for each grid element are estimated using a least-squares fit to the model as described in Section 2.4. The ice sheet mask is the same as that used by Abdalati and Steffen [2] which originated from the Quaternary Map of Greenland produced by the Geological Survey of Greenland.

4.2   Observation Model

In order to parameterize the $\sigma°$ signature of the Greenland surface I introduce an empirical observation model for $\sigma°$,

$$\sigma° = A + f(\theta - \theta_{\mathrm{ref}}) + q(\phi) + h(\mathbf{r}) + p(t - t_0) \tag{4.1}$$

where the variables describing the observation geometry are

θ – measurement incidence angle,

$\theta_{\mathbf{ref}}$ – reference incidence angle,

ϕ – measurement azimuth angle,

$\mathbf{r}$ – spatial displacement vector,

t – measurement time, and

t_0 – reference time,

and $\sigma°$ is in dB. The functions $f(\theta - \theta_{\mathrm{ref}})$, $q(\phi)$, $h(\mathbf{r})$, and $p(t - t_0)$ give the microwave signature relative to the argument parameters. Each is discussed in detail in the following sections. A represents the average at the incidence angle θ_{ref} and time t_0. For this application, θ_{ref} is set to $40°$ and t_0 is set to the center time of the data set.

The primary metric used to evaluate the performance of different model formulations is the RMS modeling error

$$\chi = \left(\frac{1}{N} \sum_{i=1}^{N} (\sigma_i° - \hat{\sigma}_i°)^2 \right)^{(1/2)} \tag{4.2}$$

where $\sigma_i°$ is the ith measurement in dB and $\hat{\sigma}_i°$ is the corresponding estimate given by Eq. (4.1). To evaluate the model performance across the entire ice sheet I use the

average RMS modeling error

$$\bar{\chi} = \frac{1}{M} \sum_{i=1}^{M} \chi_i$$

where M is the number of imaging pixels within the ice sheet. Using the fully developed model $\bar{\chi} = 0.375$ dB for ERS and $\bar{\chi} = 0.458$ dB for NSCAT.

4.2.1   Average backscatter

I first discuss A which represents the average backscatter normalized to θ_{ref} and t_0. A key application of A is in delineating the Greenland ice facies [6, 7, 8, 9, 43]. Images showing the variation in A across the ice sheet for both ERS and NSCAT are shown in Fig. 4.2. The extent of each of the snow facies can be estimated from the images in Fig. 4.2. The dry snow is characterized by low A values throughout the center of Greenland [6, 7]. Because the snow grains of dry snow are relatively small, the microwaves penetrate deep in the snow and are absorbed, producing little backscatter.

There is a strong spatial gradient in the backscatter between the dry snow zone and the central percolation zone. At the upper edge of the percolation zone the summer melt is short and the difference in backscatter from the dry snow zone is relatively small. The short melt results in a crust of *iced firn*[1] on the surface and an increase in snow-grain size due to sublimation [30]. An increase in grain size produces a corresponding increase in A in frozen snow [6]. Further downslope in the percolation zone the summer melt contributes to the formation of subsurface ice structures termed ice pipes and ice lenses which form when percolation channels in the wet snow freeze [6]. Surface scattering from the rough tops of the ice lenses and re-frozen melt surface causes the bright return in the lower portions of the percolation zone [7, 43].

Downslope from the percolation zone on the edge of the ice sheet is a narrow region of intermediate A values indicating the wet snow zone [7]. The delineation between the percolation zone and the wet snow zone is perhaps the most difficult to

---

[1]Iced firn is formed when water-saturated snow freezes.
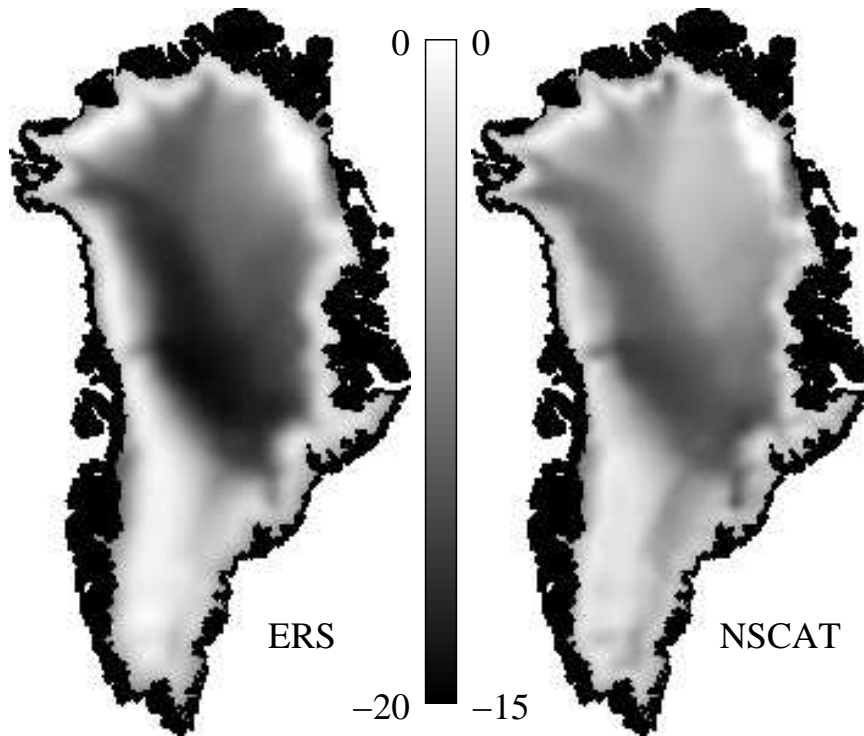
Figure 4.2: Images of A from NSCAT (Ku-band) and ERS (C-band) estimated using 6 months of data centered at January 1, 1997. The area outside the ice sheet is black in the images.

infer using the A images alone because of the low contrast between the two regions. Other parameters perform better for this purpose.

Differences between the ERS and NSCAT A images are also beneficial in delineating the snow facies. Drinkwater et al. [18] use this difference to determine the line separating the dry snow and percolation zones. The ERS/NSCAT difference is attributed to the frequency difference between the two instruments. For NSCAT, the size of the snow grains relative to the wavelength is larger than for ERS, which increases the radar cross-section of the individual snow grains. The larger σ° values for NSCAT in the dry snow zone are attributed to this effect. In the percolation zone, NSCAT σ° values are smaller than ERS. This is attributed to the reduced penetration depth due to the higher frequency of NSCAT which results in reduced scattering from the subsurface ice structures.

4.2.2 Incidence angle dependence

In my model, σ° varies as a quadratic function of incidence angle where σ° is in dB and θ is in degrees, i.e.

$$f(\tilde{\theta}) = B_1\tilde{\theta} + B_2\tilde{\theta}^2 \qquad (4.3)$$

where $\tilde{\theta} = \theta - \theta_{\text{ref}}$. Any constant offset is subsumed into A.

The B_1 images in Fig. 4.3 show the variation in the linear incidence angle dependence of σ°. In general, B_1 is an indicator of the contribution of volume scattering versus surface scattering. An increase in the magnitude of B_1 indicates a greater contribution from surface scattering. Based on this premise, some general conclusions are attained from the B_1 images.

For ERS, $|B_1| \approx 0.3$ dB/deg in the upper percolation zone which is nearly double that observed across the rest of the ice sheet, suggesting that in the upper percolation zone the relative contribution from surface scattering is much larger than elsewhere. This is attributed to the iced firn forming on the surface after a melt event [30] contributing to increased surface scattering. The key difference between the upper and lower percolation zone is that in the lower percolation zone the longer melt results in the formation of subsurface ice structures that contribute to the increased volume-like scattering. Similarly, for NSCAT the largest B_1 magnitude is observed in the dry snow zone indicating increased relative contribution from surface scattering in this area.

A key difference between the NSCAT and ERS estimates of B_1 is observed in the dry snow zone. The smaller magnitude of B_1 for NSCAT suggests that the relative contribution from volume scattering is much more significant in this region at Ku-band. This difference between C-band and Ku-band is attributed to volume scattering in the dry snow zone, primarily originating from the individual snow grains. The grains are electrically larger at Ku-band, corresponding to larger individual radar cross-sections. This is consistent with the larger A values observed for Ku-band in the dry snow zone. The ERS and NSCAT B_1 are similar in the lower percolation zone and wet snow zone where the volume-like scattering is attributed to subsurface
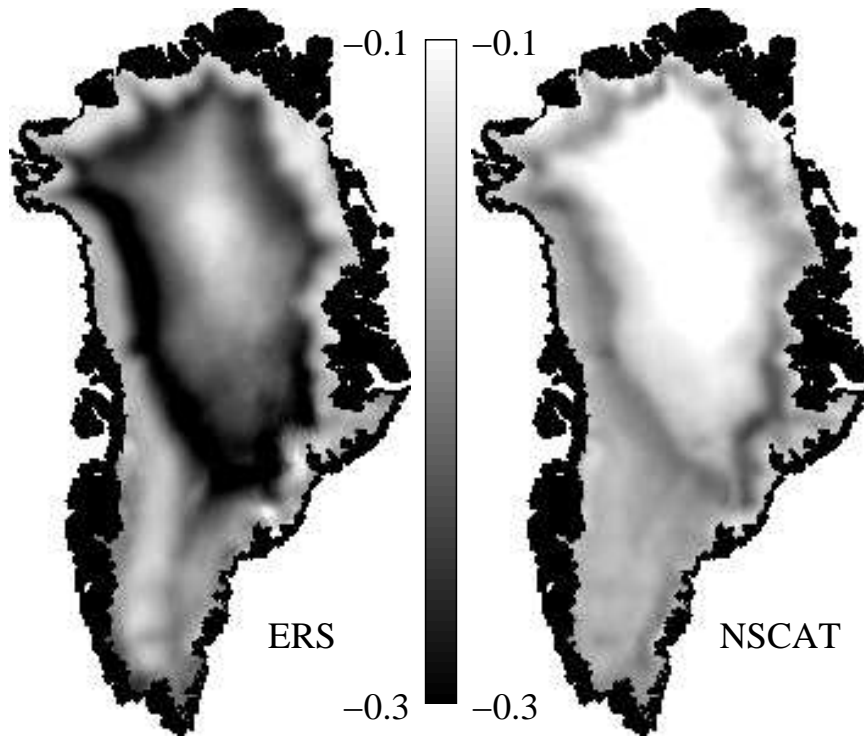
Figure 4.3: Images of B_1 from NSCAT and ERS estimated using 6 months of data centered at January 1, 1997.

ice structures that are electrically large at both C-band and Ku-band. Variations of B_1 within the dry snow zone are attributed to the variation in the accumulation rate where more negative B_1 values indicate regions of higher accumulation [18].

Figure 4.4 shows the variation of B_2 across the ice sheet. For my data set, which includes the incidence angle range from 25 to 45 degrees, B_2 is an indicator of the relative contribution of surface scattering at low incidence angles.

For ERS, the B_2 values are the most positive in the dry snow zone and upper percolation zone indicating that the relative contribution of surface scattering at low incidence angles is largest in these areas. For NSCAT, the most positive B_2 values are observed in the upper percolation zone. The large B_2 values in the upper percolation zone are attributed to the large relative contribution of surface scattering to the overall backscatter in this region. In the dry snow zone, the difference in B_2 between the two frequencies is attributed to surface scattering contributing relatively
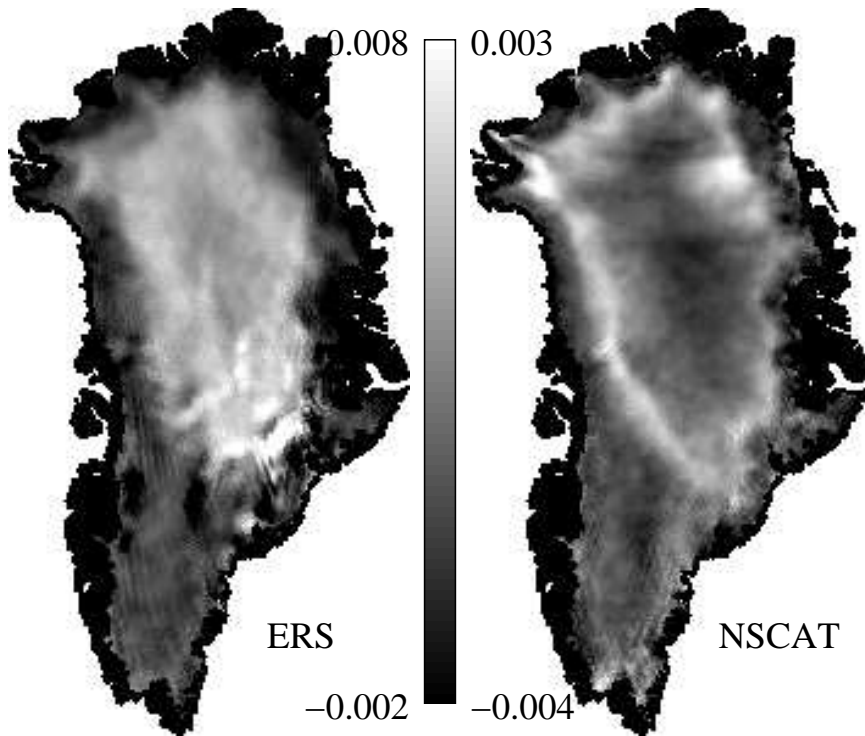
Figure 4.4: Images of B_2 (second order incidence angle dependence) from NSCAT and ERS estimated using 6 months of data centered at January 1, 1997.

more to the overall backscatter for ERS than for NSCAT. This reasoning is consistent with the observations from the B_1 images.

The modeling of incidence angle dependence is critical to the model. Without incidence angle dependence in the model, the average RMS modeling error is $\bar{\chi} = 1.26$ dB for ERS and $\bar{\chi} = 0.957$ dB for NSCAT. Including linear incidence angle dependence reduces the modeling error to $\bar{\chi} = 0.393$ dB for ERS and $\bar{\chi} = 0.461$ dB for NSCAT. When the second order term is included so the incidence angle dependence is quadratic, the modeling error is further reduced to $\bar{\chi} = 0.375$ dB for ERS and $\bar{\chi} = 0.458$ dB for NSCAT.

4.2.3 Azimuth angle dependence

The signature of σ° with azimuth angle provides valuable information relating to the surface profile. In the previous chapter a simple physical model is used

to relate azimuth dependence of σ° to aeolian-formed surface features such as sastrugi[2]. The physical model indicates that azimuth modulation of σ° over Greenland is related to katabatic wind flow. Using a physical model provides valuable insights into the relationship between surface features and backscatter; however, inversion of the model requires second-order iterative non-linear regression. To enable faster, more robust model inversion, in this chapter an empirical linear descriptive model is adopted which provides accuracy similar to the physical model. This empirical model facilitates the data normalization with respect to azimuth angle which is essential for accurate inter-measurement comparisons.

This empirical model for the variation of σ° with azimuth angle consists of the second order Fourier Series

$$q(\phi) = M_1 \cos(\phi - \phi_1) + M_2 \cos(2\phi - \phi_2) \tag{4.4}$$

where M_1 and M_2 are the magnitudes of the first and second order azimuth modulation respectively, and ϕ_1 and ϕ_2 are the orientations. This simple empirical model is chosen because it minimizes the model complexity and accurately exhibits the properties of the data. This model is also appropriate for the scale: it requires a minimal amount of knowledge of the geophysical properties of the surface which may vary widely across the scatterometer footprint and within the penetration depth of the radar. Additionally, this is a simple diagnostic model used to identify the sensitivity of σ° to azimuth variation.

This empirical azimuth dependence model is similar to models used previously for the azimuth signature of σ° over Antarctica, which has an environment similar to Greenland. The models previously proposed for the azimuth signature over Antarctica each include one or more terms of a Fourier Series. Ledroit et al. [22] use a bi-sinusoid based on a theoretical model of ocean backscatter to model azimuth dependence of Seasat-A scatterometer measurements over Antarctica finding azimuth dependencies as large as 5 dB at Ku-band. Similarly, Young et al. [23]

---

[2]Erosional or depositional wind formed surface features aligned such that the crest is parallel to the wind direction [34].

use a bi-sinusoid to model ERS variations over Antarctica finding azimuth modulations of similar magnitude (5.5 dB peak-to-peak maximum) for C-band. Long and Drinkwater [24] added a first order sinusoid for their analysis and linear variation in the magnitude of the modulation with incidence angle. The net finding of these studies is that azimuth modulation over Antarctica is primarily second order (180° symmetry), and its orientation is related to the prevalent surface wind direction.

Because the characteristics of $\sigma°$ azimuth dependence over Greenland have not previously been investigated in depth, I devote considerable effort to this topic. First, the azimuth dependency of the data relative to the azimuth variation in the model is investigated. Next, the relationship between azimuth dependence and wind flow is discussed, showing estimated wind flow maps based on the $\sigma°$ signature of the surface for both ERS and NSCAT. Subsequently, 9 years of ERS data are used for analysis of the long term variability in the azimuth signature of $\sigma°$. Finally, the variation in the azimuth signature with incidence angle is investigated and found to be relatively insignificant given the inherent variance of the data.

To illustrate the fit of the second-order Fourier Series to ERS and NSCAT data, I use measurements from the NASA-U and Tunu-N sites discussed in Section 4.1. The model fit to the data is shown in Fig. 4.5. The plots show the model estimate of the azimuth modulation, $q(\phi)$ (see Eq. 4.4), versus the raw data with the DC bias and all dependencies besides azimuth removed, i.e.

$$q_i = \sigma_i° - A - B(\theta_i - \theta_{\text{ref}}) - s_1(\mathbf{r}_i \cdot \mathbf{g}).$$

As observed in Fig. 4.5, a second-order fit is required to adequately describe the azimuth dependence.

Images of the model parameters related to azimuth dependence are shown in Fig. 4.6. The M_1 and M_2 images show estimates of the magnitude of the azimuth anisotropy of the $\sigma°$ measurements. Azimuth dependence is greater for ERS than for NSCAT. For both instruments, the dependence is primarily second-order, indicative of 180° symmetry in the microwave properties of the firn. Although smaller, the magnitude of the first order dependence is non-negligible. The azimuth dependence
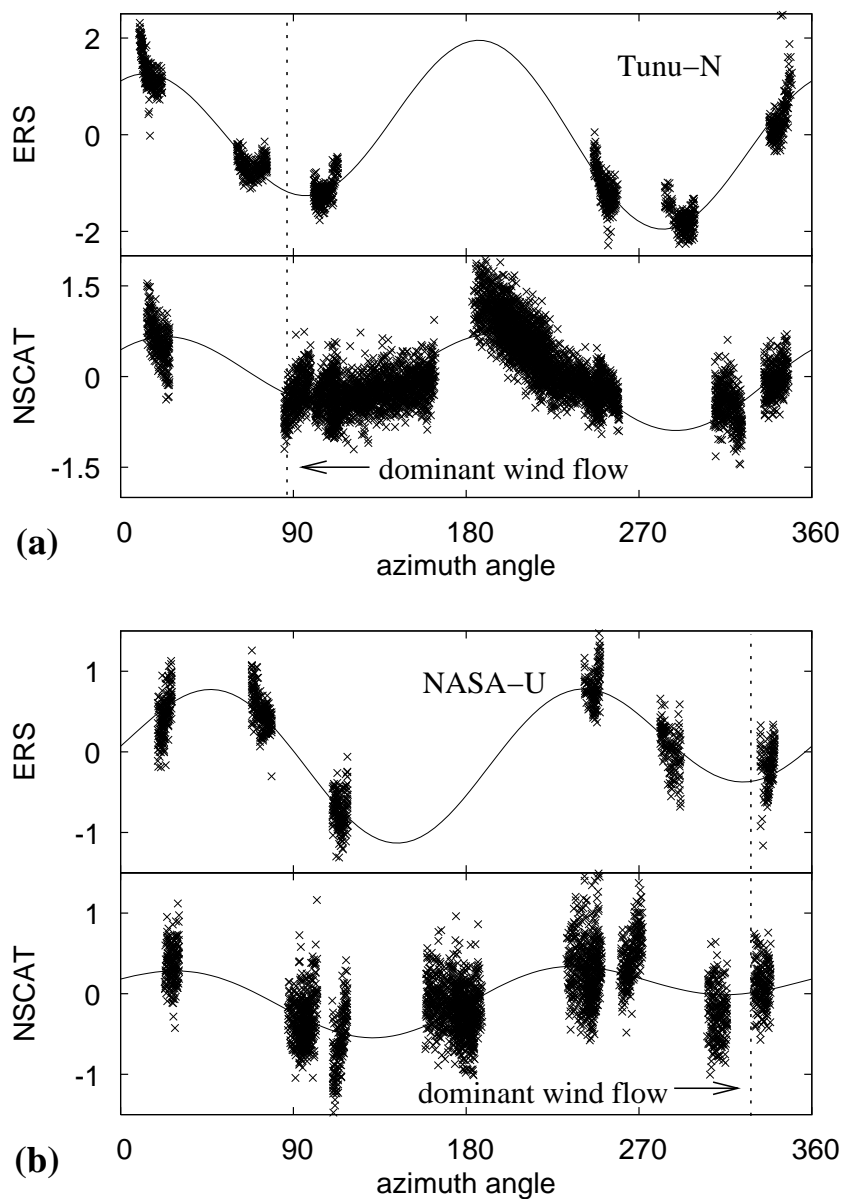
Figure 4.5: Azimuth dependency observed in the data and the model at (a) Tunu-N and (b) NASA-U. Normalized raw data measurements (q_i) are shown as "+" marks and the line indicates the model estimate $(q(\phi_i))$ of the azimuth dependence. The dominant wind direction during 1996 based on automatic weather station data from the Greenland Climate Network [39] is indicated by a vertical dotted line on each plot. The wind direction coincides with a local minimum of the azimuth modulation which supports the theoretical correlation between wind direction and azimuth modulation.

is largest in the lower portions of the dry snow zone and the transition region from the dry snow to percolation zone. The largest azimuth dependence is found in the northeast dry snow zone where the accumulation rate is relatively low [42]. Moving south from the northeast dry snow zone, a decrease in the magnitude of the azimuth dependence is observed. The location of this decrease corresponds to the windward side of a ridge northeast of the summit. The reduction in the azimuth modulation in this area is attributed to a decrease in the katabatic wind flow due to the wind flowing cross- or up-slope rather than down-slope [44]. There is a general decrease in the azimuth modulation moving from the dry snow zone to the percolation zone, especially with ERS. This is attributed to the scattering from subsurface ice structures which dominates the backscatter in this region [43] and is wind independent.

As discussed in the previous chapter and by Long and Drinkwater [24], wind-formed erosional snow features known as sastrugi are a dominant factor driving azimuth modulation. Sastrugi crests are parallel to the wind direction [34] resulting in local minima in the azimuth modulation in the up/down wind directions and a local maximum in the cross-wind directions. The observation model presented in this chapter gives results consistent with this theory. At NASA-U and Tunu-N the minimum of the ERS and NSCAT backscatter with azimuth angle matches the measured dominant wind direction as illustrated in Fig. 4.5.

Streamlines in the azimuth direction of the backscatter minimum for ERS and NSCAT are shown in Fig. 4.7. The streamlines are imposed over M_2 images from the corresponding sensor. The streamlines represent estimates of the wind flow and are highly correlated with modeled katabatic wind fields [33]. A strong feature in the streamline flow is the divergent region progressing northwest from the summit to the Hayes Peninsula. Differences observed between ERS and NSCAT wind estimates are attributed to Ku-band being sensitive to smaller roughness scales and also having smaller penetration depths than C-band.

The azimuth dependence is deemed an important part of the model based on its contribution to the overall model accuracy. Without modeling azimuth modulation, the model yields $\bar{\chi} = 0.591$ dB for ERS and $\bar{\chi} = 0.550$ dB for NSCAT.

0.8   0.5

M_1

0   0

ERS   NSCAT

1.5   0.8

M_2

0   0
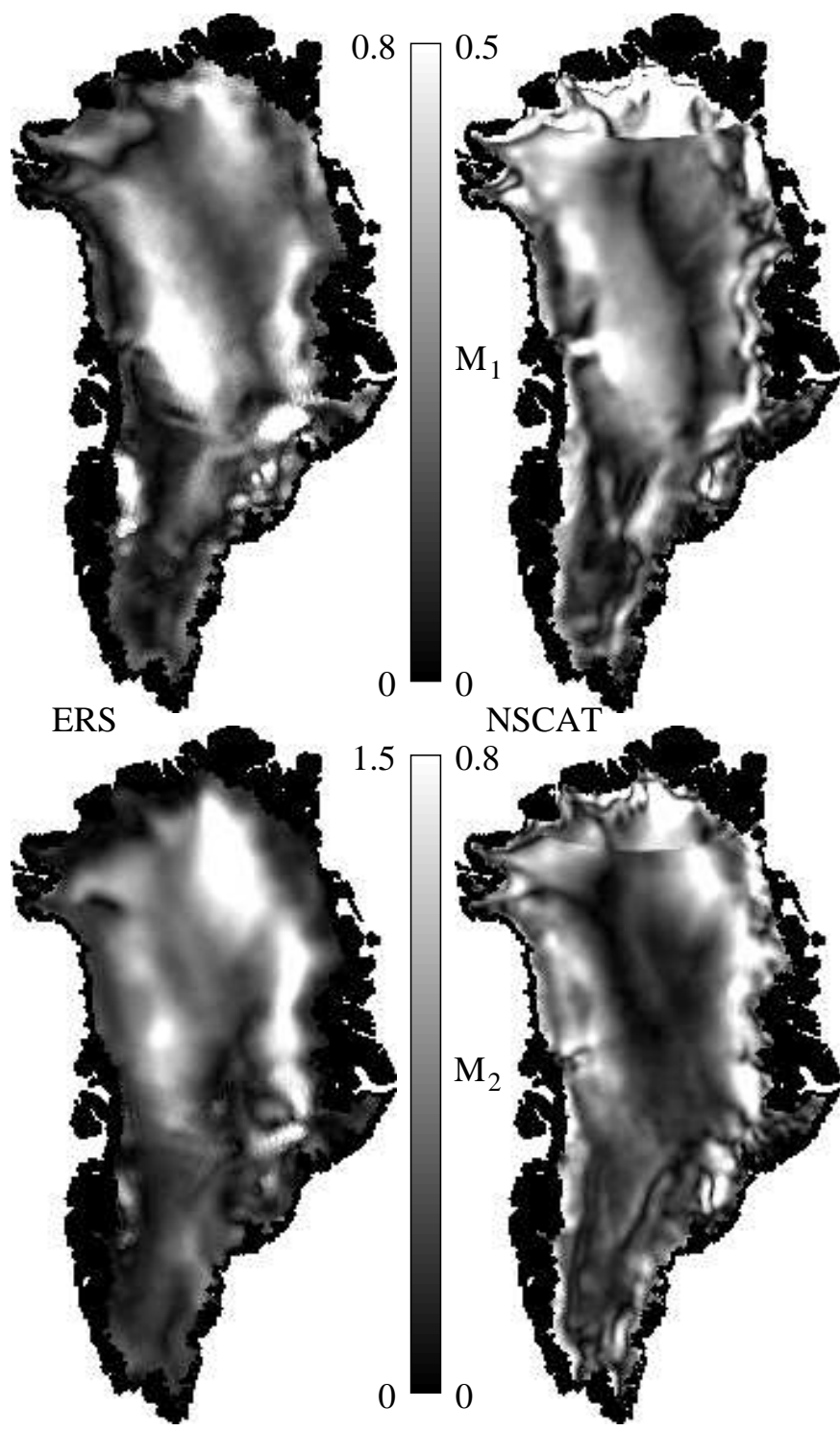
Figure 4.6: Images of the magnitude of the azimuth dependence parameters M_1 and M_2.
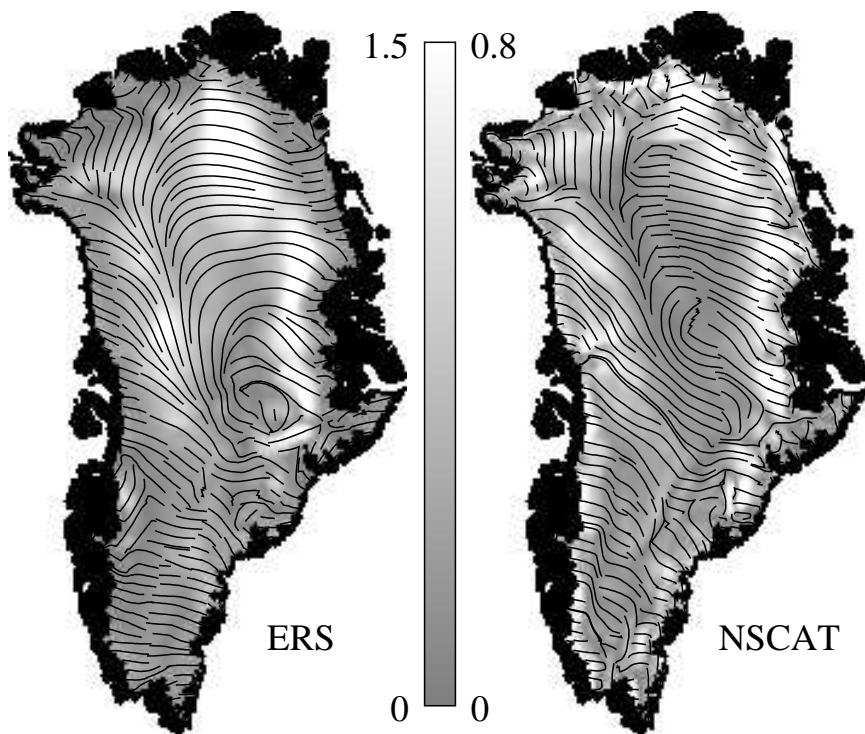
Figure 4.7: Streamlines of second order azimuth modulation minimums for ERS and NSCAT. The streamlines are imposed over M_2 images from the respective sensors.

Inclusion of only first order modulation reduces the error to $\bar{\chi} = 0.504$ dB for ERS and $\bar{\chi} = 0.511$ dB for NSCAT. Including only second order dependence results in smaller errors: $\bar{\chi} = 0.423$ dB for ERS and $\bar{\chi} = 0.491$ dB for NSCAT. When the model includes both first and second order dependence the average RMS modeling error is reduced to $\bar{\chi} = 0.375$ dB for ERS and $\bar{\chi} = 0.458$ dB for NSCAT.

Long-term stability of azimuth modulation

A question that arises in analyzing the azimuth dependence of σ° is how it varies with time. Over the ocean, the azimuth signature of σ° responds almost immediately to changes in wind direction and speed. Over Greenland a much slower change in azimuth dependence is expected because the changes in the surface profile with wind change are not as immediate as those over the ocean. Also, the backscatter is a composite of scattering from multiple layers which effectively makes the azimuth signature dependent upon the wind flow over an extended period of time. The length of time represented depends on the penetration depth, layer thickness and relative magnitude of the backscatter from the individual layers.

To investigate the rate of change of the azimuth signature I use parameter estimates from 9 years of ERS data with the parameters estimated at 15 day intervals using 30 days of data. The first and second order azimuth modulation are viewed as a vectors where M_1 and M_2 are the vector magnitudes and ϕ_1 and ϕ_2 are the vector orientations. The temporal variability in the σ° azimuth signature is evaluated by observing how these vectors change over time. Examples for the NASA-U and Tunu-N sites are shown in Fig. 4.8. Each point on the scatter-plots indicates a vector endpoint. The vector endpoints are well clustered over individual years indicating that the azimuth modulation is relatively stable annually. The few outliers are attributed to ill-conditioned estimations where the sampling of one or more of the basis elements is insufficient over the given time interval.

Some changes in the azimuth modulation are observed from year to year. The largest change is in M_2 at NASA-U between 1993 and 1994. The orientation of M_2 shifts $\sim 40^\circ$. From 1994 to 1996 the orientation appears to slowly move

66
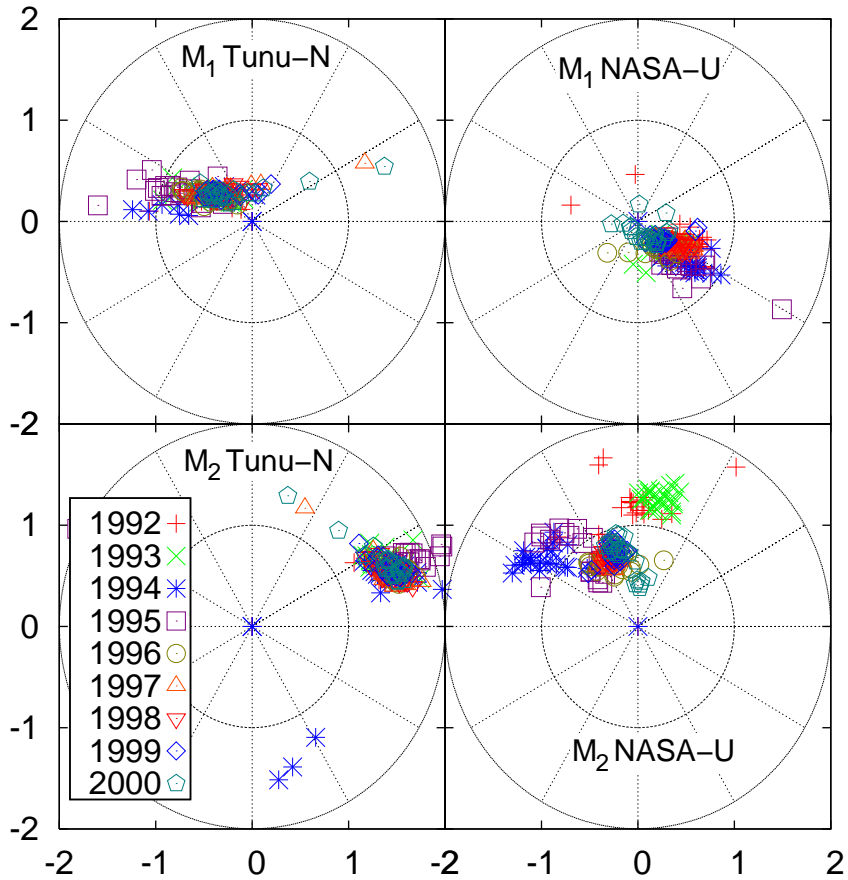
Figure 4.8: Scatter plots of the azimuth modulation parameters. Each symbol represents the end point of a vector representation of the magnitude and orientation of the azimuth modulation.

backward $\sim 20°$ and the magnitude decreases by ~ 0.3 dB. This annual change in azimuth modulation appears to be localized to small areas and is discussed further in Section 4.3.1.

Further investigations across the ice sheet give similar results. Azimuth modulation parameters are consistently well clustered, falling in the same general direction over the nine year period. Two reasons are suggested for the observed long-term stability. First, since the backscatter is a response from multiple buried layers, it represents a long-term average of the annual formation of the surface structure continually buried by additional accumulation. Second, the direction of the average

wind-flow is relatively steady. Because of its stability over time, the azimuth modulation parameters are useful in monitoring long-term inter-annual changes that occur in the average wind flow pattern.

Variation in azimuth dependence with incidence angle

Another question arising in the analysis of the azimuth signature of σ° is how this signature varies with incidence angle. Ledroit et al. [22] state that large scale roughness corresponds with azimuth modulation at low incidence angles and small-scale roughness corresponds to azimuth modulation at high incidence angles. Thus, the variation of azimuth modulation with incidence angle is an indication of the relative roughness of the surface features driving the modulation. The model proposed by Long and Drinkwater [24] for Antarctica assumes that M_1 and M_2 vary linearly with incidence angle, i.e.

$$M_i = c_i + d_i(\theta - 40)$$

where c_i and d_i are constants.

The dependence of azimuth modulation on incidence angle is investigated by plotting the residual errors as defined in Eq. (4.2) versus the basis of the d_i parameters, $b_1 = (\theta - 40)\cos(\phi - \phi_1)$ and $b_2(\theta - 40)\cos(2\phi - \phi_2)$ (see Fig. 4.9). Any dependency of M_1 and M_2 on incidence angle is expected to appear in the plots. The observed dependence is small, approximately ± 0.2 dB, which is significantly smaller than the composite modeling error and noise. This suggests that in the 25° to 45° incidence angle range the dependence of azimuth modulation on incidence angle is relatively insignificant in Greenland. The calculation of the RMS residual errors confirms this, showing negligible improvement when the azimuth modulation magnitude is modeled as a linear function of incidence angle.

4.2.4 Spatial gradient

Inclusion of the spatial gradient in a backscatter model is new. Prior to inclusion of the spatial gradient into the model, I found the largest modeling
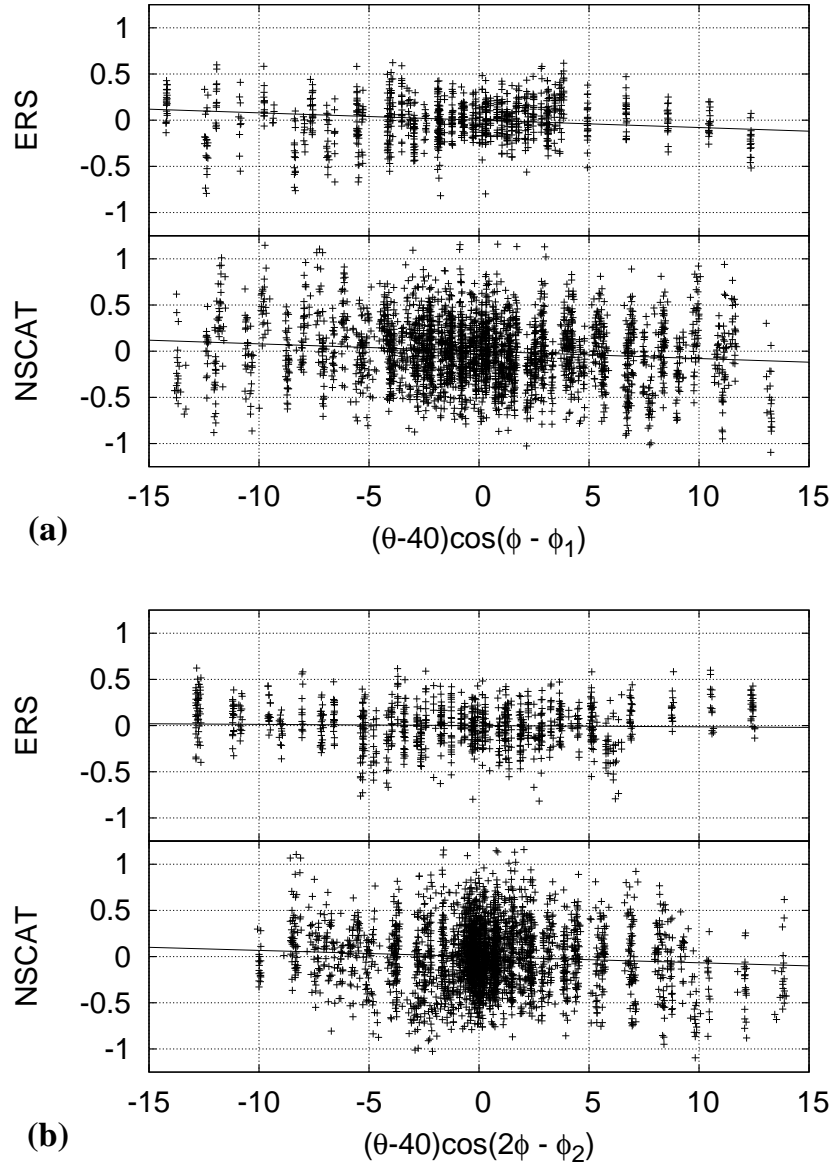
Figure 4.9: Plots indicating the incidence angle dependence of the azimuth modulation magnitude at the NASA-U site. The line in each plot shows a linear fit to the data. (a) ERS and NSCAT residual errors versus $(\theta - 40)\cos(\phi - \phi_1)$, which is a basis for incidence angle dependence of the first order azimuth modulation. (b) ERS and NSCAT residual errors versus $(\theta - 40)\cos(2\phi - \phi_2)$, which is a basis for incidence angle dependence of the second order azimuth modulation. In all cases, the dependence of the azimuth modulation magnitude on incidence angle is small.

error to be in the the percolation zone, the zone with the largest spatial gradient in backscatter. As discussed in Section 4.1, the data set for each study location includes σ° measurements that have centroids within a 25 km radius of the study site. The 50 km resolution backscatter may vary significantly within this radius producing what I term a *co-location* bias in the measurements. In these regions, the co-location bias is significantly reduced by incorporating the spatial gradient into the model. I model the spatial gradient of this data set using

$$h(\mathbf{r}) = s_1(\mathbf{r} \cdot \hat{\mathbf{g}})$$

where s_1 is the magnitude of the gradient, $\hat{\mathbf{g}}$ is a unit vector in the direction of the backscatter gradient, and $\mathbf{r}$ is a vector from the center of the study site to the measurement centroid. Estimating the spatial gradient simultaneously with the other model parameters reduces parameter estimation error caused by non-uniform spatial sampling. Also, by including the spatial gradient in the model, the effects of the co-location bias on the modeling error are reduced, increasing the effectiveness of using the modeling error to determine the applicability of the observation model in characterizing the variability of σ°.

Figure 4.10 shows the dependence of modeling error on $\mathbf{r}$ for ERS and NSCAT data at the NASA-U site for the case where only azimuth and incidence angle dependence are included in the model. The co-location bias is clearly evident in the modeling error. The plots indicate that the co-location bias contributes significantly to the variability of the data set with a bias of ~ 2.4 dB for ERS and ~ 1.1 dB for NSCAT at 25 km from the location center.

The co-location bias has at least two negative effects on σ° analysis in these regions. First, the model parameter estimation may be corrupted based on the spatial sampling of the data set due to unmodeled co-location bias. For example, an estimate of B is corrupted if the co-location bias of low incidence angle measurements is negative and the co-location bias of high incidence angle measurements is positive due to the measurement locations. Second, when the co-location bias is ignored the modeling error is biased high due to the spatial spread of the measurement centroids
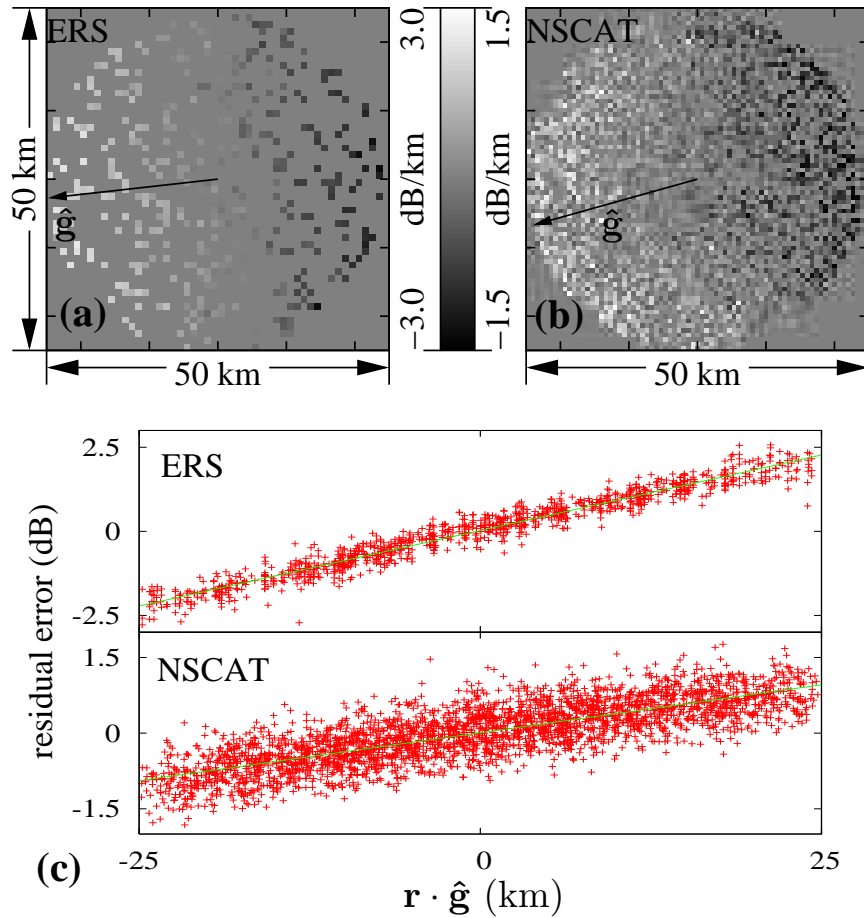
Figure 4.10: Co-location bias plots for the NASA-U site. (a) Magnitude of the residual error for ERS versus the displacement of the measurement center from the NASA-U site. The magnitude of the error is indicated by the gray-scale. (b) Magnitude of the residual error for NSCAT versus the displacement of the measurement center from the NASA-U site. (c) ERS and NSCAT residual errors versus $\mathbf{r} \cdot \hat{g}$, the distance from the center of the study area to the measurement location in the $\hat{\mathbf{g}}$ direction.

71

and the spatial variability in the backscatter. This limits use of modeling error as a tool to evaluate incidence and azimuth angle dependent models.

Images of the magnitude of the spatial gradient (s_1) with streamlines showing the gradient orientation ($\angle\hat{\mathbf{g}}$) are shown in Fig. 4.11. The magnitude of the spatial gradient is largest in the upper percolation zone due to the extreme change in backscatter over this region. In this region, the backscatter varies from some of the lowest σ° values observed over Greenland (near the dry snow zone boundary) to the highest Greenland σ° measurements which occur in the central percolation zone.

Key differences are observed between the σ° spatial gradient at C-band and Ku-band. First, the maximum s_1 values, which are located in the upper percolation zone, are smaller at Ku-band than C-band. Second, the orientation of the gradient shows some frequency differences. An area of note is in the northeast dry snow zone where at C-band the gradient is nearly east-west while at Ku-band the gradient is nearer to north-south. One explanation of this phenomenon originates from the difference in the penetration depth between the two sensors. The east west gradient observed in ERS is attributed to the transition from the dry snow zone to the percolation zone where subsurface ice structures contribute to increased backscatter. However, if this area has not melted significantly over the last few years, the accumulated snow further buries these ice structures and iced firn layers making them less visible at Ku-band than C-band due to the difference in penetration depths. The gradient for NSCAT is smaller in this region and dominated by properties other than the transition between snow zones such as accumulation rate. A second area of difference in $\angle\hat{\mathbf{g}}$ with frequency is the southwest percolation zone. With ERS a single peak is observed in s_1 based on a single discontinuity observed in $\angle\hat{\mathbf{g}}$ in this region. However, for NSCAT there appears to be two separate peaks. This is attributed in part to the higher spatial resolution intrinsic in the NSCAT measurements.

The contribution of the spatial gradient to the overall accuracy of the model is significant. When the spatial gradient is ignored, the RMS modeling error is $\bar{\chi} = 0.737$ dB for ERS and $\bar{\chi} = 0.658$ dB for NSCAT. Including the the spatial
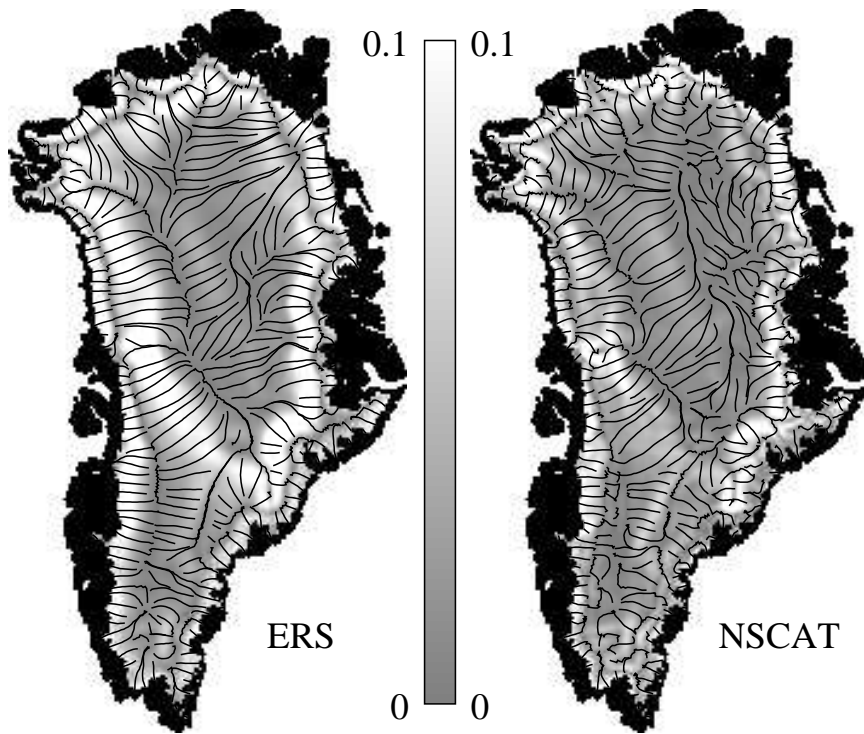
Figure 4.11: Images showing the spatial gradient magnitude (s_1) in dB/km and streamlines showing the orientation of the spatial gradient.

gradient reduces the modeling error by 30% to 50% with $\bar{\chi} = 0.375$ dB for ERS and $\bar{\chi} = 0.458$ dB for NSCAT.

4.2.5 Temporal dependence

Because I am using data over six months, some migration in the mean backscatter is expected during this period. I model this dependence, $p(t - t_0)$ from Eq. (4.1), as a linear function of time over the six month interval

$$p(t - t_0) = T(t - t_0).$$

The images of T for ERS and NSCAT are shown in Fig. 4.12. Two key features are found in these images. First, there is a linear decrease of approximately 1 dB/year over regions of the upper percolation zone. This is attributed to accumulation over a region in the upper percolation zone which experienced melt during the last summer
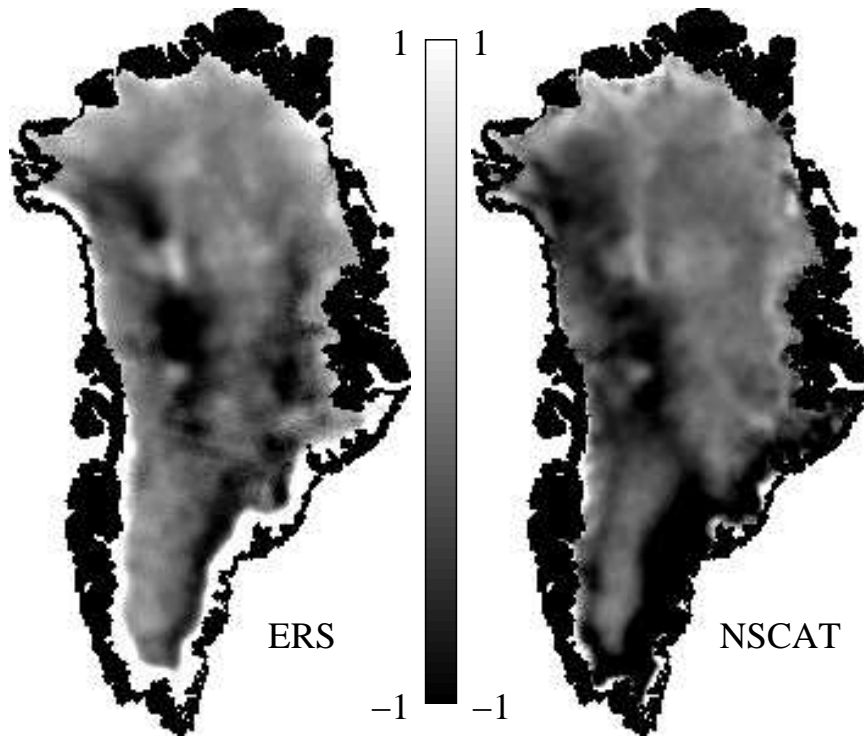
Figure 4.12: Images of T (dB/year) for the 6 months centered around January 1, 1997.

[20]. The second key feature is ~ 1 dB/year estimated increase in $\sigma°$ throughout the wet snow zone as observed by ERS. This feature aids in delineating the wet snow zone from the percolation zone, a division weak in the other parameter images.

The improvement in the model accuracy gained by including temporal dependence is small but non-negligible. Without temporal dependence, the modeling error is $\bar{\chi} = 0.401$ dB for ERS and $\bar{\chi} = 0.470$ dB for NSCAT. When the linear temporal dependence is included the RMS modeling error reduces to $\bar{\chi} = 0.375$ dB for ERS and $\bar{\chi} = 0.458$ dB for NSCAT.

4.3 Applications

The descriptive model presented in this article is applicable for studying both long- and short-term changes over the ice sheet. I present examples of each using ERS data. First, inter-annual changes are shown which indicate regions of

significant variation over the 9 year ERS period. Then, the model is used for study of intra-annual changes. Compared with previous methods, using the model provides a lower variance signal, increasing the ability to detect small-scale short-term variation as well as increased temporal resolution.

4.3.1   Inter-annual change

Annual changes in individual parameters indicate important geophysical changes occurring across the ice sheet. Figure 4.13 shows images of the average of the individual parameters for the 9 year period for ERS. Figures 4.14-4.19 show the yearly anomalies for the individual parameters. The parameter estimates for the individual years are from 6 months of data during mid-winter centered around January 1 of the indicated year.

In the A anomaly images shown in Fig. 4.14, the changes observed near the dry snow/percolation transition zone indicate the reach of the melt each summer [20, 45]. The annual difference images indicate below-average melt during the summers of 1993, 1994, and 1996. In 1995 the melt increases in the west and south. During 1997, the southern dry snow zone is a high melt region. In 1998, the northeast, and in 1999, the south are focus points for increased melt. During 2000, increased melt is observed in an area in the west dry snow zone. The net result is an increase in A from the northwest corner of the dry snow zone, down along the west edge to the southern end, and back up the east side. This is consistent with Wismann [14] and Pack et al. [46].

The changes observed in the B yearly anomaly images in Fig. 4.15 are also associated with the annual melt extent/intensity. In 1993, 1994, and 1996, the B values in the central percolation zone are more negative than average. This is indicative of a below-average intensity melt where a reduced volume of subsurface ice structures form. The resulting reduction in volume-like scattering leads to increased relative contribution from surface scattering from layers causing B to become more negative. This effect is reversed in 1998 and 1999 indicating above average intensity melting. A strong melt event contributes to the formation of subsurface ice structures,
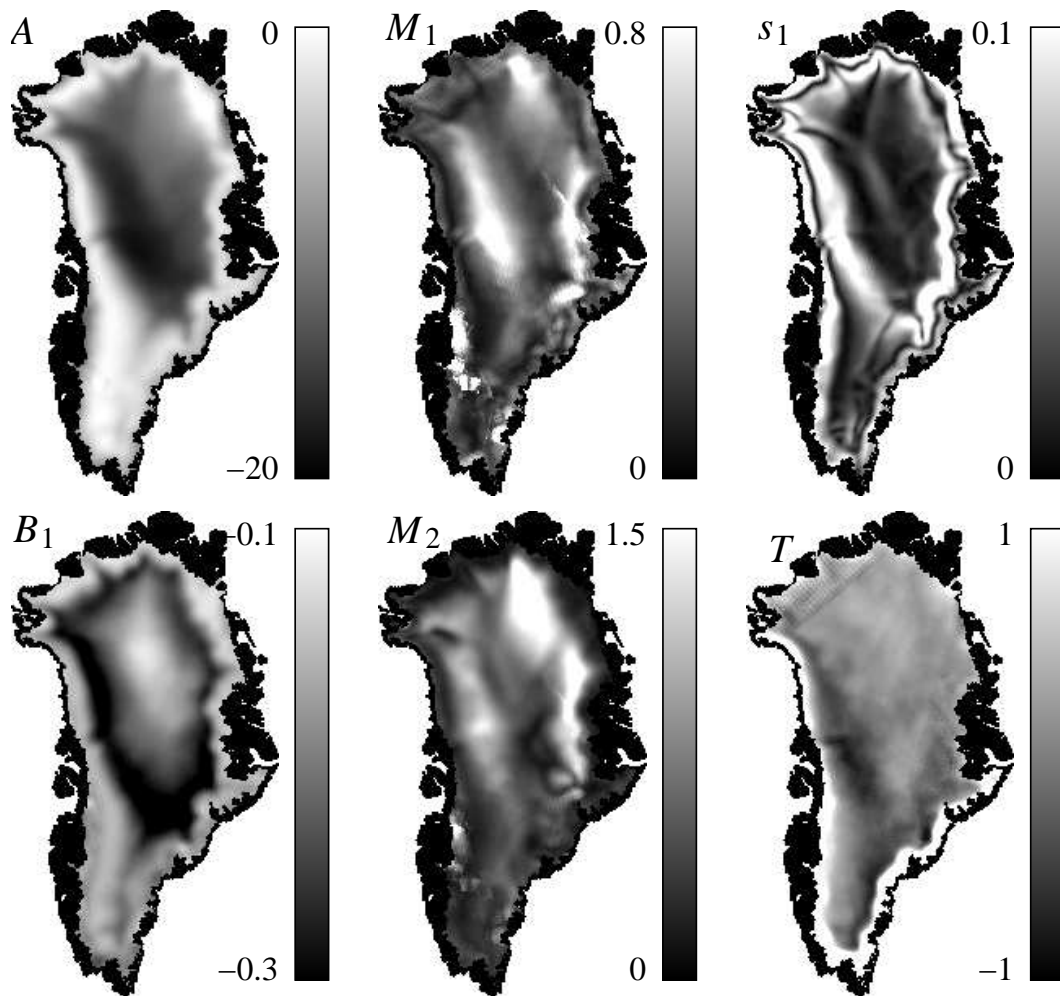
Figure 4.13: Images showing the average model parameter values over 9 years.
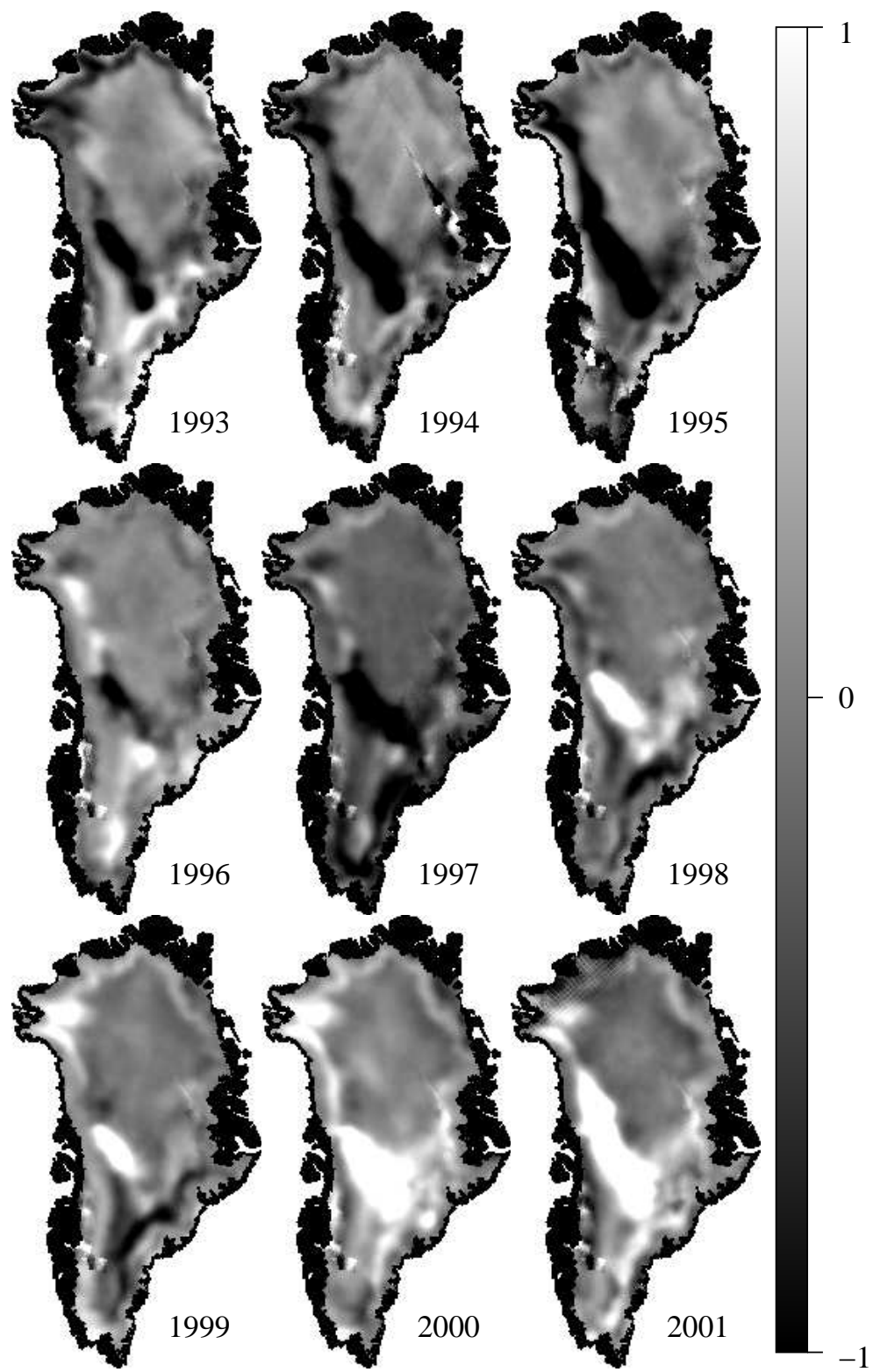
Figure 4.14: Images showing the anomalies in A over 9 years.

increasing volume scattering which causes B to become more positive. In 2000 and 2001, B becomes more negative along the dry snow zone boundary, indicating melt is occurring in areas not affected by melt in recent years. Here, surface scattering increases due to layers of iced firn forming over the previously dry snow.

The M_1 and M_2 yearly anomaly images (see Figs. 4.16 and 4.17) show azimuth modulation variation across the ice sheet. Significant annual changes are observed in small regions of the upper percolation zone as discussed in Section 5. These are the same regions where large changes in A are attributed to increased melt. The net result is a decrease in the azimuth modulation along the upper western percolation zone. Decreases occur in step increments coinciding with increased melt as observed in the A images. One exception where a below-average melt appears to contribute to a significant decrease in the azimuth modulation is observed during the summer of 1993. Both M_2 and A decrease along the western transition zone. The only significant increase in azimuth modulation occurs in M_2 during the summer of 1994 in the eastern transition zone. This increase is short-lived, almost completely vanishing after the next summer.

The s_1 yearly anomaly images shown in Fig. 4.18 are key indicators of the location of the upper percolation zone and the spatial rate of change in the snow properties progressing outward from the dry snow zone. The gradient is large in the upper portion of the percolation zone and decreases downslope as the snow becomes spatially uniform in the number of subsurface ice structures. During 1993, 1994, and 1995, s_1 is lower than average near the dry snow zone boundary indicating that the true boundary between the dry snow zone and percolation zone is further downslope than average. The opposite is observed in the years 1998 and beyond. During these years, s_1 is larger than average indicating an upslope movement of the percolation zone/dry snow zone boundary.

The T anomaly images shown in Fig. 4.19 are an indicators of accumulation rather than melt intensity/extent. In the percolation zone, the more negative values of T correspond to higher rates of accumulation [20]. Each T anomaly image is indicative of the accumulation during the previous year. The T images indicate
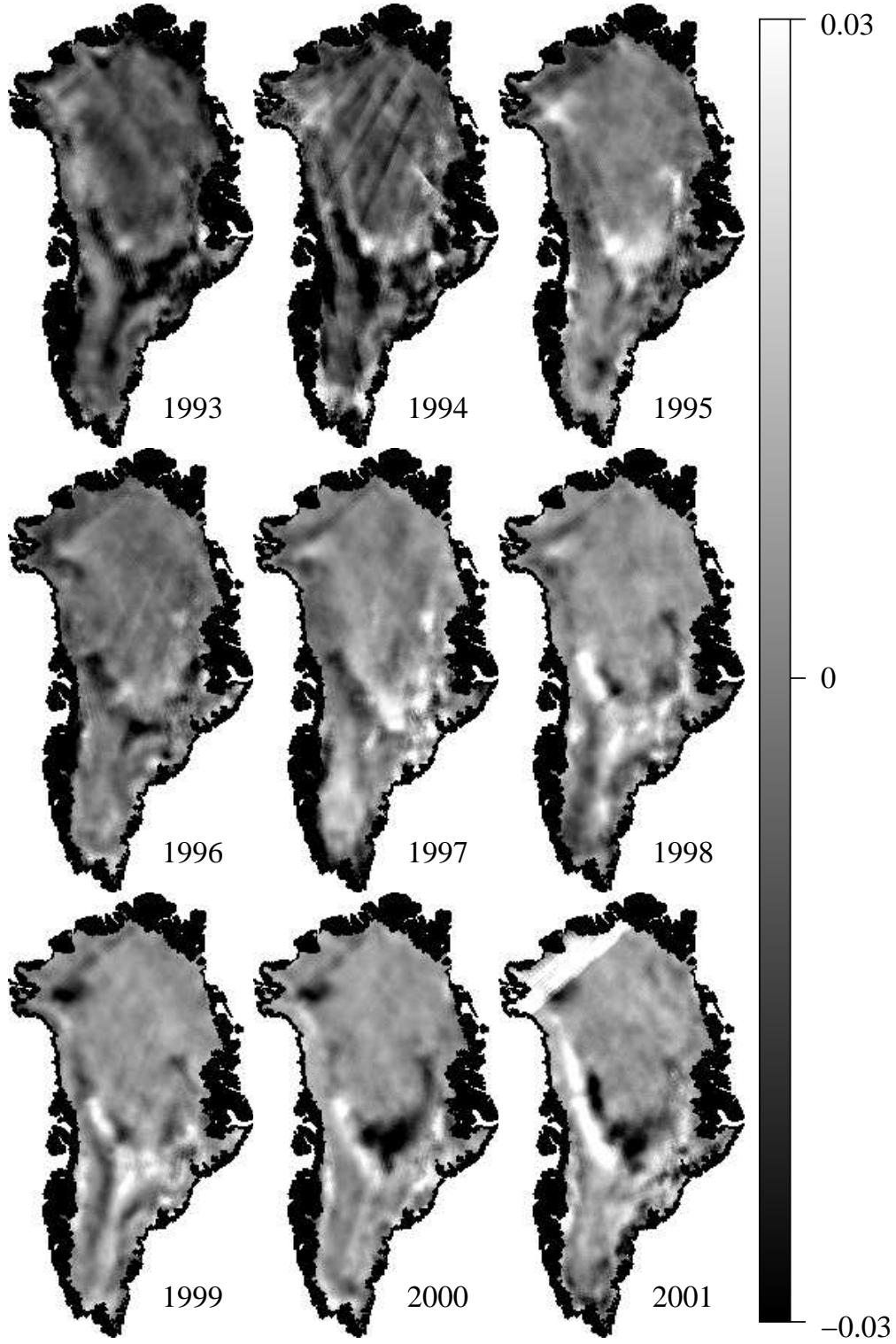
Figure 4.15: Images showing the anomalies in B_1 over 9 years.
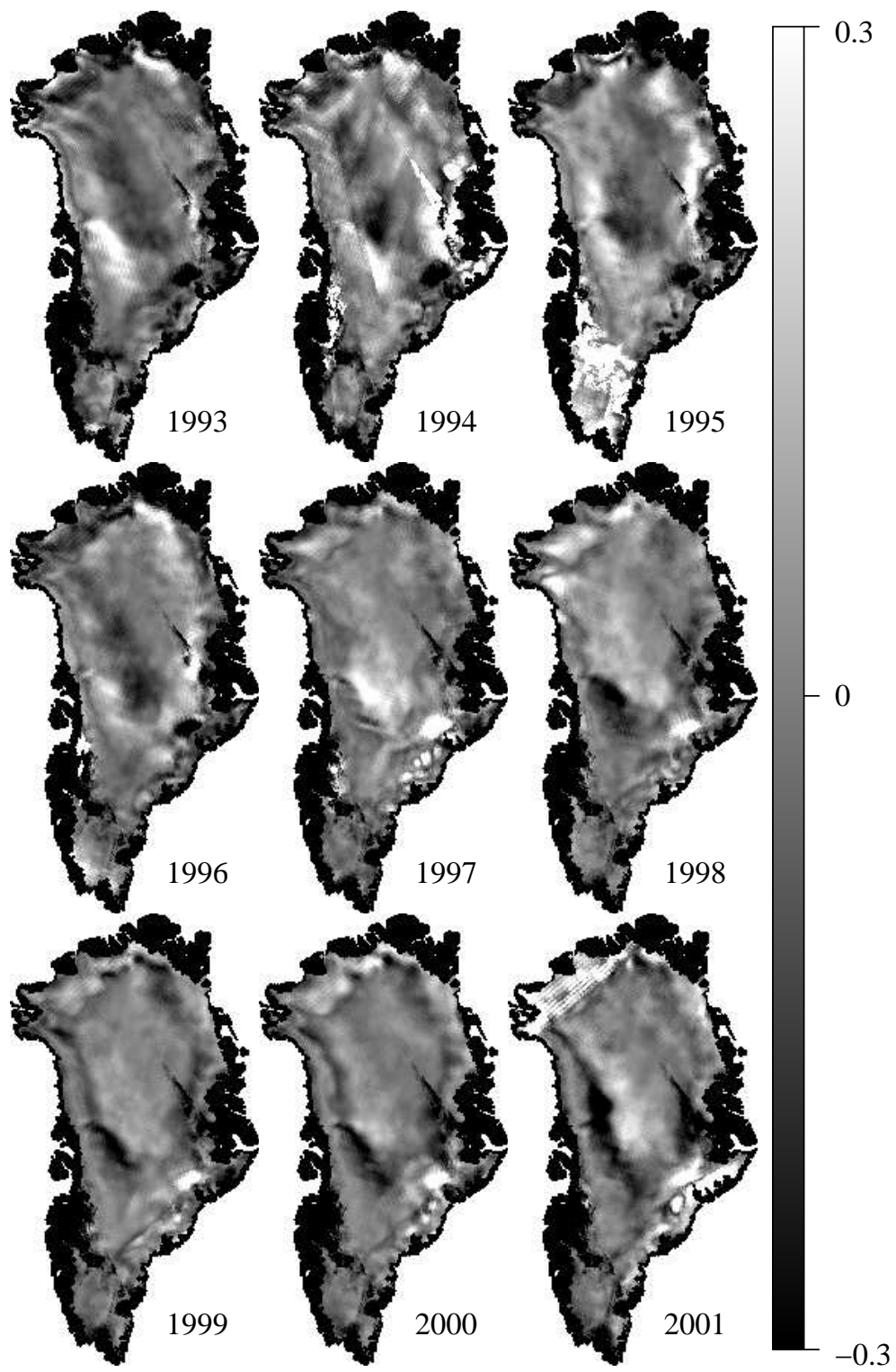
Figure 4.16: Images showing the anomalies in M_1 over 9 years.
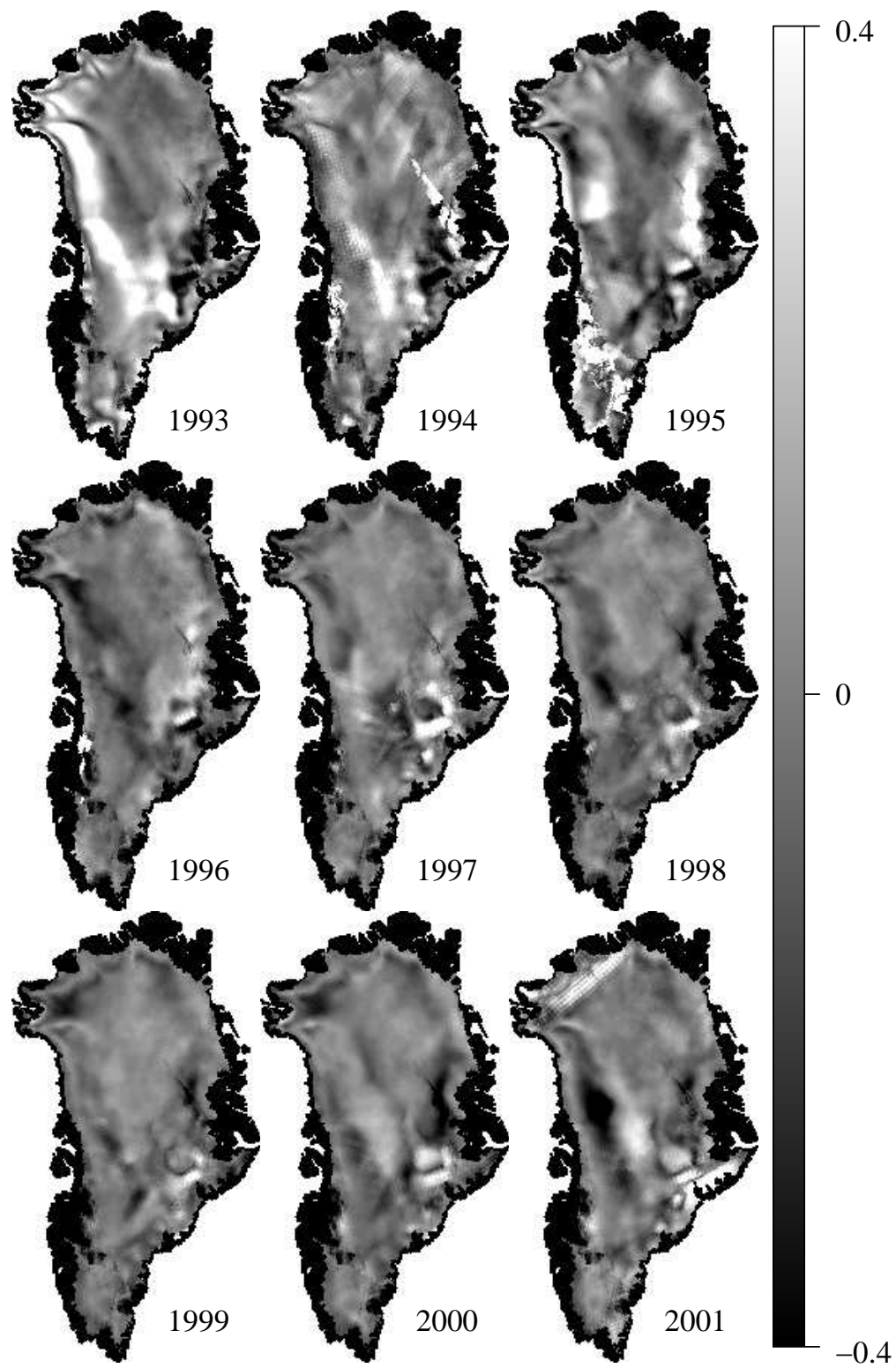
Figure 4.17: Images showing the anomalies in M_2 over 9 years.
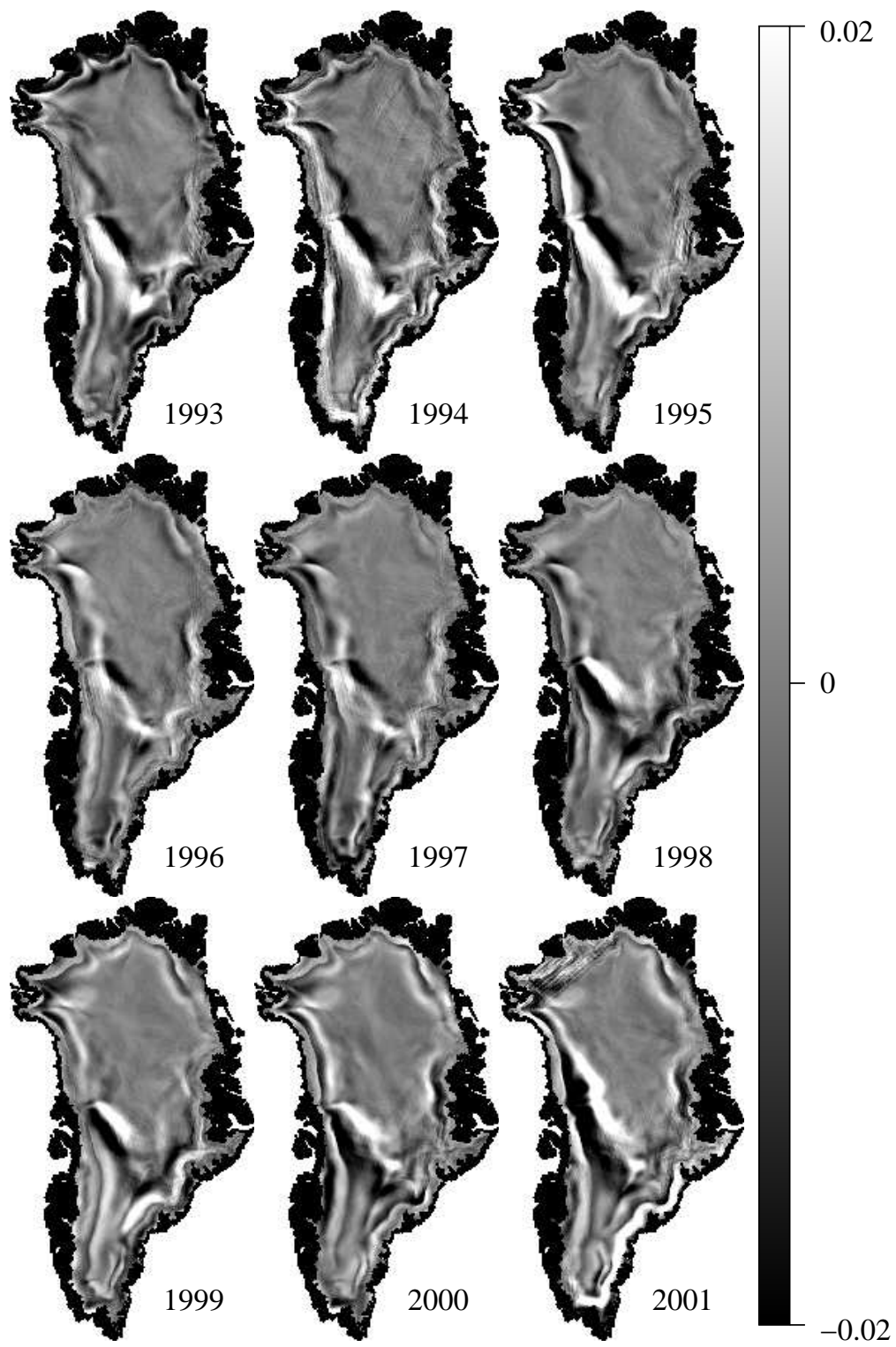
Figure 4.18: Images showing the anomalies in s_1 over 9 years.

that 1993-1994, 1996-1997, 1999-2000, and 2000-2001 were winters with above aver-
age accumulation and 1994-1995, 1997-1998, and 1998-1999 were winters with lower
than average accumulation. These results are consistent with the accumulation esti-
mates of McConnell et al. [47]. The reductions in T observed along the western dry
snow boundary in the 1997 and 2000 images are attributed to an above-average melt
extent the previous summer that results in the linear decrease in σ° associated with
accumulation observed in these new melt areas.

4.3.2 Intra-annual variations

In addition to observing inter-annual changes across the ice sheet, obser-
vations of intra-annual trends are critical to understanding the relationship between
σ° and geophysical properties of the surface. My model is applicable for improved
analysis of surface variation on short time scales. Because complete characteriza-
tion of the microwave signature at fine time scales requires more information than
is presently available or practical, the application of this model to short time-scale
analysis requires some basic assumptions about the microwave signature.

The primary assumption of my method is that for the short time-scale
considered, the variability of σ° with the observation geometry is relatively constant,
and changes in the surface and subsurface primarily affect the average backscatter,
not the variation with observation geometry. Assuming a constant geometry signature
(CGS) is supported by the previous section. Over most of the ice sheet the parameters
describing the dependence of σ° on the observation geometry are relatively constant
over time. The primary location where CGS is questionable is the upper percolation
zone where significant annual changes are observed in the model parameters. These
changes are attributed to summer melt, making the CGS assumption applicable only
during periods between summer melt events.

To develop my methodology for intra-annual analysis using the CGS as-
sumption, I begin with the full model given in Eq. (4.1) where the temporal dependent
term $p(t)$ is subsumed into $A(t)$, i.e.

$$\sigma^\circ = A(t) + f(\theta - \theta_{\mathrm{ref}}) + g(\phi) + h(\mathbf{r}).$$
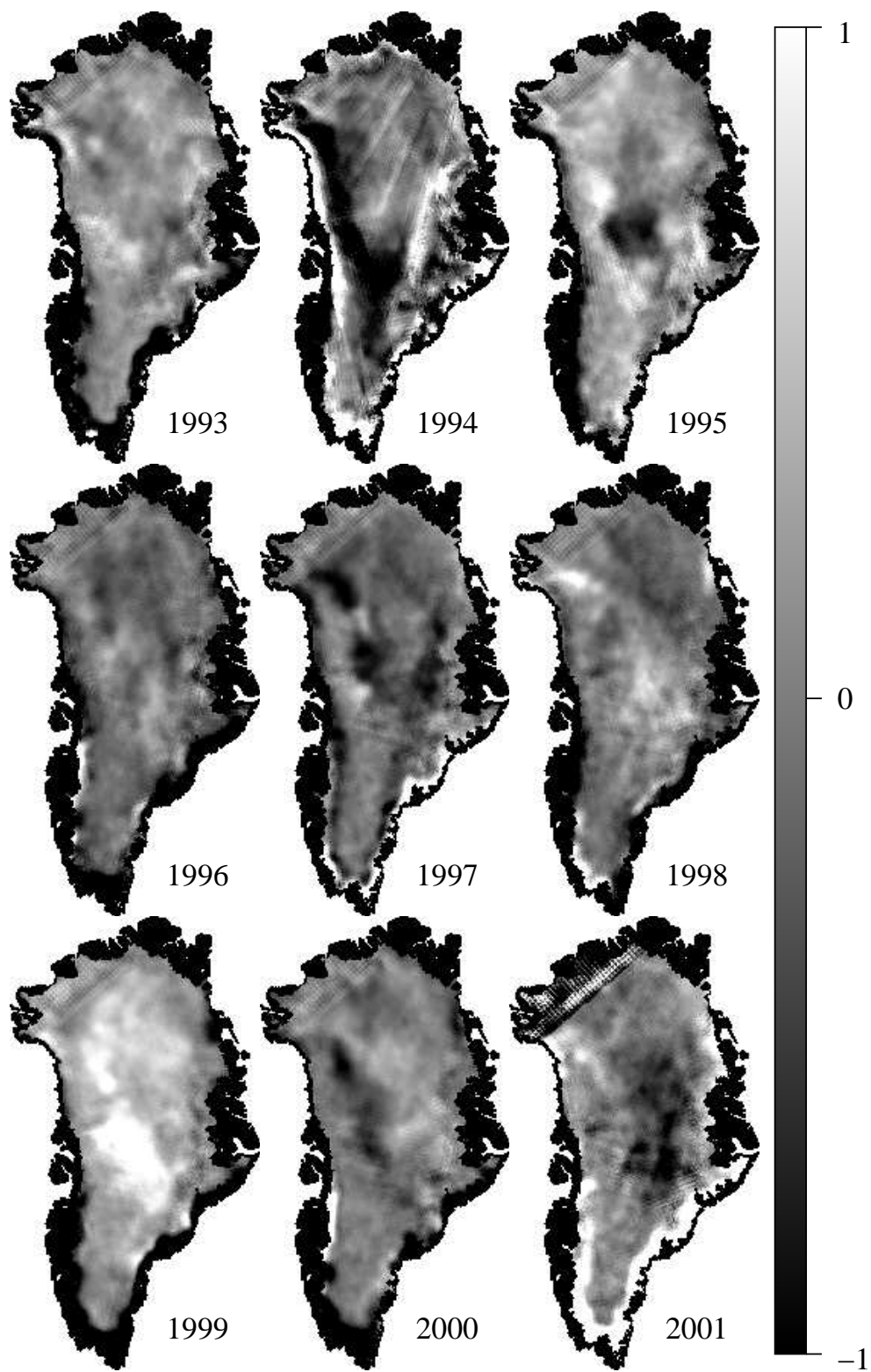
Figure 4.19: Images showing the anomalies in T over 9 years.

With the CGS assumption, only $A(t)$ in this model varies with time. Thus, $A(t)$ contains all information about the temporal variation of the surface. To estimate $A(t)$, I first estimate the geometry-dependent model parameters using least-square estimation based on data over an extended time period. Using the estimated geometry signature, I obtain estimates of $A(t)$ at each measurement time t_i by differencing the measurement (σ_i°) and the observation geometry dependent portion of the model, i.e.

$$A(t_i) = \sigma_i^\circ - f(\theta_i - \theta_{\text{ref}}) - g(\phi_i) - h(\mathbf{r}_i).$$

The result is an estimate of the variation of the average backscatter over time.

Variations in the average backscatter $(A(t))$ have been used to estimate accumulation [18, 20], monitor melt and ablation [6, 14], and study long term climate change [10, 48]. Using my model with the CGS assumption enables lower variance estimates of $A(t)$ and increased temporal resolution compared with the methods used in these studies. Without the CGS assumption, the dependence on observation geometry must be re-estimated with each estimate of the average backscatter. There are several drawbacks to continually re-estimating the dependence of σ° on the observation geometry. First, to enable higher temporal resolution, a simpler model must be used. This results in residuals from unmodeled dependencies increasing the variance in the observation signal. Second, to increase temporal resolution, a relatively small number of data samples are used. This may contribute to poor estimates of the model parameters due to limited sampling in incidence angle and/or other modeled dependencies. Third, even with the simplified model, multiple days of data are typically required to obtain estimates of the average backscatter, significantly limiting the achievable temporal resolution.

Assuming CGS provides significant improvement in each of these areas. Errors in the signal due to observation geometry sampling are mitigated using my more complete descriptive model. Using data from an extended time period increases the number of samples, making the estimation of the dependence on observation geometry much more robust. The best temporal resolution is equal to the temporal

sampling of the sensor because each σ° measurement is associated with an estimate $A(t_i)$.

To evaluate the performance using CGS, I examine two examples in which the results using CGS are compared with results assuming variable geometry signature (VGS). For VGS I use the method from the studies mentioned above. The simplified model for observation geometry dependence is

$$\sigma^\circ(\theta) = A + B(\theta - \theta_{\text{ref}}),$$

which includes incidence angle dependence only. A and B are estimated using linear least-squares regression for three days of ERS data within a 25 km radius of the study site. Estimates are made at 3 day intervals.

For the CGS method, the full model parameters are estimated using ERS data from the six month interval including October 1997 through March 1998. The $A(t_i)$ values are averaged over three days so that the two methods are consistent in time sampling. The averaging also reduces the variance of the signal at the cost of lowering the temporal resolution.

Both methods are used to estimate the temporal variation in the backscatter at two locations. The estimates are shown in Figs. 4.21 and 4.22. For both cases, the variance of the CGS estimates of A is much smaller than the variance of the VGS A estimates. At location 1, which is in the dry snow zone, there is a crest in the CGS A estimates around the beginning of 1998 which is obscured in the VGS A estimates due to noise. Location 1 is also in a region where the azimuth dependence of σ° is relatively large. The bottom plot for location 1 shows the signal due only to changes in azimuth sampling, which has been removed from CGS A estimates in the center plot by including azimuth dependence in the full model.

Location 2 is in the upper percolation zone. During the summer of 1997 a short melt event occurred that is observed as an abrupt drop in A followed by a small increase in the average value of A. This melt signal is difficult to detect from the VGS A estimates due to the high variance. Note that although the CGS geometry signature estimates are from the 6 months of data centered around Jan. 1, 1998,

Figure 4.20: ERS A image with study points indicated.

two years of A estimates are shown. Prior to the melt event during the summer of 1997, there is an increased variance in the CGS A estimates. This is attributed to fundamental changes in the geometry signature occurring with the melt. The CGS geometry signature model, which was estimated from data after this melt event, does not accurately model the geometry dependence prior to the melt. Notwithstanding this modeling error, the variance of the CGS A estimates is consistently smaller than that of the VGS A estimates, even prior to the melt.

At location 2, the spatial gradient is large. The bottom plot for location 2 shows an estimate of the variation in the signal due only to the co-location bias from the spatial sampling of the measurement locations. This signal has been removed from CGS A estimates by including the spatial gradient in the model of the microwave signature of the snow.

These examples show some of the advantages of using the CGS assumptions when applicable. A key improvement is the reduced variance in the signal and the
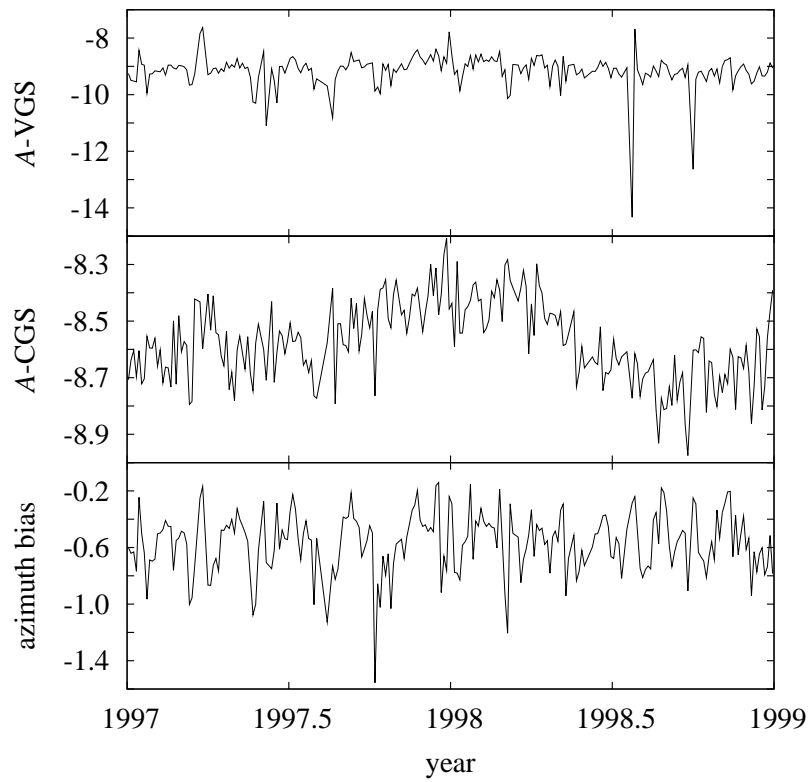
Figure 4.21: Comparison of CGS A estimates and VGS A estimates at Location 1 (78.6 N, 35.5 W) which is in an area significantly affected by azimuth modulation. The bottom plot for shows the estimated bias over time due only to azimuth sampling.
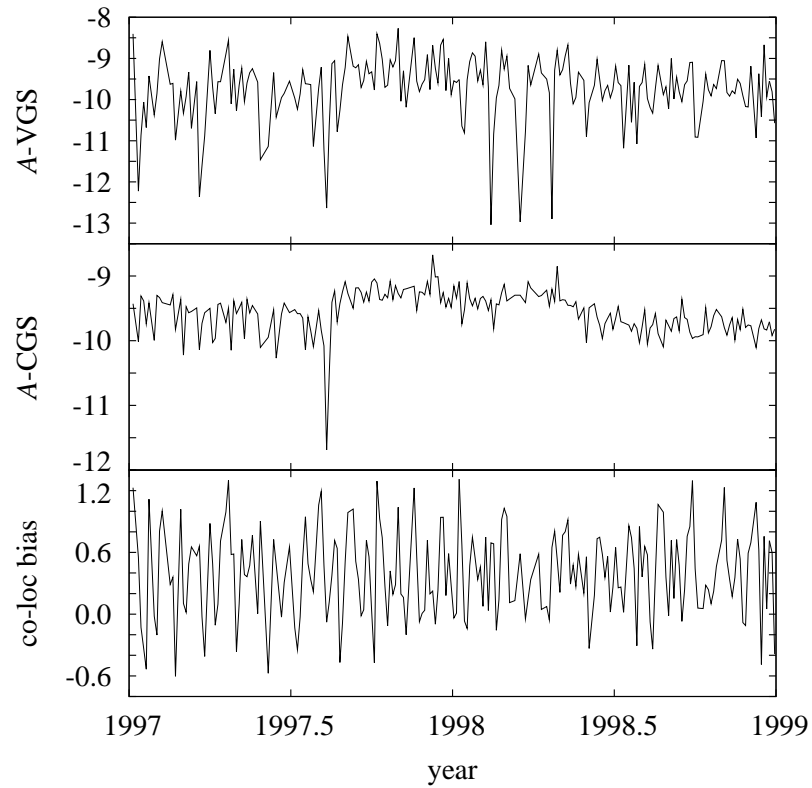
Figure 4.22: Comparison of CGS A estimates and VGS A estimates at Location 2 (69.1 N, 35.7 W). A small melt event is observed as a sharp drop in A-CGS which is obscured by the noise in the VGS A estimates. Location 2 is in an area significantly affected by co-location bias. The bottom plot for location 2 shows the estimated bias over time due only to the spatial sampling of the measurements.

removal of unrealistic spikes in the data. The reduced variance is attributed in part to the inclusion of the azimuth and spatial gradient dependencies in the model. Higher temporal resolution may be obtained by averaging the CGS $A(t_i)$ estimates over shorter time intervals at the cost of increased noise.

4.4 Summary

The σ° of the Greenland ice sheet may be modeled at a given point in time over a small region as a function of incidence angle, azimuth angle, measurement location, and measurement time. The contribution of each modeled dependency to the overall accuracy of the model is largest for incidence angle, which, in general, is followed by measurement location, then azimuth dependence, and finally, measurement time. The measurement location dependence is most significant in the upper percolation facies. Azimuth dependence is most significant in the lower dry snow zone, tapering off in the upper percolation zone. The azimuth dependence is primarily second order and exhibits little dependence on incidence angle. The orientation of the azimuth dependence is correlated with wind patterns across the ice sheet.

I have given examples of two applications for the descriptive model developed herein. First, changes in the model parameters are valuable for tracking inter-annual changes on the ice sheet. Observed trends include increases and decreases in the melt intensity and extent, as well as inter-annual variations in accumulation. Second, the model is applicable for analysis of short-term variation in the average backscatter. Combined with the constant geometry signature (CGS) assumption the model enables the estimation of average backscatter with smaller variance and/or increased temporal resolution compared with methods employed in previous studies.

The model also has other applications. For SAR, a knowledge of the azimuth modulation properties of the Greenland ice sheet is critical for accurate studies. Without proper adjustment for azimuth dependence, effects of a change in azimuth angle in an inter-comparison of SAR σ° may be mis-interpreted as physical change. Additionally, uncompensated azimuth dependence may result in image corruption for

wide angle SAR. Comparisons between in-situ and SAR measurements could also be effected by azimuth biases.

Chapter 5

Melt Detection

The Greenland ice sheet is an important factor in global sea level change, the earth's radiation budget, and other areas of global environmental concern. Measuring the melt occurring each year on the ice sheet is important in understanding the impact of Greenland in these areas. Approximately 8% of the world's ice is located on the Greenland ice sheet with melting from the ice sheet estimated to contribute 7% to the current rise in sea level [3]. In relation to the Earth's radiation budget, rising temperatures cause increased melt extent. Even small temperature changes can affect large areas due to the shallow slope of the ice sheet. Wet snow absorbs approximately 45% more incoming solar radiation than dry snow [5]. This increase in absorbed radiation with increasing temperatures represents unstable positive feedback in our climate.

Microwave measurements of brightness temperature (T_b) and the normalized radar cross-section ($\sigma°$) are excellent tools for estimating melt duration and extent. The introduction of even small amounts of liquid water into the snow pack dramatically impacts the electrical properties of the snow at microwave frequencies. This results in large changes in the microwave measurements of the surface, enabling melt detection. Current satellites measuring $\sigma°$ and T_b provide coverage of the complete ice sheet at least twice daily.

Microwave measurements have been successfully used in multiple studies to detect melt duration and extent over Greenland. A single channel threshold has been used with T_b by Mote et al. [11], Mote and Anderson [12] and with $\sigma°$ by Wismann [14] and Ashcraft and Long [49]. Abdalati and Steffen [2, 4, 5, 13] used a

frequency/polarization combination of T_b to detect melt, and Nghiem et al. [15] used the diurnal variability in $\sigma°$ to detect melt.

Although various methods have been used to detect Greenland melt, there have been no large-scale comparison between these methods. My object is to provide an inter-comparison between existing methods as well as to introduce a new method for melt detection. This is accomplished by comparing the melt duration and extent obtained from various melt detection method and sensor combinations. The differences and similarities are discussed in light of the theoretical differences between the various methods and the differences in sensitivity to melt between sensors.

This chapter is organized as follows: Section 5.1 provides a short review of sensors and data sets used for in this chapter for melt detection. This section also includes a short discussion on the data processing method used to obtain estimates of T_b and $\sigma°$ on a regularly spaced grid at regular intervals in time. Section 5.2 introduces a simple model for a melt event and the effects of melt on T_b and $\sigma°$. In Section 5.3, this model is employed to formulate methods to detect melt using T_b and $\sigma°$. Selected melt detection methods from other papers are also briefly introduced. Section 5.4 presents a comparison between various melt detection methods accompanied by a discussion of the observed and theoretical differences and similarities between the various melt detection methods. Section 5.5 contains a summary and conclusions.

5.1 Background

The T_b data used in this study is from SSM/I and includes measurements from 19.35 GHz vertical and horizontal polarized channels (19V and 19H) and the 37.0 GHz vertical polarization (37V) channel from the SSM/I instrument aboard the F-14 satellite. The $\sigma°$ measurements are from QSCAT and ERS and only vertical polarization data are used.

In order to compare the measurements from the different sensors, the raw T_b and $\sigma°$ data are processed to obtain estimates regularly sampled in space and time using the non-parametric fit described in Eq. 2.5. For the weighting, the truncated
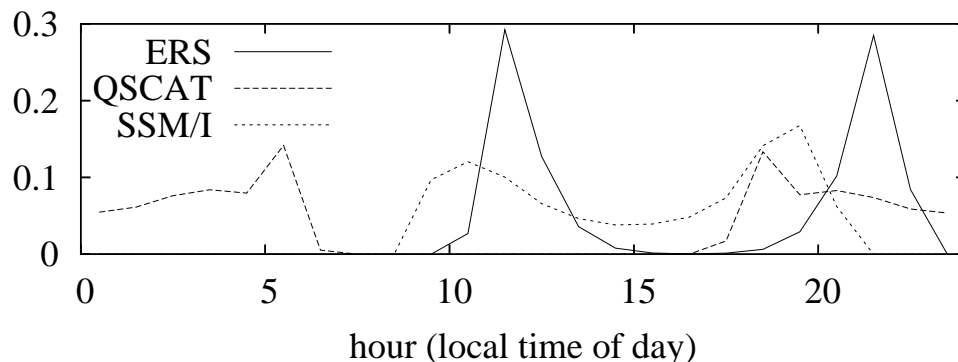
Figure 5.1: Density (normalized histogram) of sampling times for the various sensors. For melt detection, T_b and σ° are estimated at 18:00 which is close to a peak in the density of both the QSCAT and SSM/I samples The peak in the ERS samples is a few hours later in the evening, but is still relatively close to the estimation time.

Gaussian

$$w(\tau, t_i) = \begin{cases} e^{-\frac{1}{2}(t_i - \tau)^2/\sigma_t^2} & \text{if } |t_i - \tau| < \Delta t_{\max}, \\ 0 & \text{if } |t_i - \tau| \geq \Delta t_{\max} \end{cases}$$

is used.

Each sensor samples Greenland at different times of day (see Fig. 5.1). To mitigate the effects of the difference in sampling time on melt detection comparison, we compare σ° and T_b estimates at 18:00 local time each day which is near a peak in the time sampling distribution for each sensor. Because the peak sample time for ERS (21:30 local time) is later in the evening past peak melt, it is expected that ERS will detect less melt than the other sensors. For SSM/I and QSCAT the non-parametric fit parameters are $\sigma_t = 6$ hours and $\Delta t_{\max} = 2$ days. For ERS the parameters are $\sigma_t = 24$ hours and $\Delta t_{\max} = 8$ days. The relatively large values for $\Delta t_{\max}$ allow for interpolation over days with missed coverage.

SSM/I and QSCAT provide complete coverage of the ice sheet twice daily. ERS requires 3 days for complete coverage because its swath is narrower. Although ERS requires 3 days to completely cover the ice sheet, it covers approximately 80% of the ice sheet daily making 1 day resolution possible over much of the ice sheet.

5.2   Theory

The general concept of microwave detection of melt is the same for different methods; however, the application of the theory varies. The theory related to melt detection is presented by first providing an overview of the sensitivity of T_b and σ° to melt and then addressing the the application of theory specific to each method.

5.2.1   Melt event model

Microwave measurements are very sensitive to the introduction of liquid moisture into the snow-pack. The most significant change in the electro-magnetic properties is a large increase in the imaginary part of the dielectric constant (ϵ''). The introduction of only 0.5% liquid moisture content can increase ϵ'' by over an order of magnitude [25]. This increases absorption and reduces the penetration depth. The net result of melt is a large decrease in σ° and a large increase in T_b (see Fig. 5.2).

The progress of a snow-pack from a frozen state to one where melt is present is a continuous process in which the dividing point between freezing and melting is not well defined. The degree of melt is measured as the percent liquid moisture content (m_v) of the snow. In this work, a melt event is defined based on a m_v threshold and a minimum depth (d) of wet snow. The surface is classified as melting when m_v in the top layer of depth d of snow exceeds some threshold. A simple physical model is employed to relate this definition of melt to a T_b and a σ° threshold for melt detection.

In this simple physical model of a melt event, it is assumed that at melt onset a uniform layer of wet snow with depth d lies over an infinite half space of dry snow or ice (see Fig. 5.3). A model for the brightness temperature at the radiating from the air/snow boundary in terms of the brightness temperature at a point on the wet/dry snow boundary ($T_b(d)$) is [26, pg. 216]

$$T_b(0) = T_b(d)e^{-\tau(0,d)} + \int_0^d \left[\kappa_a(z)T_{\text{wet}}(z) + \kappa_s(z)T_{sc}(z)\right] e^{-\tau(0,z)} \sec\theta(z)\,\mathrm{d}z \qquad (5.1)$$

where
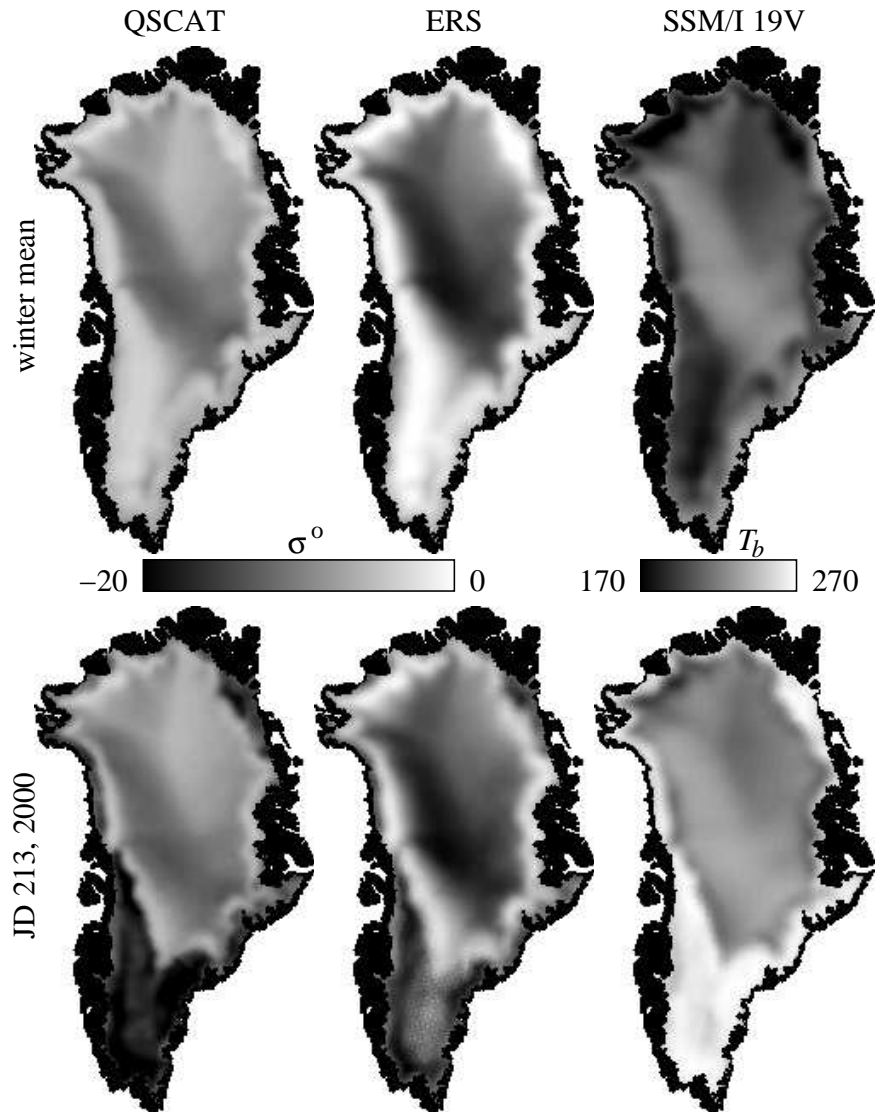
Figure 5.2: Images of QSCAT σ°, ERS σ° normalized to 40° incidence angle, and SSM/I 19.35 GHz vertical polarization T_b. Top: images of the winter mean using data from December 1, 1999 to February 28, 2000. These winter mean images are the estimates of $\sigma^\circ_{\mathrm{dry}}$ and T_b^{dry} used in the implementation of α-based melt detection. Bottom: images of σ° and T_b estimates on JD 213, 2000. This is a period of intense melt.
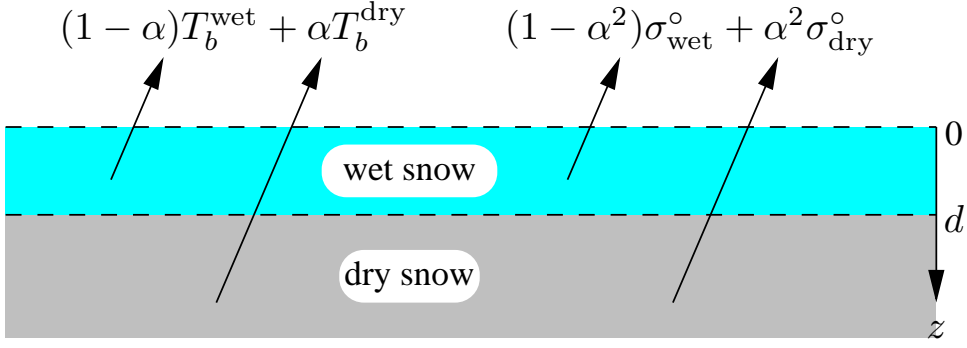
Figure 5.3: Simplified physical model of a melting surface. The composite T_b of the surface includes the emission from the wet snow and the emission from the dry snow attenuated by the wet snow layer. The composite backscatter is similarly a contribution from the wet snow and an attenuated contribution from the subsurface frozen snow.

κ_a - absorption loss coefficient,

κ_s - scattering loss coefficient,

κ_e - extinction coefficient $(\kappa_a + \kappa_s)$,

T_{wet} - wet snow physical temperature in Kelvin,

T_{sc} - scattered radiometric temperature,

$\tau(z_1, z_2)$ - optical length $(\int_{z_1}^{z_2} \kappa_e(z) \sec(\theta(z)) \, \mathrm{d}z)$, and

$\theta(z)$ - transmission angle at depth z.

Assuming the wet snow layer is uniform in all significant respects, Eq. (5.1) can be rewritten

$$T_b(0) = T_b(d)e^{-\kappa_a^{\mathrm{wet}} d \sec \theta_{\mathrm{ws}}} + \frac{\kappa_a^{\mathrm{wet}}}{\kappa_e^{\mathrm{wet}}}(1 - e^{-\kappa_e^{\mathrm{wet}} d \sec \theta_{\mathrm{ws}}})T_{\mathrm{wet}}$$

$$+ \int_0^d \kappa_s(z) T_{sc}(z) e^{-\tau(0,z)} \sec \theta(z) \, \mathrm{d}r' \tag{5.2}$$

where θ_{ws} is the transmission angle through the wet snow. In wet snow absorption loss dominates over scattering, so $\kappa_a^{\mathrm{wet}} \gg \kappa_s^{\mathrm{wet}}$ and $\kappa_e^{\mathrm{wet}} \approx \kappa_a^{\mathrm{wet}}$. Assuming the contribution from multiple scattering (T_{sc}) is negligible, Eq. (5.2) becomes

$$T_b(0) = \alpha T_b^{\mathrm{dry}} + (1 - \alpha)T_{\mathrm{wet}} \tag{5.3}$$

where $\alpha = e^{-\kappa_a d \sec \theta_{\text{ws}}}$. Based on this model, T_b asymptotically approaches T_{wet} with increasing thickness of the wet snow layer.

In this brightness temperature model I ignore reflections at the air/wet snow boundary and the wet/dry snow boundary. This is valid for SSM/I vertical polarization because the measured emission is near the Brewster angle making the effects of surface reflection minimal.

To estimate the effect of melt on σ°, I model the volume backscatter from the snow as

$$\sigma^\circ = \int_0^\infty \gamma(z) e^{-2\tau(0,z)} \sec \theta(z) \, \mathrm{d}z \qquad (5.4)$$

where $\gamma(z)$ represents the backscatter from an incremental volume. By separating the integral into the contribution from the wet snow and the contribution from the dry snow, Eq. (5.4) can be rewritten as

$$\sigma^\circ = \alpha^2 \sigma^\circ_{\text{dry}} + (1 - \alpha^2) \sigma^\circ_{\text{wet}} \qquad (5.5)$$

where

$$\sigma^\circ_{\text{dry}} = \int_d^\infty \gamma(z) e^{-2\tau(d,z)} \sec \theta(z) \, \mathrm{d}z,$$

$$\begin{aligned} \sigma^\circ_{\text{wet}} &= \int_d^\infty \gamma_{\text{wet}} e^{-2\kappa_e^{\text{wet}} z \sec \theta_{\text{ws}}} \, \mathrm{d}z \\ &= \frac{\gamma_{\text{wet}}}{2\kappa_e^{\text{wet}}}, \end{aligned}$$

and α is defined as in the T_b model. In this equation $\sigma^\circ_{\text{dry}}$ represents the dry snow backscatter without the overlying wet snow layer, and $\sigma^\circ_{\text{wet}}$ represents the volume backscatter from and infinite half-space of wet snow. Note that for backscatter, α is squared due to the two-way attenuation through the wet snow layer. Just as with the T_b model, surface reflections at the air/snow and wet snow/dry snow boundaries are ignored, which is appropriate for vertical polarization. Surface scattering from subsurface layer interfaces (which may be significant) is included in the bulk scattering described by $\sigma^\circ_{\text{dry}}$.

To obtain κ_a^{wet}, the bulk relative dielectric constant (ϵ_r) of the wet snow layer is estimated using the method presented in Ulaby et al. [38, pg. 2072]. The wet

Table 5.1: Calculated wet snow electrical properties corresponding to the three sensors. The air/snow power transmissivity (Υ) is shown for vertical polarization only and is near unity indicating minimal surface scattering.

sensor	ERS	QSCAT	SSM/I
frequency	5.3 GHz	13.4 GHz	19.35 GHz
incidence angle	~ 40	56	53.1
ϵ_r	$1.81 + i0.032$	$1.77 + i0.034$	$1.44 + i0.029$
κ_a (Np/m)	2.63	7.14	9.74
Υ	0.994	0.999	1.000

snow is assumed to have a liquid moisture content m_v=1.0% which matches the value used by Mote and Anderson [12] and Abdalati and Steffen [2]. A density of $\rho = 0.4$ g/cm^3 is assumed, which is consistent with observations of Greenland snow [30]. The absorption coefficient is

$$\kappa_a = 2\frac{2\pi f}{c}\Im\left\{\sqrt{\epsilon_r}\right\}$$

where f is the frequency, c is the speed of light in a vacuum, and $\Im\{\cdot\}$ represents the imaginary part. The power transmission coefficient (Υ) for vertical polarization across the air/wet snow boundary is calculated using ϵ_r based on Fresnel reflection. The values of ϵ_r, κ_a, and Υ for each of the sensors are listed in Table 5.1.

5.3 Melt Detection Methods

Results are compared for the various melt detection methods over Greenland during the year 2000. A primary goal of this comparison is to inter-relate the spatial and temporal consistency of the individual methods. Additionally, this comparison serves as a validation for the individual melt detection approaches using independent estimates of the daily melt extent. This validation is important because *in situ* validation of large-scale melt detection is difficult due to the limited amount of data available. This comparison includes six different approaches: Three are based on T_b measurements from SSM/I, and the other three use σ° measurements from ERS and QSCAT.

In general, melt detection for each method is based on thresholding some melt signal ($q(t)$) which varies with time. Let $m(t)$ represent the melt detection with $m = 1$ indicating melt and $m = 0$ indicating non-melt, i.e.

$$m(t) = \begin{cases} 1 \text{ if } q(t) \geq q_0 \\ 0 \text{ if } q(t) < q_0. \end{cases}$$

Each method is composed of two parts: the definition for $q(t)$ and a constant threshold q_0.

5.3.1 α-based methods

The simplified melt event model introduced in Section 5.2.1, along with Eqs. (5.3) and (5.5), is used as a basis for melt detection using QSCAT, ERS, and SSM/I measurements. This is termed α-based melt detection because the threshold is based on the attenuation in the wet snow layer, α. The details on the implementation of α-based melt detection for the different sensors, including the definition for q and the value of q_0, are discussed below.

QSCAT

QSCAT measurements have been used in few studies detecting melt extent and duration over Greenland. I initially used a method based on the mean and standard deviation of σ° during the winter where a drop in σ° of eight winter standard deviations below the winter mean indicates a melt [45]. Nghiem et al. [15] also use QSCAT to detect melt over Greenland. Their method is based on the diurnal variability and is discussed in more detail later.

In this section a method is presented for melt detection using QSCAT and the simple melt model from the previous section. This is termed the Q-α method. A similar method was employed by Wismann [14] for melt detection using ERS measurements.

Recalling that $\sigma^\circ_{\text{wet}}$ is relatively small (typically over 10 dB below $\sigma^\circ_{\text{dry}}$), the contribution from the $(1 - \alpha^2)\sigma^\circ_{\text{wet}}$ term in Eq. (5.5) is assumed negligible. In this

case, melt is indicated by

$$\sigma^\circ < \alpha^2 \sigma^\circ_{\text{dry}}$$

which in dB is written

$$\sigma^\circ < \sigma^\circ_{\text{dry}} + 2\text{dB}(\alpha).$$

Formulated in terms of q and q_0, the definitions are

$$q(t) = \sigma^\circ_{\text{dry}} - \sigma^\circ(t) \quad (\text{in dB})$$

with $q_0 = 2\text{dB}(\alpha)$.

In this method, the signal $q(t)$ represents the deviation in σ° from the backscatter from a dry snow surface. Because σ° is relatively constant during the non-melt period, $\sigma^\circ_{\text{dry}}$ can be estimated as the average over the winter period when no melt is expected to occur. In general, $\sigma^\circ_{\text{dry}}$ is a function of the observation geometry including the incidence angle (θ) and the azimuth angle (ϕ). Additionally, it is dependent on the offset ($\mathbf{r}$) of the measurement centroid from the estimation point of the average σ°. The method from Chapter 4 is used to estimate these dependencies where

$$\sigma^\circ(\phi, \mathbf{r}) = A + M_1 \cos(\phi - \phi_1) + M_2 \cos(2\phi - \phi_2) + s(\mathbf{r} \cdot \hat{\mathbf{g}})$$

with the model parameters A, M_1, ϕ_1, M_2, ϕ_2, s, and $\hat{\mathbf{g}}$ obtained through linear least-squares regression. Because of the narrow incidence angle sampling by QSCAT, incidence angle dependence is ignored.

The model parameters are estimated using 3 months of data from Dec. 1, 1999 to Feb. 28, 2000. Variations from the winter average are estimated as

$$q(t_i) = \sigma^\circ(\phi_i, \mathbf{r}_i) - \sigma^\circ_i.$$

where i indicates the measurement index. The non-parametric estimation discussed in Section 5.1 is used to estimate q at 18:00 local time each day. For the threshold for Q-α melt detection I set $q_0 = 3$ dB. This corresponds to a layer of wet snow with 3.8 cm depth and $m_v = 1.0\%$.

ERS

Melt detection using ERS, termed E-α melt detection, is similar to the Q-α method and the method used by Wismann [14] to estimate melt using ERS. The differences between these methods are in the details of the data processing and the threshold selection.

ERS has a broad sampling in incidence angle (θ), so θ dependence is included in the σ° model such that

$$\begin{aligned} \sigma^\circ(\theta, \phi, \mathbf{r}) &= A + B_1(\theta - 40) + B_2(\theta - 40)^2 + s(\mathbf{r} \cdot \hat{\mathbf{g}}) \\ &\quad + M_1 \cos(\phi - \phi_1) + M_2 \cos(2\phi - \phi_2). \end{aligned}$$

The model parameters are estimated using ERS data from December 1, 1999 to February 28, 2000. Estimation and resampling of q is preformed using the same procedure as in Q-α, with the only difference being the inclusion of the incidence angle dependence and different non-parametric fit parameters as discussed in Section 5.1.

Since the frequency of ERS (5.3 GHz) is lower than that of QSCAT (13.4 GHz), the absorption by a layer of wet snow with the same depth is smaller. This results in a smaller threshold (q_0) for ERS than for QSCAT to give an equivalent melt definition. For ERS, a threshold with an equivalent melt definition to QSCAT is $q_0 = 1.0$ dB. This small threshold poses the problem of false alarms due to variance in the q estimates and other processes which effect the backscatter.

To avoid this false alarm problem and improve the consistency between Q-α and E-α, an empirical method is used to select a threshold to match QSCAT melt detection based on the maximum a posteriori (MAP) criteria. The MAP criteria is

$$\hat{m}(t) = \begin{cases} 1 \text{ if } p(q(t)|m = 1)p(m = 1) > p(q(t)|m = 0)p(m = 0) \\ 0 \text{ otherwise} \end{cases}.$$

where $\hat{m}(t)$ is the E-α melt estimate, $p(q|m)$ is the distribution of the E-α q given the true surface melt state, and $p(m)$ is the probability of melt or non-melt. The probabilities are estimated using the results of Q-α melt detection and are shown in
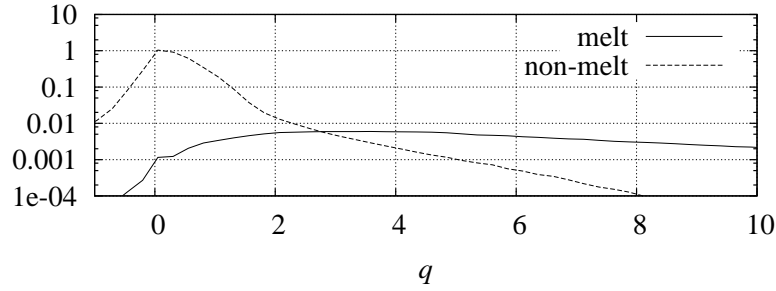
Figure 5.4: Normalized histogram of the ERS melt signal, q, for melt ($p(q|m = 1)p(m = 1)$) and non-melt ($p(q|m = 0)p(m = 0)$). The classification of melt or non-melt is based on the results of Q-α melt detection. The intersection of the two densities at 2.8 dB is the minimum error threshold for ERS melt detection based on the MAP criteria.

Fig. 5.4. The MAP threshold is at the intersection of the two densities at $q_0 = 2.8$ dB, which coincides with a theoretical wet layer depth of 10.8 cm.

The differences between the E-α method and the method of Wismann [14] are primarily in the data processing with a small difference also in the threshold value. The E-α method uses the long-term stability in the observation geometry dependencies to enable increased temporal resolution and mitigate the effects of azimuth dependence and co-location differences. This method results in increased temporal resolution and reduced variance compared with the processing method used by Wismann based on the results in Chapter 4. For further discussion about the two data processing methods refer to Chapter 4. The threshold difference is small with $q_0 = 2.8$ dB for E-α compared with $q_0 = 3.0$ dB used by Wismann.

SSM/I

SSM/I T_b measurements have been used in various studies to detect melt over Greenland. Two methods are used in the melt detection inter-comparison and are discussed in detail later.

For α-based melt detection with SSM/I, I use the 19V channel. The 19.35 GHz frequency is chosen because it is the closest SSM/I frequency to that of QSCAT

104

and ERS. Vertical polarization is chosen to minimize the impact of layer interfaces as discussed in Section 5.2.

Based on Eq. (5.3), a melt is indicated by

$$T_b > \alpha T_b^{\text{dry}} + (1 - \alpha) T_{\text{wet}}$$

where the value of α is determined by the thickness of the wet snow layer. This detection can be written in terms of $q(t)$ and q_0 as

$$q(t) = \frac{T_b(t) - T_b^{\text{dry}}}{T_{\text{wet}} - T_b^{\text{dry}}}$$

and $q_0 = 1 - \alpha$.

Melt detection requires an estimate of T_{wet} and T_b^{dry}. The wet snow-pack is assumed to be approximately at melting temperature ($T_{\text{wet}} \approx 273$ K) which is expected to be slightly high at melt onset. A precise estimate of T_b^{dry} is difficult to obtain. This is primarily due to the variability and uncertainty in the snow temperature throughout the year. For the purpose of simplicity, in this application T_b^{dry} is estimated as the average T_b from December 1 to February 28 during the previous winter at each location. This is expected to be reasonably close to T_b^{dry} although biased low.

Due to the uncertainties in the estimation of T_b^{dry} I use an empirical method to obtain an estimate of q_0, which is similar to the method used for ERS. Figure 5.5 shows the histogram of SSM/I q values for melt and non-melt based on the results from the Q-α melt detection. Based on the MAP criteria $q_0 = 0.46$, the intersection of the two histograms. This threshold is equivalent to a theoretical wet snow layer depth of 4.7 cm.

5.3.2 T_b-M

Another method using the SSM/I 19V channel, termed the T_b-M method, originates from Mote et al. [11]. Based on this method, a rise in T_b to over 31 K above winter mean T_b indicates melt. Interpreting the winter mean T_b as an estimate of T_b^{dry} as in the previous method, a melt is indicated by

$$T_b > T_b^{\text{dry}} + 31.$$
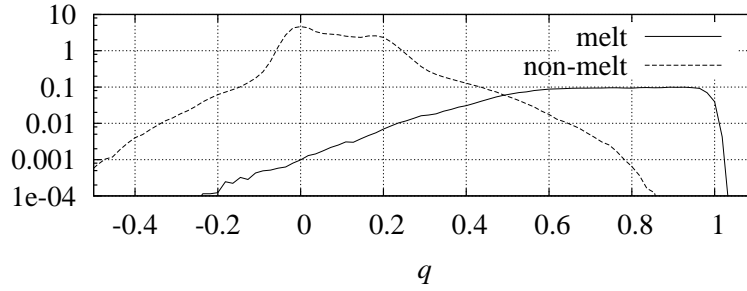
Figure 5.5: Normalized histogram of the SSM/I melt signal q for melt and non-melt. The classification as melt or non-melt is based on melt detection results from the Q-α method. The intersection of the two densities at 0.46 represents the minimum error threshold for SSM/I melt detection based on the MAP criteria.

The corresponding definitions for $q(t)$ and q_0 are

$$q(t) = T_b(t) - T_b^{\text{dry}}$$

and $q_0 = 31$ K. Just as in the previous method, T_b^{dry} is estimated the mean T_b between December 1, 1999 and February 28, 2000 at each location.

5.3.3 XPGR

The other T_b method for comparison uses the cross-gradient polarization ratio (XPGR) from Abdalati and Steffen [2, 4, 5, 13]. This method employs the differences between the SSM/I 19H and 37V channels to detect melt. For this method,

$$q(t) = \text{XPGR} = \frac{T_b^{19\text{H}}(t) - T_b^{37\text{V}}(t)}{T_b^{19\text{H}}(t) + T_b^{37\text{V}}(t)}$$

and $q_0 = -0.0158$ [2]. An equivalent criterion is if the observed ratio $T_b(19\text{H})/T_b(37\text{V})$ is greater than the constant value $(1 + q_0)/(1 - q_0)$ the surface flagged as melting. Based on the Rayleigh-Jeans approximation ($T_b = eT$), the temperature cancels and this criterion becomes a threshold on the ratio of the emissivity at the two frequencies and polarizations. A significant advantage of this method is that a single threshold is valid across the ice sheet.

106

5.3.4 Q-DV

The final method for comparison is based on the diurnal variation in σ° observed by QSCAT [15]. This is termed the Q-DV method. The melt criteria for Q-DV is that a diurnal change greater than 1.8 dB indicates melt. To determine the diurnal variation, estimates of σ° at 6:00 and 18:00 local time for QSCAT are used. In terms of $q(t)$ and q_0, this method is

$$q(t) = |\sigma^\circ_{18:00}(t) - \sigma^\circ_{6:00}(t)|$$

where t is constrained to be discrete at one day sampling and $q_0 = 1.8$ dB. This method is not used with ERS because of inadequate temporal resolution.

5.4 Method Comparison

These six methods are compared based on the detected melt for each day during the year 2000. Metrics for this comparison include total melt ($\mathcal{M}$), melt extent (E), and daily melt extent (ξ). The method differences are illustrated using images of the melt duration, melt extent, and temporal variation.

The total melt and the melt extent detected by each method are listed in Table 5.2. The total melt is given by

$$\mathcal{M} = a \sum_{t=1}^{365} \sum_{i=1}^{N} m_i(d)$$

where a is the area of a single pixel, t is the Julian Day, i is the pixel index, N is the total number of pixels. The three α-based methods and the T_b-M method result in similar estimates of $\mathcal{M}$, approximately double that of the Q-DV and XPGR methods. The two QSCAT methods result in the extremes in the total melt detection with the Q-α method detecting the largest amount and the Q-DV method detecting the smallest.

The melt extent,

$$E = a \sum_{i=1}^{N} \max_t m_i(t),$$

is consistent between the methods with the exception of XPGR which detects just over half of the melt area of the others and E-α which detects about 80% of the areal

107

Table 5.2: Total melt (km^2 days x10^6) and melt extent (km^{2}x10^4) detected by the different methods for 2000. The bottom row lists the percent of the ice sheet the melt extent covers.

	Q-α	E-α	T_b-α	T_b-M	XPGR	Q-DV
total melt ($\mathcal{M}$)	30.3	27.5	29.3	27.3	14.6	12.2
melt extent (E)	95.9	78.7	102.5	99.2	52.9	97.2
percent	58	48	62	60	32	59

melt extent of the others. To determine the percentage of the ice-sheet experiencing melt, the melt extent is divided by the total area within the ice-sheet mask. Four of the six methods estimate that about 60% of the ice sheet experiences melt. This is consistent with the estimated dry snow extent from Benson [30]. The dry snow boundary approximated by Benson is the intersection between and plane sloping down 1.15 km to the north and the elevation of the ice sheet where the intersection at 70° N is at 3000 m. With the ice-sheet mask used herein, this corresponds to 60% of the ice-sheet experiencing melt in a typical year.

Additional insights into the differences between the individual methods are gained by comparing the variation in daily estimates of the daily melt extent

$$\xi(t) = \sum_{i=1}^{N} m_i(t).$$

The variations in $\xi(t)$ for the different methods are shown in Fig. 5.6. The T_b-α and T_b-M methods give consistent estimates of $\xi(t)$. The XPGR method is biased low during periods of melt onset and peak melt. XPGR indicates very little melt around JD 213 when the other methods detect the maximum melt extent. During the refreeze period (after JD 235), XPGR exceeds the estimated melt extent of the other methods.

For the $\sigma°$ methods, E-α and Q-α result in similar $\xi(t)$ estimates with the E-α method having a small negative bias at melt onset and peak melt times, and a small positive bias during the refreeze period. Q-DV is consistently biased low,
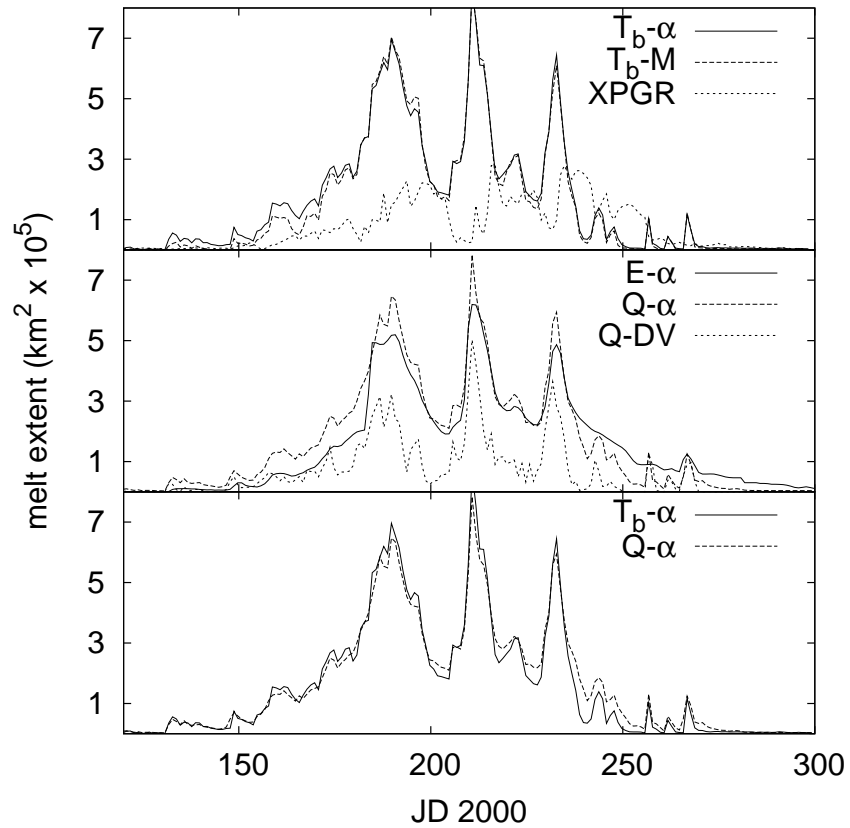
Figure 5.6: Melt extent each day as observed by the different methods. The top plot shows comparison between T_b methods, the middle plot shows comparisons between σ° methods, and the bottom plot shows the comparison between a single T_b and single σ° method.

estimating approximately 50% of the melt area of other methods. The peaks in the Q-DV $\xi(t)$ estimates occur just prior to the peaks in the other methods.

Direct comparison between the $\xi(t)$ estimates from the T_b-α and Q-α methods shows very close agreement. The small difference between the two is a larger estimate of the melt extent from T_b-α during melt onset and a larger extent estimate by Q-α during periods of refreeze. This is attributed to a difference in the sensitivity to melt due to the frequency difference which is discussed in Section 5.4.1.

Figure 5.7 includes images illustrating the annual melt extent, the annual melt duration, and the temporal/spatial variation of the detected melt for summer 2000. The melt duration for each method is illustrated by comparing the melt duration estimated by each individual method with the average melt duration estimated by the α-based methods. The melt duration detected by the Q-α method is near average over the complete melt extent. E-α estimates of the duration are above average in regions with a long average melt duration. T_b-α melt duration estimates are below average in the same regions. The difference between the T_b-M melt duration estimates and the α-based average varies by region. A general trend is observed of above average estimates in areas with low winter T_b values and below average estimates in regions with high winter T_b values (see Fig. 5.2 for a winter T_b image).

In general, XPGR and Q-DV detect shorter melt than the α-based methods. For Q-DV this is only true for lower elevations: at higher elevations the melt duration is very close to the estimates of the α-based methods. With XPGR exceptions exist on the east of the ice sheet around 64° N and 77° N where XPGR detects longer melt than the α-based methods.

The middle row of images in Fig. 5.7 shows a comparison between the melt extent obtained from the individual methods and the melt extent obtained by combining the methods. Just as indicated in Table 5.2, the Q-α, T_b-α, T_b-M, and Q-DV methods agree closely on the extent of the melt. Differences are primarily on the border of the dry snow zone and are attributed to small differences in the definition of melt intrinsic to each method. For E-α and XPGR the areas of missed detection

110
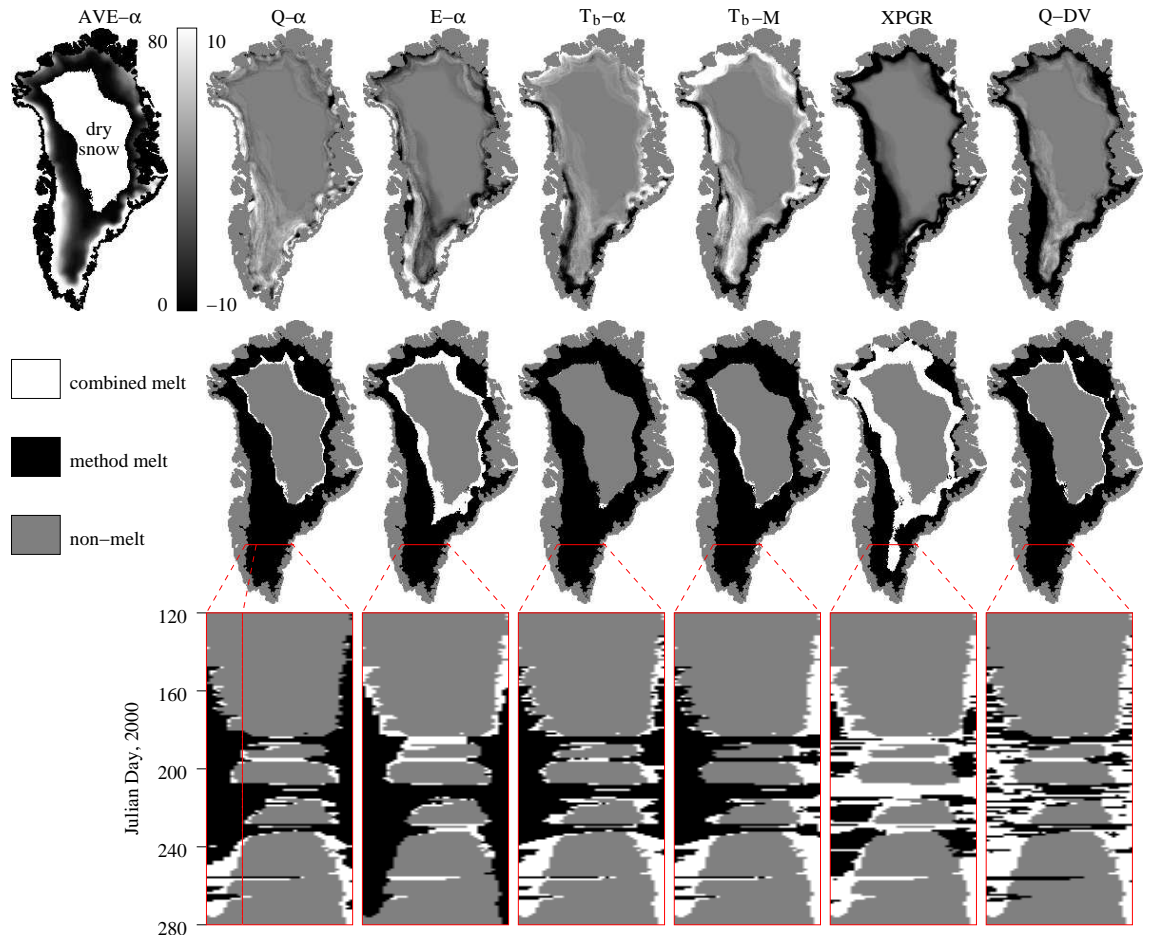
Figure 5.7: Top row: (left) Average melt duration in days obtained from the α-based methods. (right) Images of the difference between each method and the α-based average. Middle row: Annual melt extent from the individual methods compared with the annual melt extent combining all methods. Bottom row: Hovmöller diagrams showing the variation in the melt extent over time along a transect across the southern portion of the ice-sheet as indicated in the figure. In the bottom two rows white represents the area that is designated as melting by any method. Black is imposed over the white to indicate the melt area detected by the method specified in the column header. Gray is non-melt area. The line over the Q-α Hovmöller diagram indicates the location for the Q versus t plots in Fig. 5.9. See Fig 5.8 for enlarged images.
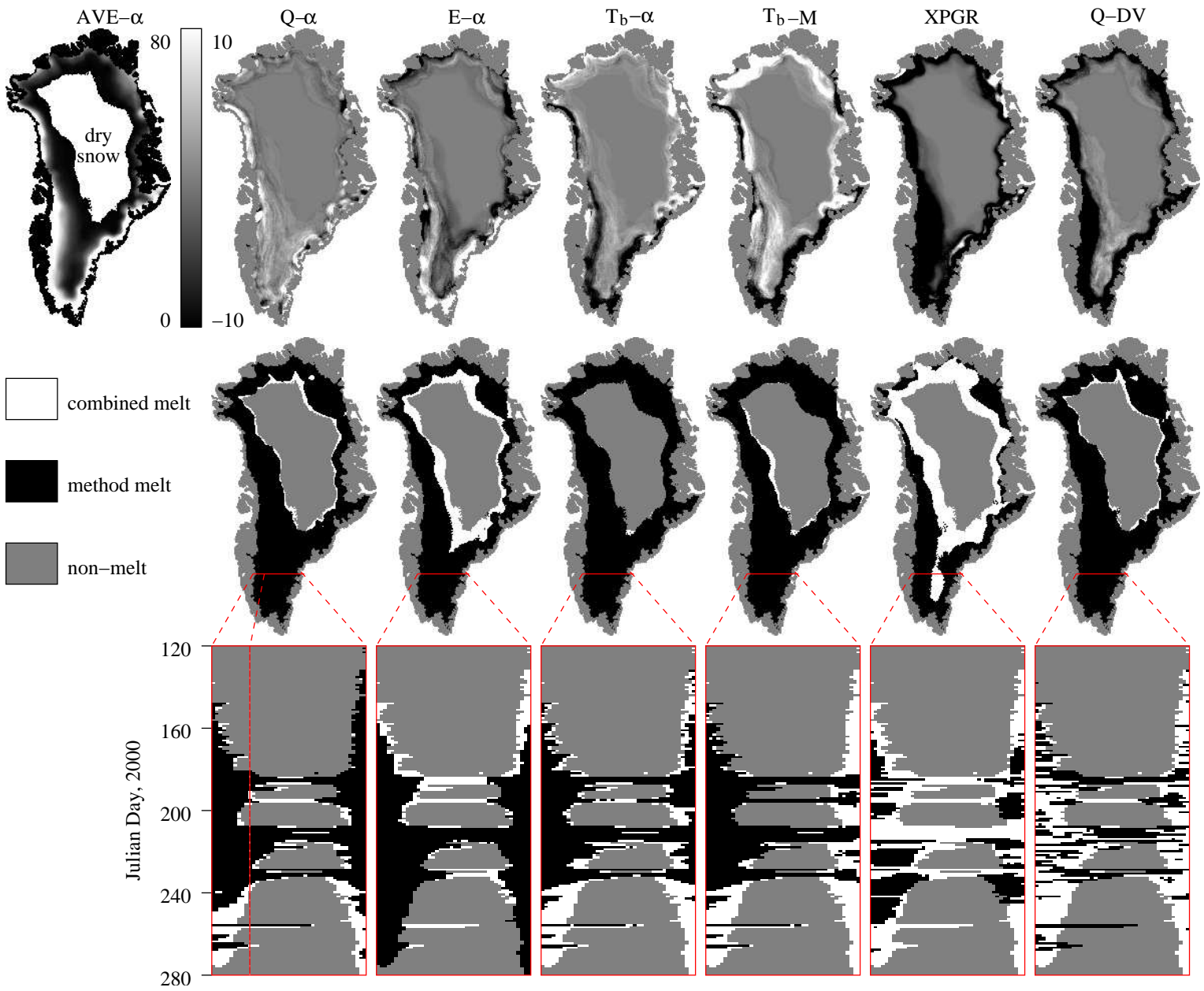
Figure 5.8: Enlarged version of Fig. 5.7.

are in the upper regions of the percolation zone indicating that these methods are less sensitive to small amounts of melt.

The bottom row in Fig. 5.7 is a set of Hovmöller diagrams which illustrates the changes in the melt extent over time along a transect across the southern portion of the ice-sheet. These images aid in understanding the spatial and temporal consistency in the melt detection methods.

The α-based methods all appear to be spatial and temporally consistent with expected trends in the summer melt process. Melt, as a function of time, begins at the edges and progresses toward the interior of the ice sheet. Increases and decreases in the melt extent occur gradually over time. Near the peak melt period, where the upper extent of the melt is near the crest of the ice-sheet, the changes in the melt extent occur more rapidly. This increased rate of change in melt area is attributed to the small slope of the ice-sheet near the crest resulting in large changes in the areal extent of the melt due to small changes in temperature. It appears that a warm front moved across the ice-sheet near JD 255 which caused a short melt event. This is detected by the Q-α and T_b-α methods, but not by the E-α method. The missed detection by E-α is attributed to the lower temporal resolution of the ERS data and to the ERS local time sampling. The temporal resolution of ERS, along with the differences in melt detection by the α-based methods, are discussed in Section 5.4.1.

The Hovmöller diagram for the T_b-M method is similar on the west of the ice sheet to those for the α-based methods. The melt detected by T_b-M and T_b-α is almost identical with T_b-M detecting the upper extent of the melt about 10 to 20 km further upslope. On the east however, there is a notable difference: the T_b-M method detects less melt than the α-based methods, and melt is only detected during intense melt periods.

Substantial differences are also observed in the Hovmöller diagrams between XPGR and the other melt detection methods. These differences are largest during periods of intense melt based on the results of the α-based and T_b-M methods.

An example is observed near JD 213, a time when other methods are detecting maximum melt. The XPGR Hovmöller diagram indicates no melt at this time; however, previous to, and after this period, XPGR detects a sizable amount of melt. XPGR also results in short periods of detection of melt at higher elevations while not detecting melt at lower elevations. An example of this is shown in the XPGR Hovmöller diagram near JD 235.

Although the maximum melt extent estimates from Q-DV closely match that of other methods, the daily variation in the melt extent detected by Q-DV is very different from that of any other method. Melt detection appears sporadic in both time and space. Melt detection by Q-DV is not accepted as accurate based primarily on the lack of spatial and temporal correlation, making this method inconsistent with the results of the other methods and inconsistent with what is expected for the natural melt progress.

To further illustrate the similarities and differences between the melt detection methods, Fig. 5.9 displays $q(t)$ and q_0 for each method at one location. Melt onset is indicated in each plot by an abrupt large increase in $q(t)$. During the melt period, the $q(t)$ signal of the α-based methods and T_b-M are similar. The E-α signal lacks some of the higher frequency components of the other methods due to coarser temporal resolution in the ERS data. The variation in the T_b-α and T_b-M $q(t)$ during non-melt is attributed to temperature variation and accumulation. The XPGR and Q-DV melt signals are substantially different from the other methods. With XPGR, local maximums in $q(t)$ occur at times similar to those observed for the α-based and T_b-M methods; however, the relative amplitude of the peaks are different contributing to discrepancies in the melt detection by XPGR and the other methods. During the melt period, the Q-DV melt signal is much more variable than the other methods. During non-melt, $q(t)$ remains relatively constant for both XPGR and Q-DV.

To evaluate the agreement between the methods on the location and time of melt, the correlation coefficient is used which is defined as

$$R = \frac{S_{xy}}{\sqrt{S_{xx}S_{yy}}}.$$
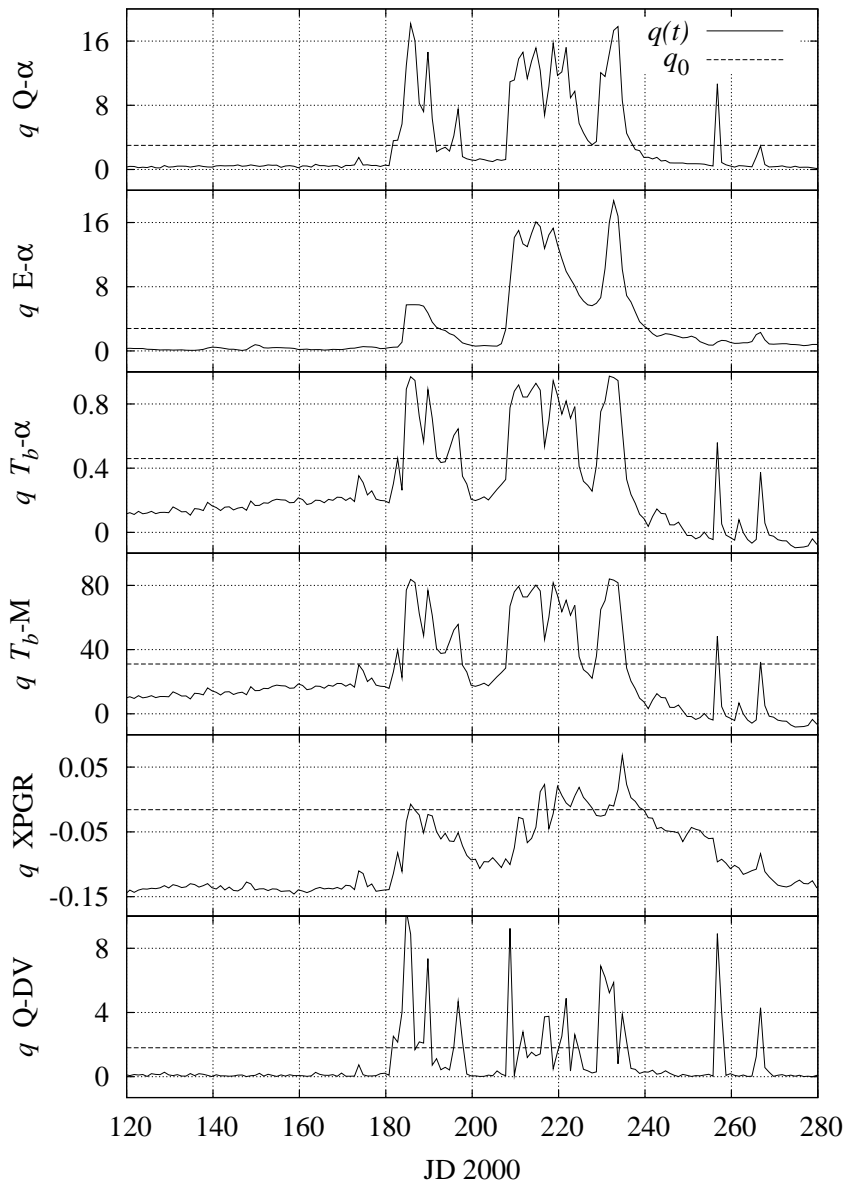
Figure 5.9: Plots of the melt signal $(q(t))$ for the different melt detection methods at 64.9 N, 47.3 W. The location is indicated in the Q-α Hovmöller diagram in Fig. 5.7.

Table 5.3: Correlation coefficient (R) between the melt signal ($m_p(d)$) of the various methods.

	Q-α	E-α	T_b-α	T_b-M	XPGR	Q-DV
Q-α	1.00	0.81	0.87	0.78	0.42	0.57
E-α	0.81	1.00	0.73	0.67	0.49	0.44
T_b-α	0.87	0.73	1.00	0.85	0.38	0.55
T_b-M	0.78	0.67	0.85	1.00	0.35	0.54
XPGR	0.42	0.49	0.38	0.35	1.00	0.19
Q-DV	0.57	0.44	0.55	0.54	0.19	1.00

where

$$S_{xy} = \sum_{i=1}^{N}(x_i - \bar{x})(y_i - \bar{y}).$$

The average of x_i is $\bar{x}$ and the average of y_i is $\bar{y}$. In this case, the x_i or y_i is the melt signal for all pixels ($m_i(t) \, \forall \, i, t$) based on the different methods. The correlation coefficients are listed in Table 5.3.

The correlation between the α-based methods is high, between 0.73 and 0.87, indicating that these methods are consistent in time and location of detected melt. The T_b-M method is also strongly correlated to the α-based methods. XPGR and Q-DV have lower correlations with the other methods, with correlation to the α-based methods ranging from 0.38 to 0.57. The latter two methods also exhibit little correlation with each other having a joint correlation coefficient of only 0.19.

5.4.1 Discussion

The differences in the melt detected by the individual methods are attributed to differences in sensitivity to melt due to frequency and/or differences in the definition of melt implicit with each method.

The α-based methods define a melt event based on a uniform wet snow layer with a specified m_v and minimum depth. This property contributes to the spatial and temporal consistency of these methods. It also helps to ensure consistency in the different facies and regions of the ice-sheet. Given a value of α associated with

116
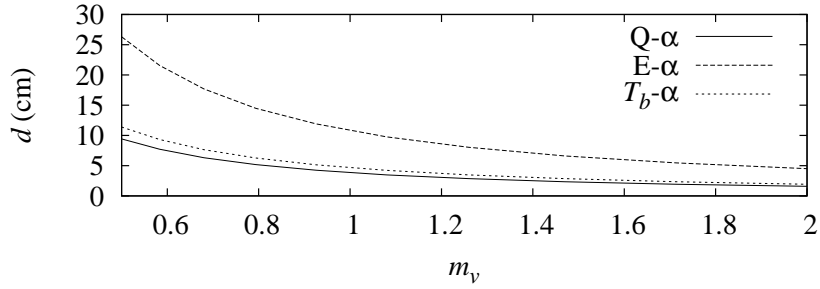
Figure 5.10: Wet snow percent liquid moisture content (m_v) versus depth (d) corresponding to the melt threshold used in the Q-α, E-α, and T_b-α melt detection methods. The lines are calculated based on a snow density of $\rho = 0.4$ g/cm^3.

a threshold, a line can be drawn indicating the relationship between m_v and d for melt detection. These lines are shown in Fig. 5.10 for the three α-based methods. The thresholds for Q-α and T_b-α are similar with the small difference representative of the uncertainty in the T_b^{dry} estimates. The E-α minimum wet snow depth for melt detection is about double that of Q-α and T_b-α for any given value of m_v. Because the 5.3 GHz ERS measurements are less sensitive to snow moisture content, a larger threshold is necessary to reduce the possibility of false alarms due to noise. Thus, E-α requires a more intense melt before detection occurs. This contributes to E-α generally detecting less melt than the Q-α and T_b-α methods.

Another factor affecting E-α melt detection is the local time of day of the ERS samples. The peak ERS sampling is around 11:30 and 21:30 local time (see Fig. 5.1) which is before and after the expected period of peak diurnal melt. This is also expected to reduce the melt detected using E-α.

The discussion thus far has focused primarily on differences in detecting melt at onset, which is the focus of of the α-based melt detection. During refreeze the vertical melt profile can be quite different than that of the simple physical model presented. After an intense melt event, subsurface liquid moisture remains after the refreezing of the surface. Due to the large penetration depth at low frequencies, melt is still detected after surface refreeze. The lingering melt detection after intense melt

is observed in the results from E-α in the melt extent plot in Fig. 5.6 and the the E-α Hovmöller diagram in Fig. 5.7. This is also observed in comparing the Q-α results to those of T_b-α in the same figures.

T_b-M is the non-α method with results most similar to the α-based methods. Melt detection using T_b-M is based on the winter T_b statistics and melt T_b statistics at selected locations with the threshold based on the difference between the winter mean T_b and the mean T_b during a melt period as well as the standard deviation of T_b during the melt period [11]. Over much of the ice-sheet this method performs very well. However, at locations which have a high winter mean T_b values, this method significantly under-detects the melt. This under-detection can be explained using the simple melt model: In southwest Greenland the mean winter T_b is ≈ 195 K. This results in melt detection for T_b-M when $T_b > 226$ K. The corresponding T_b-α physical model parameters are $\alpha = 0.60$, and $d = 3.8$ cm based on $m_v = 1.0\%$. In the southeast, the winter mean T_b is ≈ 230 K resulting in T_b-M melt detection when $T_b > 261$ K. The corresponding T_b-α physical model parameters here are $\alpha = 0.28$ and $d = 9.6$ cm based on $m_v = 1.0\%$. Note the difference in the theoretical depth of the wet snow layer associated with the melt detection threshold at the two locations. This theoretical difference wet snow depth is further accentuated by the low bias in the T_b^{dry} estimate, making the true difference even greater. Hence, T_b-M results in different melt definitions at different locations with an end result of higher sensitivity to melt in the southwest of the ice-sheet than in the southeast. Effects of this regional difference are observed in the limited detection of melt on the east of the ice-sheet in T_b-M melt duration image and the Hovmöller diagram in Fig. 5.7. The cold region bias (more melt detected at a cold locations than a warm location), which was also observed by Abdalati and Steffen [5], is attributed to this effect.

The Q-DV method is based on the rapid fluctuation of σ° during a melt event. Because of freezing at night and melting during the day it is assumed that there is a large fluctuation in σ° over the course of a day. The main caveat of this method is that it is based on a sufficient, but not a necessary condition. A diurnal change of over 1.8 dB over snow is indicative of melt; however, the converse is not

true. The surface can theoretically be melting and have negligible diurnal variation. This is observed in the Q-DV Hovmöller diagram in Fig. 5.7 where long periods of melt based on results of other methods are interspersed with intermittent gaps of undetected melt in the Q-DV results.

The XPGR method is based on 19 GHz signal being more responsive to melt onset in the firn than 37 GHz and a melt producing a larger increase in the H-pol emissivity than V-pol [2]. However, it appears that significant melt can occur without meeting the XPGR melt detection requirement. An example is observed around JD 213 when the other methods detect maximum melt extent, and XPGR detects minimal melt. One attribute of XPGR is that due to the difference in the penetration depths of the two channels it detects melt after the surface has refrozen if the subsurface remains contains liquid moisture [2].

5.5 Summary and Conclusions

Melt detection using σ° and T_b is related to snow wetness and the depth of the wet snow layer at melt onset using a simple physical model. The technique for melt detection using σ° reduces to using a set threshold below the winter mean. I use a threshold of 3 dB for QSCAT and 2.8 dB for ERS. Model based melt detection using T_b is only slightly more complex. A melt is indicated by a rise in T_b above some threshold which is a function of the difference between the winter mean T_b and the maximum T_b for wet snow (273 K). The selected threshold is 46% of this difference added to the winter mean T_b. The threshold for QSCAT corresponds to a theoretical wet snow layer with $m_v = 1.0\%$ and depth $d = 3.8$ cm. An empircal method based on MAP detection and the QSCAT melt detection was used to select the ERS and SSM/I thresholds. The theoretical wet snow depths corresponding to the empirically obtained thresholds are $d = 10.8$ cm for ERS and $d = 4.7$ cm for SSM/I 19V.

Melt detection based on this simple physical model, which is termed α-based detection, eliminates unnatural phenomenon observed in the results for other melt detection methods. Improvements include similar melt duration estimates for

similar elevations on the east and west sides of the ice sheet, elimination of mid-summer melt detection gaps between periods of intense melt, and the detection of melt at lower elevations before, during, and after detection of melt at higher elevations.

Some differences are observed in α-based melt detection for the three sensors. The E-α method is the most dissimilar detecting a total melt extent of 48% of the ice sheet compared with 58% for Q-α and 62% for T_b-α. This difference is attributed to lower temporal resolution, reduced sensitivity to melt due to the lower frequency, and different local time of day sampling for ERS compared with QSCAT and SSM/I. The E-α method also detects above average melt during the refreeze period. This is attributed to the relatively large penetration depth at C-band making the measurements sensitive to the presence of subsurface melt remaining after surface refreeze. This phenomenon of extended melt detection is observed to a smaller degree in QSCAT melt detection when compared with SSM/I which is also attributed to difference in penetration depth due to the frequency difference between the two instruments.

The results for non-α methods are widely variable. Estimates of the melt extent are near 60% of the ice-sheet for T_b-M and Q-DV, which is similar to the Q-α and T_b-α results. XPGR, however, indicates that only 32% of the ice-sheet experiences melt during the summer of 2004. The non-α methods are also generally less correlated with other methods with the lowest correlation $R = 0.19$ between XPGR and Q-DV.

The α-based melt detection is based on a model for melt onset. However, during refreeze the vertical melt profile is potentially quite different from the profile at melt onset. This is especially true in regions with extended melt duration. Although the α-based method performs moderately well at determining refreeze, the relationship between the end of the detected melt and the surface profile are not as well understood as at melt onset. This phenomenon is one reason for the differences between the α-based methods during the refreeze period. Ways to improve the characterization of the surface during the refreeze process are discussed in the next chapter.

In situ measurements of the vertical wetness profile of the surface would aid in further validating the α-based melt detection. Simultaneous measurements from scatterometer and radiometer instruments aboard the same platform will further enhance the ability to inter-relate T_b and σ° melt detection. This is the setup with SeaWinds and AMSR on ADEOS II.

Chapter 6

Melt Classification

As discussed in the previous chapter, various methods have been developed for using microwave measurements to detect melt on the Greenland ice sheet. The methods generally focus on detecting the presence of liquid water in the snow. However, a snow-surface containing liquid water can be in two states: melt or freeze. When the amount of liquid water in the snow-pack is increasing over time, the net heat flow is into to snow and the snow is in the melt state. If the liquid water is decreasing, the net heat flow is out of the wet snow so the snow is classified as freezing. In this generalization, changes in the liquid water content due to percolation are ignored for simplification. The distinction between the melt and freeze stages of the melt cycle is important because ablation occurs when heat is flowing into the snow causing liquid water to form. Minimal ablation is expected during periods when heat is flowing out from the surface and liquid water is transforming back to its frozen state.

Increased accuracy in ablation estimation requires differentiation between the melt and freeze stages of the melt cycle. This differentiation is possible based on fundamental differences due frequency and polarization in the sensitivity of T_b to snow melt. These differences are observed using SSM/I channel ratios. The relationship between the channel ratios and the melt cycle stages are established through empirical observations and supported by basic microwave emission modeling. The results in this paper lay a framework for the discrimination between the melt and freeze stages of the melt cycle.

This chapter is organized as follows. First, a background discussion on the data set and the data processing method is presented. Then, diurnal signatures of T_b are analyzed and compared with automatic weather station temperature measurements. Next, diurnal variations in SSM/I channel ratios are related to the stages of melt, which is supported by *in situ* data from other investigators. Finally, theory supporting this method for melt classification is presented.

6.1 Data

The focus of this chapter is on the differentiation between the different stages of the melt cycle. Because the surface experiences multiple stages of the melt cycle during one day intervals, the daily average T_b values used in other studies are inadequate in their temporal sampling. In order to achieve increased temporal resolution, I use a non-parametric estimator in conjunction with T_b measurements from multiple instruments.

During the summer of 2002 three SSM/I instruments operated simultaneously aboard the F-13, F-14, and F-15 satellites. Their orbits result in different time-of-day observations for each instrument. Combining measurements from the three instruments provides increased temporal coverage. This coverage varies with latitude. Image histograms showing the distribution of the local time of day of the T_b samples for Greenland latitudes are shown in Fig. 6.1 (a). At high latitudes, each sensor covers a continuous 11 hour span of time with a combined span of approximately 14 hours of continuous coverage. At lower latitudes, there is a temporal division between ascending and descending measurements. The combined coverage is approximately from 0600 to 1200 in the morning and 1600 to 2200 in the evening. Because of relative orbital geometries between the three SSM/I sensors, an eight hour portion (2200-0600) of each day is not observed at any latitude. Note that SSM/I measurements occur primarily during mid-day when the largest amount of melt is expected to occur.

T_b measurements are processed to estimate T_b at regularly spaced increments in space and time. The spatial sampling is 8.9 km, and the temporal sampling

124

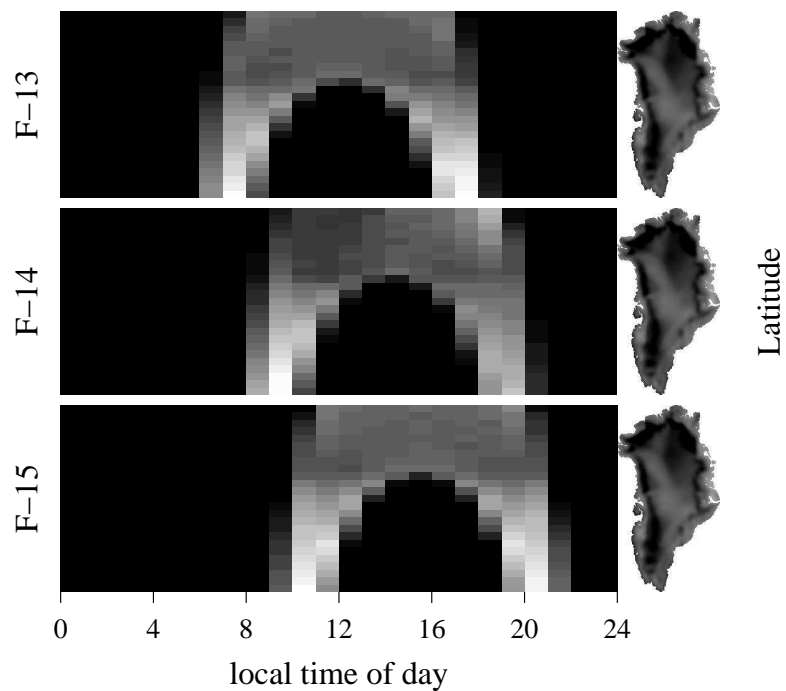Figure 6.1: Image histograms of the pass times of the F-13, F-14, and F-15 satellites versus latitude. Each horizontal scan represents a histogram at the matching latitude on the Greenland image on the right. At high latitudes temporal coverage is one continuous span due to the wide swath orbit inclination angle of the satellites. At lower latitudes the measurements are divided into ascending and descending passes.

is 3 hours where T_b is interpolated to obtain estimates at times of day when there are no measurements. For a given location, T_b measurements within a 25 km radius are included in the processing. Estimates of T_b every three hours are obtained using a simple non-parametric fit to the data where the estimate of T_b at time τ is

$$T_b(t) = \frac{\sum_i T_{bi} w(\tau, t_i)}{\sum_i w(\tau, t_i)}$$

where

$$w(\tau, t_i) = e^{-\frac{1}{2}\frac{(t_i - \tau)^2}{\sigma_t^2}}$$

is a temporal weighting factor and $\sigma_t = 3$ hours, which is the same as the sampling interval. The sampling frequency of these estimates makes it possible to observe the stages of the daily melt cycle and aids in associating the frequency and polarization sensitivities of T_b with the vertical melt profile.

A study site centered at 78.0 N, 34.0 W is selected for three primary reasons. First, it is the location of the Tunu-N automatic weather station (AWS), so air temperature measurements are available. Second, moderate melt is observed in this area during the summer of 2002. Third, no major gaps in the temporal coverage exists for T_b or AWS temperature over the time interval.

6.2 T_b Daily Melt Cycle Observations

The sensitivity of radiometers to snow melt stems from the dramatic effect the presence of liquid water has on the microwave properties of the snow. The Rayleigh-Jeans approximation is

$$T_b = eT$$

where e is the microwave emissivity and T is the physical temperature of the snow in Kelvin [2]. The emissivity remains relatively constant over time for frozen snow, making T_b approximately a linear function of T. When melt begins, the introduction of liquid water into the snow-pack causes a large increase in e and a corresponding increase in T_b. This is illustrated in the summer T_b image of Fig. 6.2 where the periphery of the Greenland ice sheet exhibits high T_b values. In this image the melt is particularly strong in northeast Greenland.
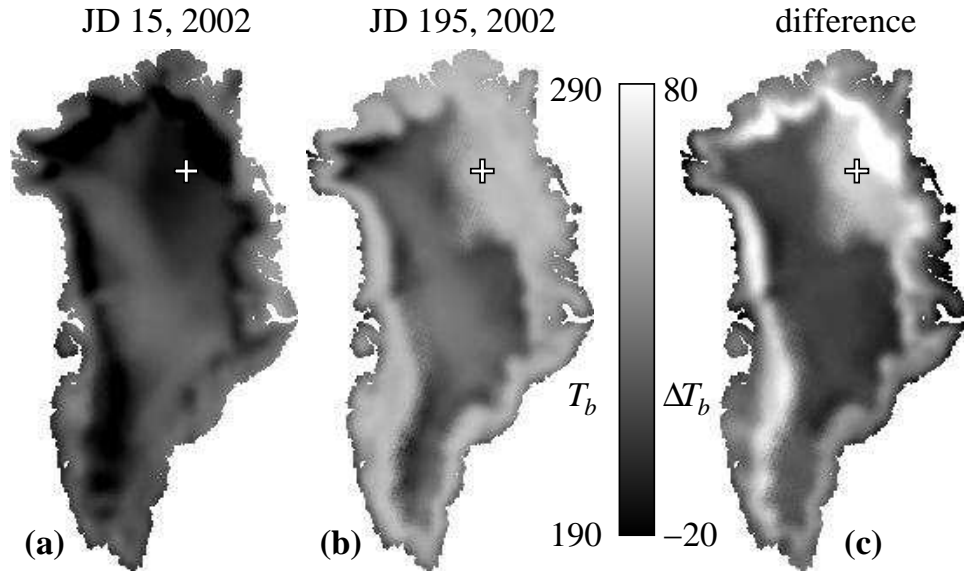
Figure 6.2: Greenland SSM/I 19V T_b images from (a) mid-winter (JD 15, 2002) and (b) the peak melt period (JD 195, 2002). The difference is shown in (c). The large differences are primarily caused by the presence of liquid water in the snow from melt. Smaller differences are due to surface temperature change. The Tunu-N site (78 N, 34 W) is indicated by a "+" mark.

Using the high temporal resolution T_b estimates it is possible to observe changes in T_b related to the stages of the daily melt cycle. This is illustrated using T_b estimates centered at the Tunu-N site. An abrupt increase in T_b connected with a melt event is observed in Fig. 6.3 during the afternoon of JD 189. By early in the morning on JD 190, T_b has dropped significantly due to overnight freezing. By mid-day on JD 190, the T_b measurements are once again at high values. This pattern of daily melt and nightly freeze is observed each day in the T_b variation. The diurnal variation is due to both temperature cycling and changes in emissivity with the emissivity change dominating during periods of melt/refreeze. The high average of the T_b measurements between JD 190-195 indicates relatively intense melt. T_b gradually decreases during the period between JD 196 and 200 indicating a gentle refreeze. The increased spread in the raw data during this period is attributed to spatial inhomogeneities in the refreeze process.

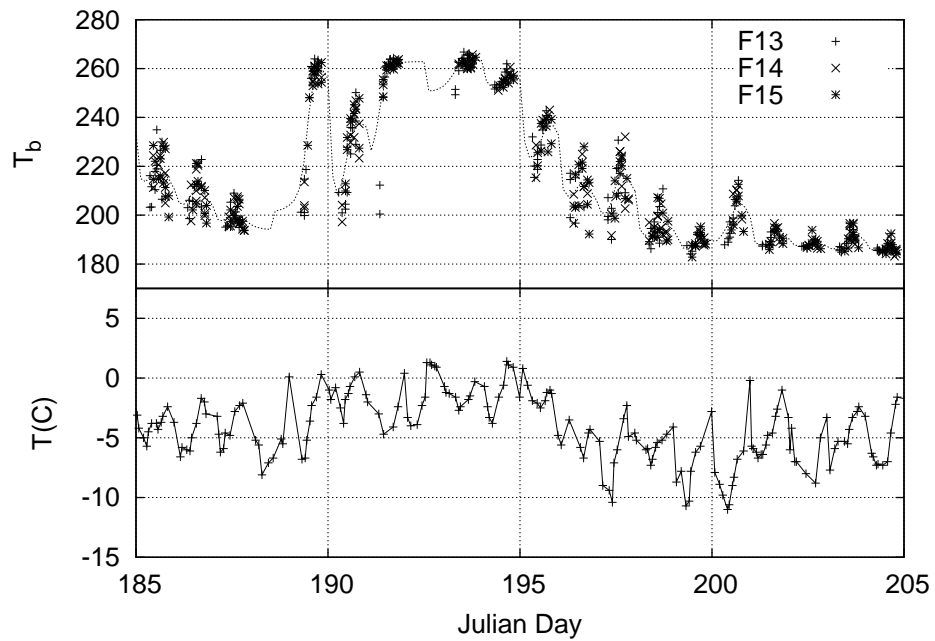Figure 6.3:   Raw 19V T_b measurements from 78.0 N, 34.0 W during the summer of 2002. The line is a non-parametric fit to the raw data with estimates of T_b at 3 hour intervals. The bottom plot displays AWS near-surface air temperature measurements at the same location. The horizontal axis is local Greenland time.

Automatic weather station (AWS) near-surface air temperature measurements obtained from the Greenland Climate Network are used to assist in validating melt as the primary contributing factor driving the rapid large fluctuations of the microwave measurements. The AWS Temperature data (T_{air}) concurs with the microwave data set in manifesting periods of melt. The days when T_{air} reaches above freezing (JD 190-196) is when the T_b measurements indicate significant melt. After JD 196, T_{air} remains below freezing and the microwave measurements gently migrate to their frozen state.

Figure 6.4 illustrates the strong relationship between the microwave measurements and T_{air}. The effects of melt are observed in the 19V and 19H T_b measurements at T_{air} values as low as -10° C which is attributed to liquid water beginning to form on firn crystals. Above -2° C the effects of the melt on T_b saturate at around 260° K for 19V and 245° K for 19H. Slight differences in the sensitivity of the 19V and 19H channels aid in determining the melt profile. A key difference is illustrated using the 19H/19V polarization ratio (see Fig. 6.4). For $T_{air} < -10°$ K the polarization ratio is ≈ 0.82. As the temperature increases, the polarization ratio increases to ≈ 0.94 at $T_{air} = 0$. Further analysis of the 19 GHz polarization ratio is provided in the next section.

Some care is required in interpreting Fig. 6.4 due to discrepancies expected between T_{air} and the actual surface temperature. Surface temperature change is primarily driven by radiation and conduction whereas convection plays a major role in local air temperature change. This discrepancy is considered to be a contributing factor to the hysteresis effect observed in T_b as a function of T_{air} associated with a melt event. Also, the satellite pass times are during the day when the surface is generally melting, so night-time trends are not included.

6.3   Channel Ratios

An illustration of a simplified vertical melt cycle for this area is shown schematically in Fig. 6.5. During the melting phase, liquid water forms on the snow grains near the surface, with the depth of the melt increasing over time. During
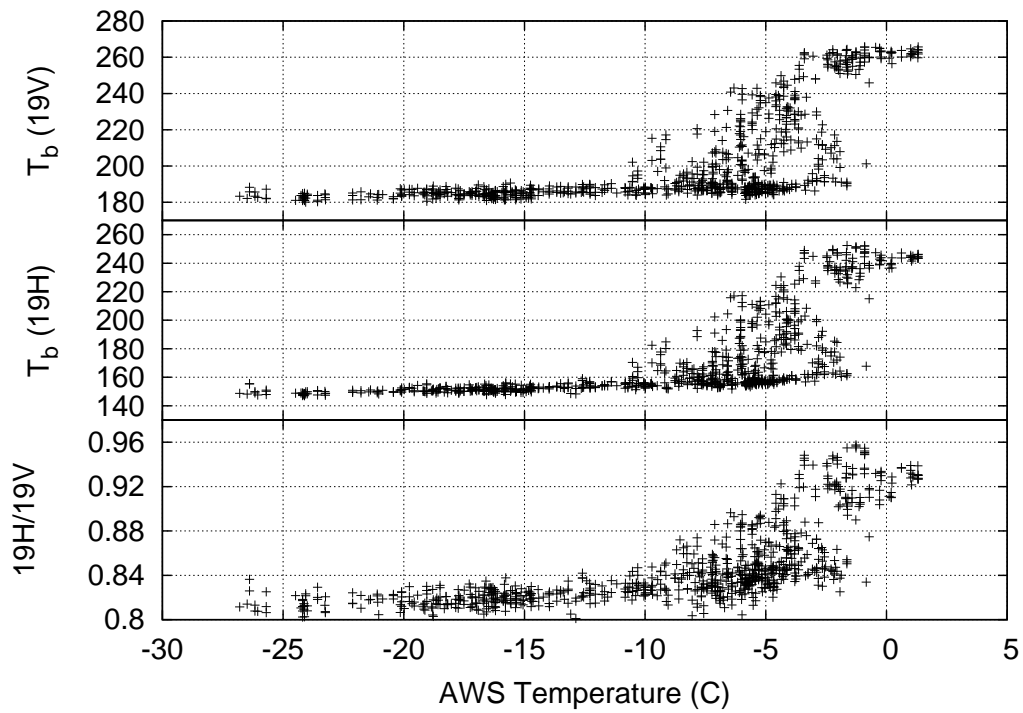
Figure 6.4: Scatter plots showing the relationship between T_{air} and 19V and 19H T_b values. Data from JD 184 to 236, 2002 are included with measurements from JD 205 to 211 discarded due to the lack of T_{air} measurements during this period. Data is from 78.0 N, 34.0 W.
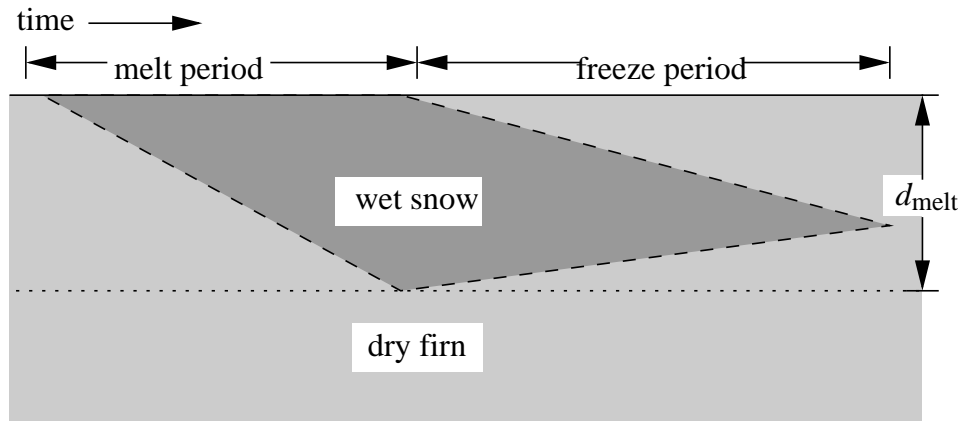
Figure 6.5: An illustration of the progression of a simplified vertical melt profile over time.

freeze, heat flows both up from the surface and down into the snow-pack. In the case of deep melt, the surface may freeze while liquid water remains in the subsurface snow. Multiple such situations with a frozen crust above wet snow were observed by Mätzler [50].

Both surface and subsurface melt contribute to a large effective emissivity resulting in high T_b measurements. However, different polarizations and frequencies respond slightly different to the stages of a melt event. Figure 6.6 shows various SSM/I channel ratios. The first and second plot from the top focus on frequency difference while the third and forth illustrate polarization dependence. The ratio method has the advantage of eliminating the change in surface temperature and focusing on only differences in emissivity for the two channels.

Variations in the frequency dependence of emissivity aid in detecting periods during which subsurface melt is present under a refrozen surface. The 19V/37V and 19H/37H plots in Fig. 6.6 are significantly higher during the period between JD 195 and 200 which is a refreezing period. During mid-day when surface melt is most likely, the frequency ratios decrease, migrating closer to one. This is attributed to the small emission depth of wet snow for both frequencies, so both channels are "seeing" only the wet surface layer. However, in dry or refrozen snow the emission depth at

Figure 6.6: Ratios of various non-parametric estimates of SSM/I channel brightness temperatures are valuable in characterizing the melt profile of the surface. Data is for the study location 78.0 N, 34.0 W.

Table 6.1: Definitions for the different snow types.

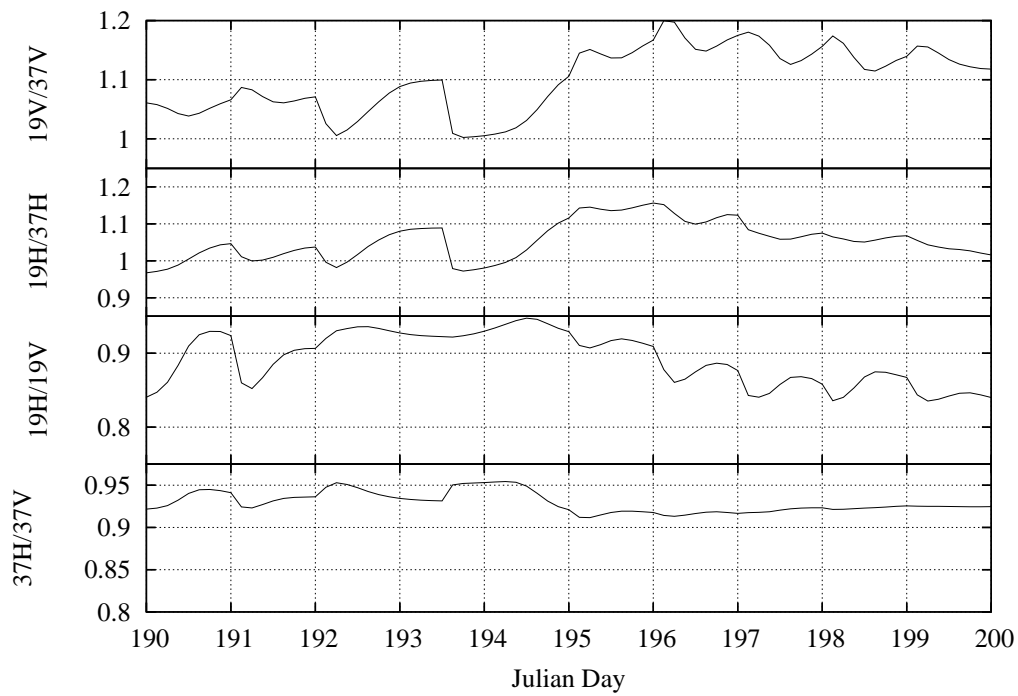| snow type	definition
deep dry snow	water equivalent of dry snow is between 25 and 63 cm
wet snow	snow surface layer is wet
thin crust	a frozen crust, 1 to 3 cm thick, over wet snow
thick crust	a frozen crust, 4 to 30 thick, over wet snow

37 GHz is significantly less than at 19 GHz. Thus, at 37 GHz the refrozen surface is a greater contributer to the signal than at 19 GHz so that the 37 GHz emissivity drops becoming more like that of refrozen snow while the 19 GHz emissivity reduces more slowly due to the effects of the subsurface moisture.

In the polarization ratio plots of Fig. 6.6 maximums occur when surface melt is expected to be present. As discussed in Section 6.2 and observed in Fig. 6.4, h-pol T_b are consistently less than v-pol. During melt the two emissivities become closer to equal corresponding to an increase in the polarization ratio. The 19H/19V ratio is largest during the period JD 190 to 195 and peaks at mid-afternoon when surface melting is expected. Minimums occur between late night and early morning during this period when the surface is expected to be freezing due to below freezing air temperatures and radiative cooling. The ratio also decreases during the refreeze period from JD 196 to 200.

6.3.1 Comparison with *in situ* data

The signatures of different vertical melt profiles observed in the SSM/I channel ratios are compared with *in situ* measurements from Mätzler [50]. Mätzler records T_b values for various frequencies and terrains of which a selected number are similar to Greenland surface profiles. The 21 and 35 GHz frequencies used by Mätzler are the closest to those analyzed herein for SSM/I. The snow scenes observed by Mätzler similar to those expected in Greenland are described in Table 6.1.

Figure 6.7 shows the polarization and frequency ratios for each of the relevant snow conditions observed by Mätzler (see Table 6.1). The plot is designed so that progression to the right on the horizontal axis corresponds to the progression of an idealized melt event beginning with a layer of dry snow. The snow melts and then the surface begins to refreeze with the frozen crust thickening over time. Consistent with the SSM/I observations, the frequency ratios display a small drop associated with surface melt progressing toward a large increase affiliated with a thick frozen crust over wet snow. Also similar to SSM/I observations, the polarization ratio increases during a melt event, with a maximum observed during the period when the melt is expected to have maximum depth (a thin frozen crust is present indicating the transition from melt to freeze). The polarization ratio decreases as the frozen crust thickens.

6.4 Theory

In order to better understand the physical mechanisms driving the sensitivity of SSM/I channel ratios to the different melt stages, we employ simple electromagnetic models based on the bulk properties of the snow pack. We first consider the frequency ratio followed by the polarization ratio.

6.4.1 Frequency ratio

The variation in the frequency ratio during the melting and freezing stages of the melt cycle is illustrated using a simple multi-layer model. The brightness temperature at the surface is the sum of the contributions from the individual layers, i.e.

$$T_b = \sum_{i=1}^{N} T_{bi} \tag{6.1}$$

where T_{b1} is the contribution from the top layer, T_{b2} is the contribution from the second layer, and T_{bN} is the contribution from the bottom layer. Assuming each layer is homogeneous in the physical properties of the snow and has a uniform temperature profile, the contribution from layer i in terms of the brightness temperature of an
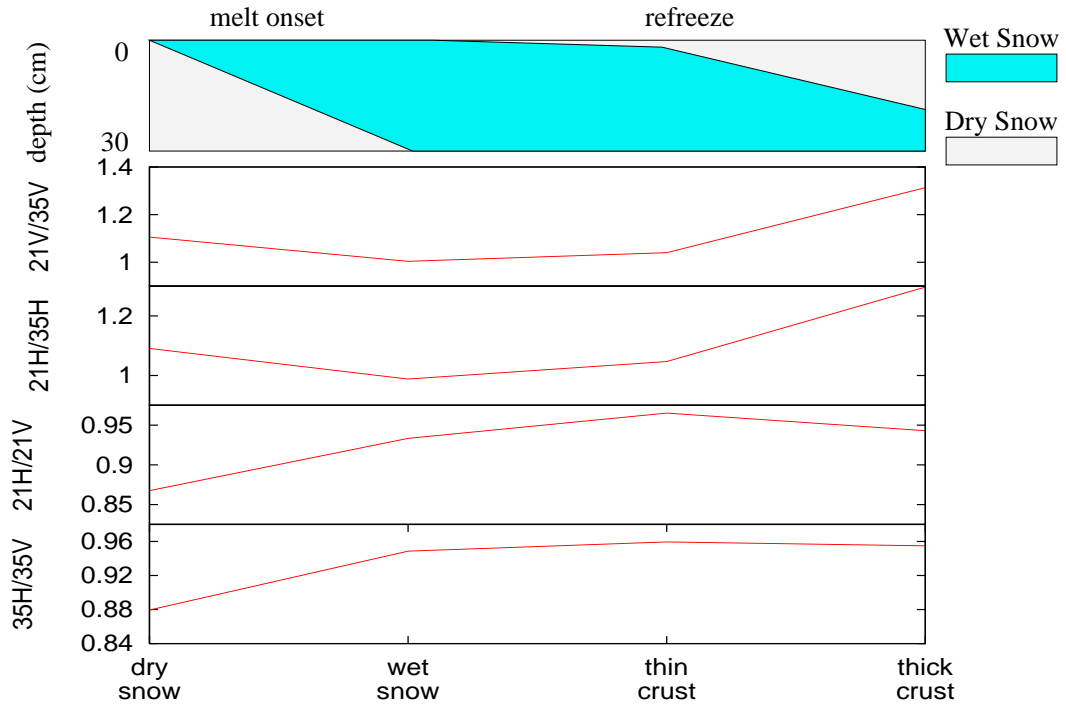
Figure 6.7: Channel ratios for certain snow conditions as given by Mätzler [50]. The horizontal axis represents the different snow profiles associated with an idealized melt event. It is in the order of the typical progression of a melt event from dry snow to wet snow to a thin then a thick frozen crust over an underlying layer of wet snow. A simplified illustration of the melt progression is shown above the plots. See Table 6.1 for definitions of snow types.

infinite half space with the same properties (T_{bi}^∞) is

$$T_{bi} = e^{-\tau_i} T_{bi}^\infty (1 - e^{-\kappa_{ei} d_i \sec \theta_i}) \prod_{j=1}^{i} \Upsilon_j \qquad (6.2)$$

where d_i is the depth of the ith layer, θ_i is the propagation angle in the layer, Υ_j is the power transmission at the upper boundary of the jth layer, and $\tau_i = \sum_{j=1}^{i} \kappa_{ej} d_j \sec \theta_j$ is the optical depth of the snow above the ith layer.

This model is used to simulate the relationship between $T_b(19V)$ and $T_b(37V)$ during a melt/freeze cycle. During melt, the vertical profile of the snow is modeled as two layers, wet snow over dry firn, with the depth of the wet snow increasing over time. Dry firn is used rather than new dry snow to simplify the model. Potential discrepancies between the model results and observed data trends due to this simplification are discussed later. During freeze, the surface is modeled as three layers: wet snow between two layers of dry firn. The bottom of the wet snow layer is assumed to freeze at one half the rate of the top of the wet snow layer (see Fig. 6.5).

The implementation of this multi-layer T_b model requires the estimates of T_b^∞, κ_e, and θ for each layer as well as Υ at each layer boundary. T_b^∞ is estimated based on observations in the southwest percolation zone during the year 2000. For convenience, I denote T_b^∞ for the dry firn as T_b^{dry} and T_b^∞ of the wet snow as T_b^{wet}.

The extinction coefficient (κ_e) of dry snow is estimated using the empirical formula from Hallikainen et al. [51] assuming the snow grain radius to be 0.5 mm. The extinction coefficient of wet snow is estimated using the relationship $\kappa_e = \kappa_s + \kappa_a$ where κ_s is the scattering coefficient and κ_a is the absorption coefficient. The absorption coefficient is a function of the complex relative dielectric constant (ϵ_r), i.e.

$$\kappa_a = 2\frac{2\pi f}{c} \Im\left\{\sqrt{\epsilon_r}\right\}$$

where f is the frequency, c is the speed of light in a vacuum and $\Im\{\cdot\}$ denotes the imaginary part. The complex relative dielectric constant is estimated using a *modified Debye-like model* from Ulaby et al. [38, pg. 2072] where the snow is assumed to have a density $\rho = 0.4$ g/cm^3. The scattering coefficient for wet snow is assumed to be similar to that of dry snow, which is negligible compared to κ_a of wet snow.

Table 6.2: Snow dielectric properties used for the simple multi-layer emission model. The associated frequency (f) is in GHz. All estimates are for vertical polarization.

	f	ϵ_r	κ_e	κ_a	κ_s	Υ_{air}	T_b^∞
dry firn	19	1.41	1.58	0.00	1.58	1.00	180
dry firn	37	1.38	10.20	0.00	10.20	1.00	160
wet snow	19	$1.44 + i0.029$	11.32	9.74	1.58	1.00	273
wet snow	37	$1.41 + i0.023$	25.18	14.98	10.20	1.00	273

The propagation angle (θ) is calculated using Snell's law with the estimates of ϵ_r. The power transmission (Υ) at the boundaries is calculated from the estimates of ϵ_r using Fresnel reflection. The estimated properties of the dry firn and wet snow are listed in Table 6.2.

Variations of in $T_b(19V)$ and $T_b(37V)$ during a melt cycle based on this multi-layer T_b model are illustrated in Fig. 6.8. During the melt phase T_b values follow a convex path originating at $(T_b^{\mathrm{dry}}(19V), T_b^{\mathrm{dry}}(37V))$ and ending at $(T_b^{\mathrm{wet}}(19V), T_b^{\mathrm{wet}}(37V))$. For shallow melt events, the T_b values follow the same path without reaching the end point. Four different paths are shown for the freeze phase based on different melt depths. Contrary to the melt phase, the path followed by the T_b values during the freeze phase of the melt cycle is significantly affected by the depth of the melt. In all cases, T_b during the freeze phase follows a concave path ending at $(T_b^{\mathrm{dry}}(19V), T_b^{\mathrm{dry}}(37V))$. The start point lies on the path followed during the melt phase with the location dependent on melt depth. The curvature of the path during the freeze phase increases with the depth of the melt. The results in Fig. 6.8 confirm the frequency ratio $(\gamma = T_b(19V)/T_b(37V))$ as a tool for discriminating between the melt and freeze portions of the melt cycle. Additionally, the maximum value of γ during freeze is an indicator of the melt depth.

Figure 6.9 shows SSM/I T_b measurements during 2000. These T_b estimates are at 6 hour intervals and originate from the SSM/I instrument aboard the F-14 satellite. The points are connected to illustrate the temporal evolution of the
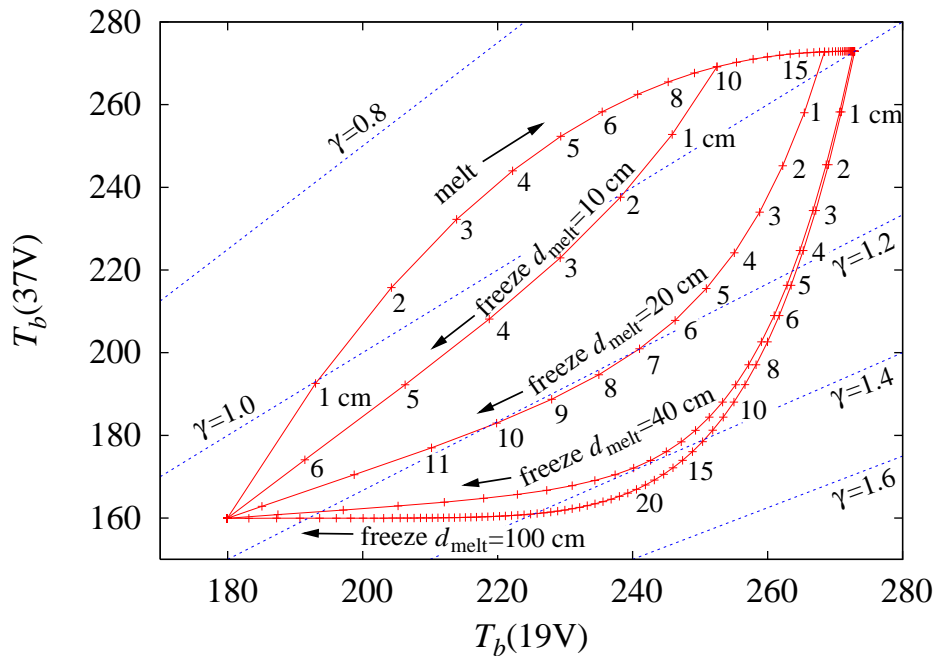
Figure 6.8: Simulated melt cycle for $T_b(19V)$ and $T_b(37V)$ with different melt depths represented. Numbers within the plot indicate incremental melt depths and depths of surface freeze. Lines of constant frequency ratio $(\gamma = T_b(19V)/T_b(37V))$ are also shown.

Figure 6.9: Scatterplot of $T_b(19V)$ versus $T_b(37V)$ during the year 2000 at 65.6 N, 47.6 W. The points are connected to indicate the temporal evolution. The cluster of points near the left side of the plot shows the effects of winter accumulation. Lines of constant frequency ratio (γ) are also shown in the plot.

measurements. The patterns in the Fig. 6.9 are similar to the simulations shown in Fig. 6.8. During many of the observed melt cycles, it appears that the surface does not achieve a frozen state before the melting repeats. The melt cycles in the plot show a distinct difference in the melt and refreeze paths, just as predicted by the model. The lines of constant frequency ratio (γ) indicate the applicability of this parameter in differentiating between melt and freeze.

The trend in T_b associated with winter accumulation is also indicated in Fig. 6.9. This migration during the winter is a result of the combination of changes in the surface due to accumulation and temperature variations. The idea of temperature variation alone causing this migration is ruled out based on the premise that temperature changes is expected to result in a straight line migration. Accumulation causes the surface emission to approach the behavior of dry snow which has higher T_b

values than the snow in the percolation and wet snow zones. Because of the smaller emission depth, the 37 GHz T_b increases at a faster rate than the 19 GHz T_b.

As mentioned previously, the model ignores the dry snow accumulation on the surface, assuming the snow profile to be comprised of firn prior to the melt event. This effectively ignores the T_b migration observed in Fig. 6.9 associated with accumulation. This simplification is expected only to effect the start point of the initial melt. After the first melt/freeze cycle, the surface snow is effectively firn.

6.4.2 Polarization ratio

The sensitivity of the polarization ratio to the melt or the freeze stage may be explained based on Fresnel reflection. Assuming that snow layers are isotropic, there is no difference between h-pol and v-pol in propagating through the volume of each snow layer. The polarization is only significant at the layer boundaries. Based on Fresnel reflection, the transmission of v-pol emissions through the boundary is always greater than the transmission of h-pol emissions through the boundary. During melt, the emission depth is small and the observed T_b is primarily from the top snow layer. For a single layer, the ratio of h-pol T_b to v-pol is primarily a function of the reflection at the air/snow interface. During freeze and for dry snow, the emission depth is much greater and many snow layers contribute to the observed T_b. For frozen snow, the ratio of h-pol to v-pol is less due to additional attenuation of h-pol emissions at subsurface layer interfaces. This effect is illustrated in the SSM/I T_b scatterplot in Fig. 6.10. In this case the largest ratio difference is between the end points as opposed to the frequency ratio where the largest difference is in the transition region. The hysteresis effect is smaller than for the frequency ratio, but may still be exploited to infer the melt depth.

6.5 Conclusions

The T_b polarization ratio and frequency ratio can be used separately or combined to differentiate between the melt and the freeze stages of the melt cycle. The 19 to 37 GHz frequency ratio increases when the surface is frozen and liquid water
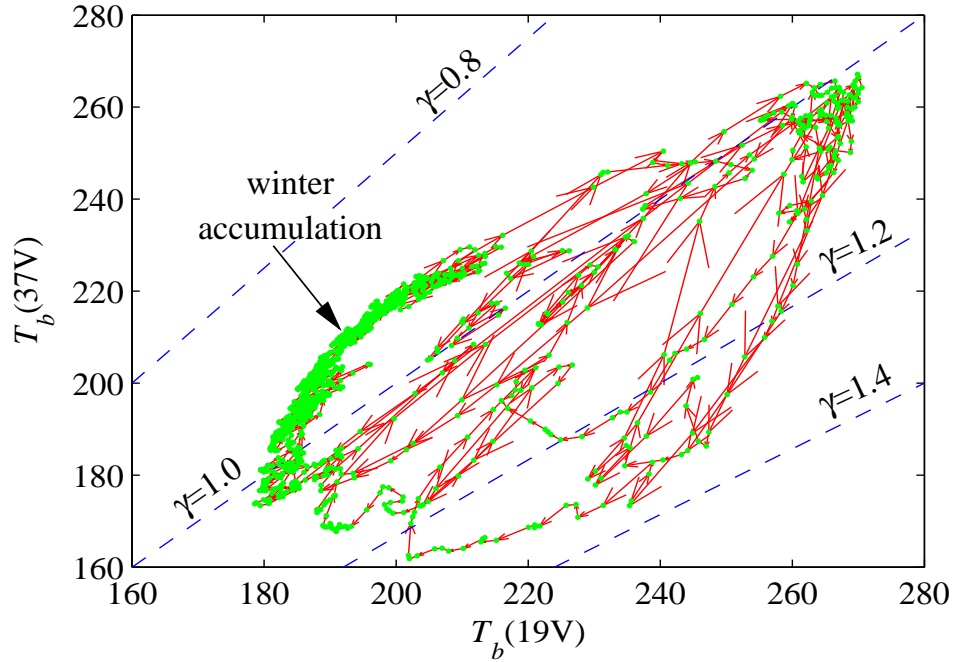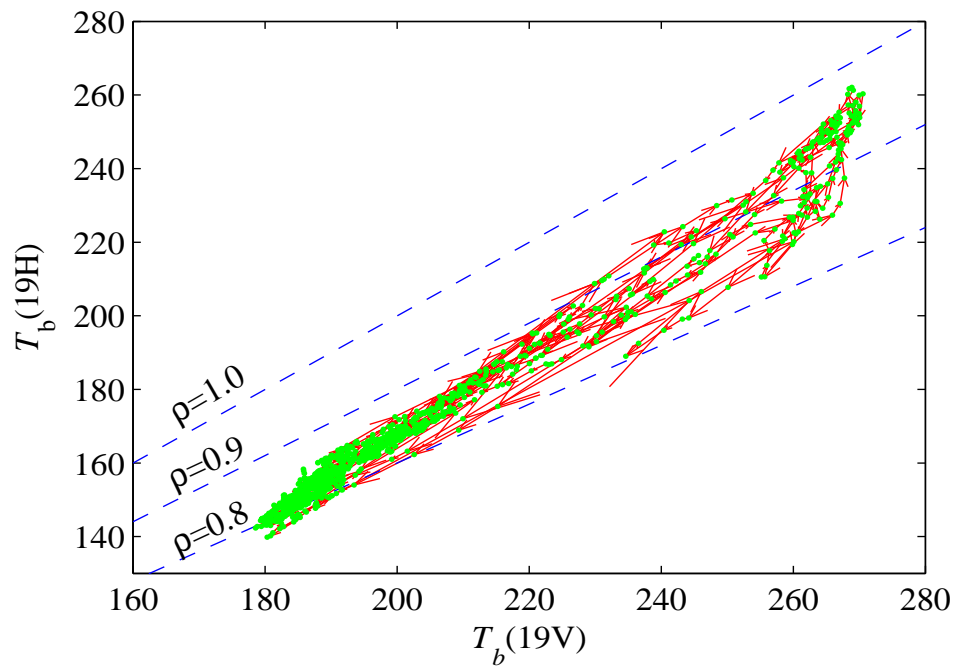
Figure 6.10: Scatterplot of $T_b(19V)$ versus $T_b(19H)$ during the year 2000 at 65.6 N, 47.6 W. The points are connected to indicate the temporal evolution. Lines of constant polarization ratio ($\rho = T_b(19H)/T_b(19V)$) are also shown in the plot.

is present in the subsurface. The horizontal to vertical polarization ratio increases when liquid water is present in the surface snow. The use of this technique in future studies will enable increased accuracy in ablation estimation and estimation of the overall mass-balance of the Greenland ice-sheet.

Chapter 7

Summary and Conclusions

This chapter summarizes the results found in this dissertation by first discussing the key observations for each study and then summarizing additional significant contributions including new models and methodologies. It ends with suggestions for future research for the continuation and advancement of these studies.

7.1 Key Observations

My studies of the Greenland ice sheet have resulted in several key observations of the microwave properties of the ice sheet and the relation of these properties to physical processes. Key observations are from four areas of research: Azimuth modulation of $\sigma°$, microwave signature of snow, melt detection over snow, and melt classification.

7.1.1 Azimuth modulation of $\sigma°$

Various aspects of azimuth modulation of $\sigma°$ over Greenland are analyzed in this dissertation. This analysis is original with this work since previous studies of azimuth modulation over Greenland are almost non-existent. Information regarding the azimuth modulation properties over Greenland is valuable for inter-comparison of SAR images, for *in situ* studies of azimuth modulation, and for general study of Greenland using $\sigma°$.

To investigate $\sigma°$ azimuth modulation two models are employed: a physical model relating $\sigma°$ azimuth variation to meso-scale surface roughness is used in Chapter 3 and a simple empirical model useful in characterizing the magnitude and

variability of the azimuth modulation is used in Chapter 4. The mean RMS error for ERS for the physical model is 0.46 dB compared with 0.56 dB for similar models assuming azimuthally isotropic surface roughness. The accuracy of the empirical model increases from a mean RMS error of 0.591 dB to 0.375 dB for ERS when azimuth modulation is included.

Both models indicate that the azimuth modulation is largest in the lower region of the dry snow zone and the upper edge of the percolation zone. This is the region where the largest meso-scale slope estimates are obtained from the scattering model inversion. Over most of Greenland, the azimuth modulation is dominated by a second order harmonic, although there is also a non-negligible contribution from the first order harmonic. The magnitude of the azimuth modulation is found to be relatively independent of incidence angle in the 25° to 45° incidence angle range. The orientation and magnitude are stable over time. Over a select few areas near the percolation zone/dry snow zone boundary, abrupt changes in the azimuth modulation are observed, which is attributed to changes occurring during summer melt events. Azimuth modulation of $\sigma°$ is generally larger at C-band than at Ku-band.

The orientation of the azimuth modulation is such that the minimum $\sigma°$ is aligned with the flow direction of the katabatic winds. This relationship between katabatic wind flow and azimuth modulation orientation is similar to what has been observed over Antarctica. This similarity is interesting because the katabatic winds are weaker over Greenland and storm winds, which are non-katabatic, have a greater impact.

7.1.2   Microwave signature

Chapter 4 presents a model for characterizing the $\sigma°$ microwave signature over Greenland. This model includes incidence angle dependence, azimuth dependence, the spatial gradient, and the temporal rate of change. The inclusion of the spatial gradient in the microwave signature model, which is original with this work, significantly reduces the RMS modeling error from 0.737 dB to 0.375 dB for ERS and from 0.658 dB to 0.458 dB for NSCAT.

Various attributes of the microwave signature in the different snow zones are discussed in Chapter 4 with only a few repeated here. Estimation of the parameters of this model using ERS and NSCAT data indicates that the σ° signatures at the two frequencies exhibit similar trends throughout the different snow zones. A general difference with frequency is that the extremes are typically greater at C-band. The minimum backscatter, which occurs in the dry snow zone, is smaller at C-band and the maximum backscatter, which occurs in the percolation zone, is larger. The incidence angle dependence is greater and the azimuth variation is larger at C-band. Extrema in the model estimates indicating the dry snow zone/percolation zone boundary generally occur further down slope at Ku-band.

One application of this characterization model is the observation of inter-annual changes on the ice-sheet through monitoring changes in the model parameters. Over the 9-year span of ERS data significant changes only occur in specific areas primarily concentrated near the dry snow line. The observed changes are attributed to variations in the annual Greenland ice-sheet melt extent, the formation of iced-firn on the snow surface, the formation of subsurface ice structures, and variations in the annual accumulation rate. Using only the microwave signature model parameters, rough relative estimates of the annual melt and accumulation rates may be obtained.

In studies of short term change, using this model and assuming the σ° dependencies are constant over time reduces the signal variance and increases the possible temporal resolution compared with previous methods. Because these model parameters are relatively stable between summer melt events, they can be used to normalize individual measurements. This method can be used to reduce noise due to observation geometry sampling and co-location bias in the estimation of short term variations in the average backscatter. Improvements over previous methods include increased temporal resolution and reduced variance in the observed signal. When applied, this method enables higher sensitivity to short melt events and to small magnitude seasonal cycles such as those observed in the dry snow zone.

7.1.3 Melt detection

Chapter 5 presents a comparison between 6 different melt detection methods. This comparison finds significant discrepancies between existing methods which are primarily attributed to differences in the intrinsic definitions. In an effort to obtain consistent detection of melt from scatterometers and radiometers, a simple physical model of a melt process is used. This model is consistent with a uniform definition of melt across the ice sheet. Melt detection based on this model is termed α-based.

QSCAT α-based melt detection with QSCAT appears the most robust. QSCAT (Ku-band) is more sensitive to small-melt at onset and less sensitive to subsurface melt during refreeze than ERS (C-band) due to the higher frequency. QSCAT also has superior temporal coverage with more frequent sampling and sampling closer to mid-afternoon, the local time-of-day when peak melt is expected. Melt detection with QSCAT is more robust than with SSM/I because the estimation of the physical model parameters for σ° are more precise than for T_b because σ° is relatively independent of the physical temperature of the surface.

The results of α-based melt detection with SSM/I, QSCAT, and ERS are consistent with correlation coefficients ranging from 0.73 to 0.87. QSCAT and SSM/I α-based melt detection estimate that 58% and 62% of the ice sheet, respectively, melted in 2000 which is consistent with the 60% estimate obtained using the dry snow zone boundary given by Benson [30]. Due to reduced temporal sampling and reduced sensitivity due to frequency, ERS detects only 48% of the ice sheet as experiencing melt. ERS also detects periods of prolonged refreeze due to increased sensitivity to subsurface moisture at lower frequencies.

The non-α-based methods vary widely in their results. XPGR indicates that only 32% of the ice sheet experiences melt and has a correlation coefficient of 0.42 with QSCAT α-based melt detection. XPGR also appears to be strongly sensitive to melt during refreeze. T_b-M matches α-based detection except for bias toward detecting more melt in regions with low winter T_b values and small amounts of melt in regions with high winter T_b values. Q-DV melt detection estimates that

59% of the ice sheet experiences melt during 2000 and has a correlation coefficient of 0.57 with QSCAT α-based melt detection. Although the annual melt extent estimate is consistent with QSCAT and SSM/I α-based detection, the daily estimates of the Q-DV melt extent appears sporadic, changing dramatically from day to day during the summer melt period.

7.1.4 Melt classification

Chapter 6 discussed the classification of melt as either surface or subsurface. Due to lack of available *in situ* data on the vertical profile of the moisture content in the snow, high temporal resolution estimates of the T_b diurnal variation are used to associate data trends with the different stages of the daily melt cycle. Results indicate that the T_b polarization ratio (horizontal over vertical) is a sensitive indicator of surface melt and that the T_b frequency ratio (37 GHz over 19 GHz) is a sensitive indicator of subsurface melt. These trends are confirmed by *in situ* T_b and snow moisture profile measurements. These observations serve as a foundation for the classification of detected melt as either surface or subsurface.

7.2 Contributions

This dissertation contains several specific contributions in new models and methods that have made the above observations possible. These contributions are necessary steps for refining microwave remote sensing over Greenland.

7.2.1 Scattering model for azimuth modulation

A new simple scattering model for snow is presented in Chapter 3, which provides a solid link between azimuth modulation and the surface slope distribution. Previous to this work, azimuth modulation had been attributed to sastrugi formed by katabatic winds, but no models were presented to confirm this. Existing $\sigma°$ azimuth modulation models are developed for ocean scattering and are derived from Bragg scattering which occurs on scales significantly smaller than sastrugi.

7.2.2 Spatial and temporal dependence model

The observation model presented in Chapter 4 for characterization of the microwave signature contains two new terms for modeling $\sigma°$. The spatial dependence term is entirely new and reduces the mean RMS modeling by mitigating the effects of co-location bias. The modeling error reduction is 50% for ERS and 30% for NSCAT. Modeling of the spatial dependence is especially important in high temporal resolution studies where the spatial sampling of $\sigma°$ is sparse. The idea for modeling the temporal dependence of $\sigma°$ was first presented by Wismann et al. [20] and is adapted here to be included into the microwave signature characterization model. Although the reduction in the mean RMS error is much smaller for the inclusion of temporal dependence in the model than spatial dependence, the temporal dependence parameter provides important information related to annual accumulation. The use of this observation model for azimuth modulation is also new over Greenland, being used previously by Long and Drinkwater [24] to characterize azimuth modulation only in Antarctica.

7.2.3 Improved methods for tracking temporal change

Based on the observation model in Chapter 4, a new methodology is introduced for tracking short term changes over the ice-sheet. Because the parameters modeling the observation geometry dependence of $\sigma°$ are relatively stable over time, they may be assumed to be constant during the interval of short term (less than a year) temporal change studies. By not re-estimating these parameters at every time increment, the variance of the signal indicating temporal change is greatly reduced. A more complex model may be used providing increased accuracy and the possible temporal resolution is increased. This method is applied for $\sigma°$ melt detection in Chapter 5. The full observation model also enables enhanced tracking of long term change through monitoring the various aspects of the microwave signature.

7.2.4 Physical melt detection model

In Chapter 5 a simple physical model for use in melt detection with T_b and σ° is presented. Previous melt detection methods such as XPGR [2, 4, 5] and the method used by Mote et al. [11] (T_b-M) have theoretical support, but lack an explicit model. An alternate method presented by Mote and Anderson [12] is based on an explicit physical model; however, it is complex and difficult to reproduce. The model presented herein reduces to a simple data based algorithm so that future investigators are not required to implement the details of the model. This model is applicable to σ° melt detection as well as T_b.

7.2.5 New method for melt detection using T_b

The simple physical melt model from Chapter 5 is used to define a new method for melt detection using T_b. This method eliminates unnatural phenomenon observed in other T_b melt detection methods such as intermittent gaps in the detected melt during large melt events and melt detected at high elevations while not being detected at low elevations. This new method for T_b melt detection is also consistent with results from σ° based melt detection which was not the case for previous methods.

This simple physical model results in a melt detection algorithm for σ° similar to that used by Wismann [14] for ERS. Small differences exist in the melt threshold and other implementation details. The use of this melt detection method with QSCAT is original with this work.

7.2.6 Melt classification framework

In Chapter 6, a framework is introduced for classification of melt as either surface or subsurface using SSM/I T_b measurements. This method is based on the polarization and frequency differences which can be explained based on the fundamental electro-magnetic properties of snow. This is a simple methodology that is reasonably well understood to address the issue of quantifying the amount of ablation during periods of detected melt. Although the use of data fusion of SSM/I channels for melt

detection is not a new idea, the specific simple methods presented in this dissertation have not previously been introduced for the purpose of melt classification.

7.3 Publications

Multiple papers are derived from work in this dissertation. The material in Chapter 3 is currently in review for publication in the *Journal of Glaciology* and the material in Chapter 4 is currently in review for publication in the *IEEE Transactions on Geoscience and Remote Sensing*. Material contained in Chapter 5 is in final preparation for submission to the *International Journal of Remote Sensing* and Chapter 6 contains material in preparation for submission to *IEEE Transactions on Geoscience and Remote Sensing Letters*. Additionally, work related to this dissertation has been published in 9 conference papers [32, 45, 52, 53, 54, 55, 56, 57, 58].

7.4 Future Work

The ideas, methods, and results in this dissertation stand as a framework upon which to build future studies using microwave remote sensing to track changes over Greenland. Suggestions for future studies are divided into two areas: further refinements in the methods presented, and the use of this work in new studies. Areas for further refinement of methods in this dissertation include

- the use of a different small-scale model such as small-slope approximation in the azimuth modulation model,

- validation of the azimuth modulation model using *in situ* measurements,

- improved methods for estimation of the physical model parameters in melt detection, and

- the development of a melt classification algorithm applicable to large-scale studies of the ice sheet.

Suggestions for new studies based on methods from this dissertation include

- the use of the model for characterization of the σ° microwave signature and the physical model-based melt detection methods for the creation of a new updated facies map of Greenland,

- the development of an automated algorithm for facies classification,

- the use of the full σ° signature model in future studies of long and short term changes over Greenland,

- the implementation of an adaptive model for the microwave filter based on the use of a Kalman filter with the full σ° signature model,

- use of the α-based melt detection methods for the investigation of long-term trends in changing melt extent and duration using SSMR, SSM/I, and QSCAT, and

- application of a melt classification algorithm for determining the percent of detected melt representing surface melt and the percent representing subsurface melt.

As microwave remote sensing of Greenland becomes more refined, it can be used to increase the accuracy of Greenland mass-balance studies resulting in more accurate estimation of the effects of a changing climate on our environment.

Appendix

Appendix A

Co-location Bias

In Chapter 3 the scattering model parameters are estimated using ERS measurements from within a 30 km radius of the study site. Because the surface is non-uniform, these measurements may exhibit spatially correlated variations or bias according to the measurement location. The bias is particularly large in the transition region from the dry snow zone to the percolation zone. This *co-location bias* adversely effects the scattering model estimation and analysis in at least two ways. First, when estimating the scattering model parameters, the co-location bias may be misinterpreted as azimuth or incidence angle dependence based in part on the incidence angle, azimuth angle, and location sampling. Second, the co-location bias may be misinterpreted as an inadequacy of the model in matching the measured incidence angle and azimuth angle dependence of the σ° measurements. Although the co-location bias cannot be completely eliminated from the data, it may be estimated in order to negate the adverse effects on the scattering model estimates and analysis.

The co-location bias is observed in the modeling error. Figure A.1 (a) shows how the modeling error varies with the displacement of the measurement centroid from the center of the study site. To characterize the dependence of the modeling error on location offset I use a simple model

$$\nu = s_0 + s_1(\vec{r} \cdot \hat{g})$$

where ν is the modeling error, $\vec{r}$ is the vector from the study site to the measurement center, and s_0, s_1, and $\hat{g}$ are model parameters which are obtained using least-squares estimation. Fig. A.1 (b) shows the estimation errors versus $\vec{r} \cdot \hat{g}$ along with the linear

fit. The plot indicates that at this location, the co-location bias contributes up to ± 2 dB to the residual error.

In order to diminish the effects of the co-location bias on the physical surface model estimates, this bias is estimated and removed prior to estimating the surface roughness using a simple linear model which is fit to the σ° measurements. The model is

$$\sigma^\circ(\theta, \phi) = A + B\theta + C_1 \cos(\phi) + S_1 \sin(\phi)C_2 \cos(2\phi) + S_2 \sin(2\phi) + s_1(\vec{r} \cdot \hat{g}) \quad \text{(A.1)}$$

where A, B, C_1, C_2, S_1, and S_2 are the model parameters. After estimating the parameters using linear least-squares regression, the co-location bias is removed from the σ° measurements by subtracting $s_1(\vec{r} \cdot g)$. Azimuth dependence is included in Eq. (A.1) to minimize the possibility of biasing the co-location bias correction based on azimuth sampling. At the NASA-U location, co-location parameter estimates are $s_1 = 0.092$ and $\angle \hat{g} = 263^\circ$. Without correcting for the co-location bias, the RMS modeling error is 1.29 dB. Correcting for the co-location bias leads to a RMS modeling error of only 0.40 dB, a significant improvement.
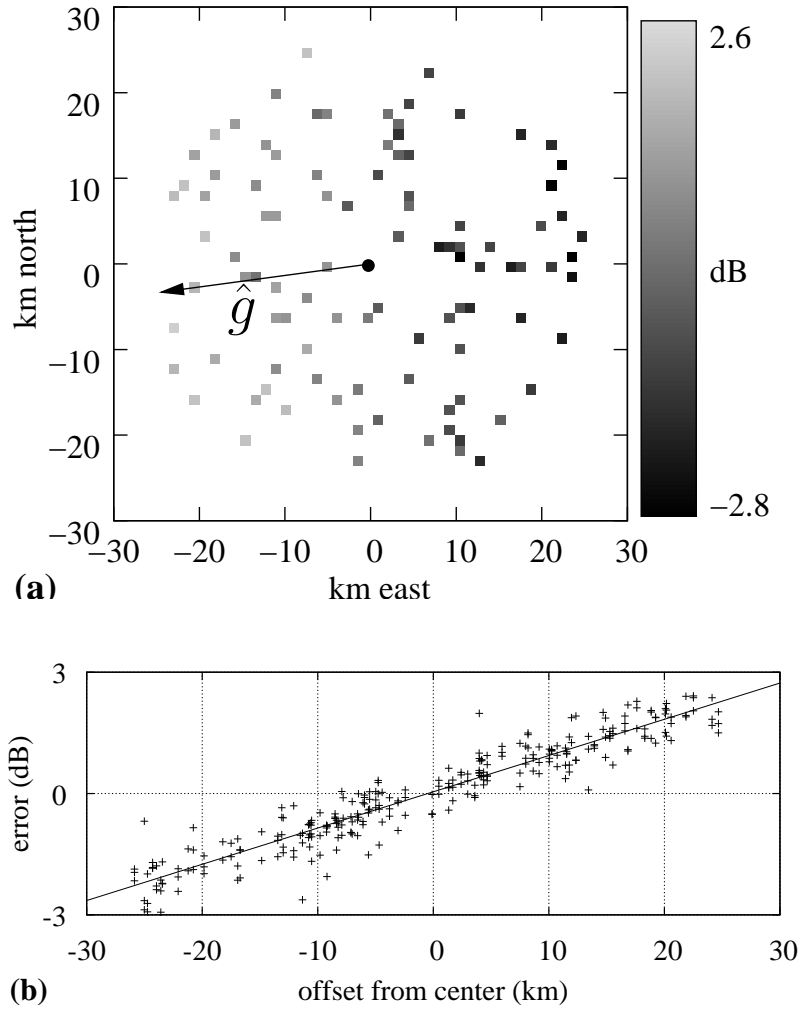
Figure A.1: Co-location bias of A-model estimates at the NASA-U site. (a) Residual error versus displacement between the measurement centroid and the center of the study site. The error magnitude is indicated by the gray-scale. The $\hat{g}$ vector indicates the direction of the backscatter gradient. (b) Magnitude of the error versus $\vec{r}_i \cdot \hat{g}$ or the distance in the $\hat{g}$ direction of the measurement centroid from the center of the study area. The line shows the co-location bias model fit to the estimation errors.

Appendix B

Slope Covariance Matrix Decomposition

The A-model in Chapter 4 assumes a Gaussian distribution of surface slopes for which the probability distribution function is

$$P(\vec{s}) = \frac{1}{2\pi |R|^{1/2}} e^{-(1/2)\vec{s}^T R^{-1} \vec{s}}$$

where the covariance matrix is

$$R = E\left\{\vec{s}\vec{s}^T\right\} = \begin{bmatrix} r_x & r_{xy} \\ r_{yx} & r_y \end{bmatrix}.$$

$E\{\cdot\}$ is the expected value operator. The surface slope covariance R has a physical interpretation in terms of a preferential direction in the surface roughness which can be found using the singular value decomposition $R = U^T R U$. The diagonal elements of Σ are the singular values of R, ξ_1^2 and ξ_1^2, and represent the maximum and minimum variance of the surface slope over the range of ϕ (azimuth angle). The singular values of R are given by

$$\xi^2 = \frac{1}{2}\left(r_x + r_y \pm \sqrt{(r_x - r_y)^2 + 4r_{xy}^2}\right).$$

The directions of the maximum and minimum surface slope variance are obtained by interpreting U as a rotational matrix

$$U = \begin{bmatrix} \cos\phi & \sin\phi \\ -\sin\phi & \cos\phi \end{bmatrix}.$$

Setting the off-diagonal terms of $U^T R U$ to zero results in the rotation angle

$$\phi = \frac{1}{2}\arctan\frac{2r_{xy}}{r_x - r_y} \tag{B.1}$$

which has two solutions corresponding to the directions of maximum and minimum surface slope variance.

Bibliography

[1] W. S. B. Paterson and N. Reeh, "Thinning of the ice sheet in northeast Greenland over the past forty years," *Nature*, vol. 414, pp. 60–61, November 2001.

[2] W. Abdalati and K. Steffen, "Snowmelt on the Greenland ice sheet as derived from passive microwave satellite data," *Journal of Climate*, vol. 10, pp. 165–175, February 1997.

[3] W. Krabill, W. Abdalati, E. Frederick, S. Manizade, C. Martin, J. Sonntag, R. Swift, R. Thomas, W. Wright, and J. Yungel, "Greenland ice sheet: High-elevation balance and peripheral thinning," *Science*, vol. 289, no. 5478, pp. 428–430, Jul 2000.

[4] W. Abdalati and K. Steffen, "Greenland ice sheet melt extent: 1979-1999," *Journal of Geophysical Research*, vol. 106, no. D24, pp. 33983–33988, December 2001.

[5] W. Abdalati and K. Steffen, "Passive microwave-derived snow melt regions on the Greenland ice sheet," *Geophysical Research Letters*, vol. 22, no. 7, pp. 787–790, April 1995.

[6] D. G. Long and M. R. Drinkwater, "Greenland ice-sheet surface properties observed by the Seasat-A scatterometer at enhanced resolution," *Journal of Glaciology*, vol. 40, no. 135, pp. 213–230, 1994.

[7] M. Fahnestock, R. Bindschadler, R. Kwok, and K. Jezek, "Greenland ice sheet surface properties and ice dynamics from ERS-1 SAR imagery," *Science*, vol. 262, pp. 1530–1534, December 1993.

[8] K. C. Partington, "Discrimination of glacier facies using multi-temporal SAR data," *Journal of Glaciology*, vol. 44, no. 146, pp. 42–53, 1998.

[9] K. C. Jezek, M. R. Drinkwater, J. P. Crawford, R. Bindschadler, and R. Kwok, "Analysis of synthetic aperture radar data collected over the southwestern Greenland ice sheet," *Journal of Glaciology*, vol. 39, no. 131, 1993.

[10] M. R. Drinkwater and D. G. Long, "Seasat, ERS-1/2 and NSCAT scatterometer observed changes on the large ice sheets," in "ESA SP-424," pp. 91–96, Noordwijk, The Netherlands: ESA Publications Div., ESTEC, November 1998.

[11] T. L. Mote, M. R. Anderson, K. C. Kuininen, and C. M. Rowe, "Passive microwave-derived spatial and temporal variations of summer melt on the Greenland ice sheet," *Annals of Glaciology*, vol. 17, pp. 233–238, 1993.

[12] T. L. Mote and M. R. Anderson, "Variations in snowpack melt on the Greenland ice sheet based on passive-microwave measurements," *Journal of Glaciology*, vol. 41, no. 137, pp. 51–60, 1995.

[13] W. Abdalati and K. Steffen, "The apparent effects of the Mt. Pinatubo eruption on the Greenland ice sheet melt extent," *Geophysical Research Letters*, vol. 24, no. 14, pp. 1795–1797, July 1997.

[14] V. Wismann, "Monitoring of seasonal snowmelt on Greenland with ERS scatterometer data," *IEEE Transactions on Geoscience and Remote Sensing*, vol. 38, no. 4, pp. 1821–1826, 2000.

[15] V. S. Nghiem, K. Steffen, R. Kwak, and W.-Y. Tsai, "Detection of snowmelt regions on the Greenland ice sheet using diurnal backscatter change," *Journal of Glaciology*, vol. 47, no. 159, pp. 539–547, 2001.

[16] J. D. Pack and M. A. Jensen, "Greenland snowmelt estimation using multi-spectral passive and active microwave observations," in "Proceedings of the IEEE International Geoscience and Remote Sensing Symposium," pp. 2106–2108, 2002.

[17] J. F. Bolzan and K. C. Jezek, "Accumulation rate changes in central Greenland from passive microwave data," *Polar Geography*, vol. 24, no. 2, pp. 98–112, 2000.

[18] M. R. Drinkwater, D. G. Long, and A. W. Bingham, "Greenland snow accumulation estimates from satellite radar scatterometer data," *Journal of Geophysical Research*, vol. 106, no. D24, pp. 33935–33950, December 2001.

[19] R. R. Forster, K. C. Jezek, J. Bolzan, F. Baumgartner, and S. P. Gogineni, "Relationships between radar backscatter and accumulation rates on the Greenland ice sheet," *International Journal of Remote Sensing*, vol. 20, no. 15, pp. 3131–3147, Oct. 1999.

[20] V. Wismann, D. P. Winebrenner, K. Boehnke, and R. J. Arhern, "Snow accumulation on Greenland estimated from ERS scatterometer data," in "Proceedings of the IEEE International Geoscience and Remote Sensing Symposium," pp. 1823–1825, 1997.

[21] J. D. Pack and M. A. Jensen, "Estimating snow accumulation on Greenland from SSM/I radiometer data," in "Proceedings of the IEEE International Geoscience and Remote Sensing Symposium," pp. 946–948, 2001.

[22] M. Ledroit, F. Remy, and J. F. Minster, "Observations of the Antarctica ice sheet with the Seasat scatterometer: relation to katabatic-wind intensity and direction," *Journal of Glaciology*, vol. 39, no. 132, pp. 385–396, 1993.

[23] N. Young, D. Hall, and G. Hyland, "Directional anisotropy of C-band backscatter and orientation of surface microrelief in East Antarctica," in "Proceedings of the First Australian ERS Symposium," pp. 117–126, Feb. 1996.

[24] D. G. Long and M. R. Drinkwater, "Azimuth variation in microwave scatterometer and radiometer data over Antarctica," *IEEE Transactions on Geoscience and Remote Sensing*, vol. 38, no. 4, pp. 1857–1870, 2000.

[25] F. Ulaby, R. Moore, and A. Fung, *Microwave Remote Sensing: Active and Passive*, vol. 2, Norwood, Massachusetts: Artech House, Inc., 1986.

[26] F. Ulaby, R. Moore, and A. Fung, *Microwave Remote Sensing: Active and Passive*, vol. 1, Norwood, Massachusetts: Artech House, Inc., 1981.

[27] J. P. Hollinger, J. L. Peirce, and G. A. Poe, "Ssm/i instrument evaluation," *IEEE Transactions on Geoscience and Remote Sensing*, vol. 28, no. 5, pp. 781–790, September 1990.

[28] D. S. Early and D. G. Long, "Image reconstruction and enhanced resolution imaging from irregular samples," *IEEE Trans. on Geosci. and Rem. Sens.*, vol. 39, no. 2, pp. 291–302, 2001.

[29] B. Fristrup, *The Greenland Ice Cap*, Seattle, Washington: University of Washington Press, 1966.

[30] C. S. Benson, "Stratigraphic studies in the snow and firn of the Greenland ice sheet," *SIPRE Res. Rep.*, 1962.

[31] C. T. Swift, P. S. Hayes, J. S. Herd, W. L. Jones, and V. E. Delnore, "Airborne microwave measurements of the Southern Greenland ice sheet," *Journal of Geophysical Research*, vol. 90, no. B2, pp. 1983–1994, February 1985.

[32] I. S. Ashcraft and D. G. Long, "Azimuth variation in microwave backscatter over the Greenland ice sheet," in "Proceedings of the IEEE International Geoscience and Remote Sensing Symposium," vol. 4, pp. 1779–1781, 2001.

[33] D. H. Bromwich, Y. Du, and K. M. Hines, "Wintertime surface winds over the Greenland ice sheet," *Monthly Weather Review*, vol. 124, pp. 1941–1947, September 1996.

[34] D. H. Bromwich, T. R. Parish, and C. A. Zorman, "The confluence zone of the intense katabatic winds at Terra Nova Bay, Antarctica, as derived from airborne sastrugi surveys and mesoscale numerical modeling," *Journal of Geophysical Research*, vol. 95, no. D5, pp. 5495–5509, April 1990.

[35] C. T. Swift, "Seasat scatterometer observations of sea ice," *IEEE Transactions on Geoscience and Remote Sensing*, vol. 37, no. 2, pp. 716–723, March 1999.

[36] S. L. Broschat and E. I. Thorsos, "An investigation of the small slope approximation for scattering from rough surfaces, Part ii. Numerical studies," *J. Acoust. Soc. Am.*, vol. 101, no. 5, pp. 2615–2625, 1997.

[37] D. W. Marquardt, "An algorithm for least squares estimation of nonlinear parameters," *Journal of the Society for Industrial and Applied Mathematics*, vol. 11, pp. 431–441, 1963.

[38] F. Ulaby, R. Moore, and A. Fung, *Microwave Remote Sensing: Active and Passive*, vol. 3, Norwood, Massachusetts: Artech House, Inc., 1990.

[39] K. Steffen, J. E. Box, and W. Abdalati, "Greenland Climate Network: GC-Net," *CRREL Special Report on Glaciers, Ice sheets and Volcanoes*, vol. 96-27, pp. 98–103, 1996.

[40] E. P. W. Attema and P. Lecomte, "The ERS-1 and ERS-2 wind scatterometers, system performance and data products," in "Proceedings of the IEEE International Geoscience and Remote Sensing Symposium," pp. 1967–1969, 1998.

[41] A. Ohmura and N. Reeh, "New precipitation and accumulation maps for Greenland," *Journal of Glaciology*, vol. 37, no. 125, pp. 140–148, 1991.

[42] R. C. Bales, J. R. McConnel, E. Mosley-Thompson, and B. Csatho, "Accumulation over the Greenland ice sheet from historical and recent records," *Journal of Geophysical Research*, vol. 106, no. D24, pp. 33813–33825, December 2001.

[43] K. C. Jezek, P. Gogineni, and M. Shanableh, "Radar measurements of melt zones on the Greenland ice sheet," *Geophysical Research Letters*, vol. 21, no. 1, pp. 33–36, January 1994.

[44] I. S. Ashcraft and D. G. Long, "Relating microwave backscatter azimuth modulation to surface properties of the Greenland ice sheet," Submitted to *Journal of Glaciology*, 2004.

[45] I. S. Ashcraft and D. G. Long, "SeaWinds views Greenland," in "Proceedings of the IEEE International Geoscience and Remote Sensing Symposium," vol. 3, pp. 1131–1136, 2000.

[46] J. D. Pack, J. W. Wallace, and M. A. Jensen, "Greenland snow ablation and accumulation observed using ERS and SSM/I data," in "Proceedings of the IEEE International Geoscience and Remote Sensing Symposium," pp. 1128–1130, 2000.

[47] J. R. McConnell, G. Lamorey, E. Hanna, E. Mosley-Thompson, R. C. Bales, D. Belle-Oudry, and J. D. Kyne, "Annual net snow accumulation over southern Greenland from 1975 to 1998," *Journal of Geophysical Research*, vol. 106, no. D24, pp. 33827–33837, December 2001.

[48] A. W. Bingham and M. R. Drinkwater, "Recent changes in the microwave scattering properties of the Antarctic ice sheet," *IEEE Trans. on Geosci. and Rem. Sens.*, vol. 38, no. 4, pp. 1810–1820, 2000.

[49] I. S. Ashcraft and D. G. Long, "SeaWinds views Greenland," in "Proceedings of the IEEE International Geoscience and Remote Sensing Symposium," vol. 3, pp. 1131–1136, 2000.

[50] C. Mätzler, "Passive microwave signatures of landscapes in winter," *Meteorol. Atmos. Phys.*, vol. 54, pp. 241–260, 1994.

[51] M. T. Hallikainen, F. T. Ulaby, and T. E. V. Deventer, "Extinction behavior of dry snow in the 18- to 90-ghz range," *IEEE Transactions on Geoscience and Remote Sensing*, vol. GE-25, no. 6, pp. 737–745, November 1987.

[52] I. S. Ashcraft and D. G. Long, "Relating microwave backscatter azimuth modulation to surface properties of the Greenland ice sheet," in "Proceedings of the IEEE International Geoscience and Remote Sensing Symposium," vol. 3, pp. 1610–1612, 2003.

[53] I. S. Ashcraft and D. G. Long, "Increasing temporal resolution in Greenland ablation estimation using passive and active microwave data," in "Proceedings

of the IEEE International Geoscience and Remote Sensing Symposium," vol. 3, pp. 1604–1606, 2003.

[54] I. S. Ashcraft and D. G. Long, "The spatial response function of SeaWinds backscatter measurements," in W. L. Barnes, ed., "Earth Observing Systems VIII," vol. 5151 of *Proceedings of SPIE*, pp. 609–618, 2003.

[55] I. S. Ashcraft and D. G. Long, "Multi-annual changes in microwave backscatter over the Greenland ice sheet," in "Proceedings of the IEEE International Geoscience and Remote Sensing Symposium," vol. 2, pp. 958–960, 2001.

[56] I. S. Ashcraft and D. G. Long, "Microwave backscatter over greenland: Changing with time," in W. L. Barnes, ed., "Earth Observing Systems VI," vol. 4483 of *Proceedings of SPIE*, pp. 127–134, 2001.

[57] I. S. Ashcraft and D. G. Long, "Using SeaWinds resolution enhanced images for large scale monitoring of the earth's surface," in "World Multiconference on Systemics, Cybernetics, and Informatics," vol. 6, pp. 220–225, 2001.

[58] I. Ashcraft, D. Long, A. Anderson, S. Richards, M. Spencer, and B. Jones, "Sigma-0 retrieval from SeaWinds on QuikSCAT," in W. L. Barnes, ed., "Earth Observing Systems IV," vol. 3750 of *Proceedings of SPIE*, pp. 171–179, 1999.